The Construction and Commissioning of the Straw Tracking Detector in the New Muon g-2 Experiment at Fermilab

UNIVERSITY OF LIVERPOOL

William Turner

Department of Physics

University of Liverpool

This dissertation is submitted for the degree of

Doctor of Philosophy

October 2018

Declaration

I hereby declare that except where specific reference is made to the work of others, the contents of this thesis is my own.

William Turner

October 2018

Acknowledgements

I would like to acknowledge **Joe Price**, **Mark Lancaster**, **James Mott**, **Barry King**, **Saskia Charity**, **Rebecca Chislett** and **Nick Kinnaird** for their close support, guidance, criticism and above all for enforcing a key work life balance. As well as everyone who made working on g-2 enjoyable, **Midhat Farooq**, **Joe Grange**, **Gleb Lukicov**, **Tom Stuttard**, **Cristina Schlesier** and **Deepak Sathyan** as well as many more.

I also wish to thank everyone who worked on the straw tracker design, construction and testing at Liverpool in particular **Mike Wormald**, **David Sim**, **Talal Albahri**, **Tabitha Halewood-Leagas** and **Kayleigh Thomson** who made the many hours in the clean room fun and stimulating. As well as **Steve Maxfield**, **Themis Bowcock**, **Alex Keshavarzi** who introduced many aspects of g-2 in an understandable way and for their guidance through my studies. I would also like to note the kindness and support of **Chris Barry**, **Pratiksha Paudyal**, **Adam Roberts**, **Ahmed Omar**, **Thomas Otobong** as well as the rest of the residents of the 4th floor office for providing coffee and biscuits in times of need.

This work would not have been possible without the support of my family as well as from **Sarah White** who laughed each and every time I mentioned 'Perturbed Wiggles'.

I want to extend a special thanks to **Dr. Clive McLintock** for supporting the Department of Physics by establishing the Particle Physics Alumni Studentship Fund. Without his kindness the work presented herein would not have been possible. *The Particle Physics Alumni Studentship Fund, founded in 2014 by Dr Clive McLintock.*

Abstract

The anomalous magnetic moments of leptons have been a long standing test of the standard model of particle physics as they can be both measured experimentally and predicted theoretically with high precision. In particular the anomalous magnetic moment of the muon, a_μ, has been favoured due to its sensitivity to new physics effects. Currently the world's best measurement of a_μ was made at Brookhaven National Laboratory (BNL) in 2001 which resulted in a 3σ deviation between the experimental measurement and theoretical prediction. Since this measurement a number of improvements have been made to the theoretical prediction giving a deviation between theoretical prediction and measured value of over 3.5σ.

A new experimental effort has been set up at Fermi National Laboratory (FNAL) in order to measure a_μ with a factor of four reduction in the experimental uncertainties. If these aims are met and the central measurement value stays the same a discrepancy will be discovered providing strong evidence for new physics effects. The FNAL experiment uses the same experimental method as BNL which centres around measuring the precession of the μ^+ spin after circling an extremely precise magnetic storage ring.

To reduce the experimental uncertainties in the new experiment straw tracking detectors have been constructed and installed into the Fermilab muon g-2 storage ring. These detectors measure the stored muon beam profile throughout each fill and enable key independent cross checks of the calorimeter detector systems. This body of work presents the design, construction, testing, installation and commissioning of the straw tracking detectors as well as the ability to match the straw tracker *tracks* and calorimeter *clusters* with a focus on measuring the calorimeter pileup rate.

Table of contents

Chapter 1

Introduction

The main aim of particle physics is to understand nature at the most fundamental levels. To do so requires knowledge of the particles which comprise the world around us as well as how these particles interact with each other. Properties of these fundamental particles include mass, charge and an intrinsic form of angular momentum known as spin. As a moving charge produces a magnetic field, all charged spin-$\frac{1}{2}$ particles will have an intrinsic magnetic moment, μ, arising from their spin. The magnetic moment of particles is given by,

$$\vec{\mu} = g\frac{Qe}{2m}\vec{s}, \tag{1.1}$$

where e is the charge of the particle and Q is the sign of the charge, m is the mass, $\vec{s}$ is the particle's spin and g is the gyromagnetic ratio. The gyromagnetic ratio is a fundamental relation between the particle's spin and magnetic moment and defines how strongly a particle will interact with a magnetic field.

When Dirac proposed his relativistic theory in 1928, he predicted that free electrons have a gyromagnetic ratio of 2 [1]. The first experimental efforts to measure the gyromagnetic ratio of the electron confirmed Dirac's predictions but came with relatively large errors [2]. Around 20 years later the experimental effort had improved enough to conclude that an electron's gyromagnetic ratio exceeded 2 by around 0.12% - the first

clear indication of an anomalous contribution, a_l,

$$a_l = \frac{g_l - 2}{2}, \tag{1.2}$$

where l labels the charged leptons, e, μ, τ [3]. Importantly, it was during these 20 years that the development of relativistic quantum field theories allowed predictions of higher order effects from virtual particles emerging from the quantum vacuum and interacting with charged fermions (Tomonaga, Schwinger, Feynman, Dyson and others [4–7]). This work resulted in the calculation of the leading order (one loop diagram, shown in figure 1.1) quantum electrodynamics (QED) contribution to the anomalous magnetic moment by Schwinger, giving [8]

$$a_l^{\mathrm{QED}(2)} = \frac{\alpha}{2\pi}. \tag{1.3}$$

It is now known that this result accounts for 99 % of the anomaly with the remaining

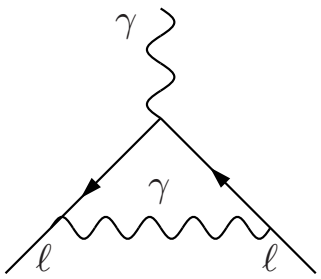

Figure 1.1: The universal lowest order QED contribution to a_l.

contribution coming from higher order QED effects as well as electroweak (EW) and hadronic (had) effects. Also, potential "new physics" effects could contribute to a_l through new particles interacting with charged fermions. Subsequently in 1961, the anomalous magnetic moment of the electron was measured with high precision, agreeing closely with the theoretical calculations [9]. But, as the sensitivity to new physics scales quadratically with the mass of the probed lepton, any interesting effects are magnified in a_μ relative to a_e by a factor $(m_\mu/m_e)^2 \approxeq 4 \times 10^4$ [10]. This makes

the anomalous magnetic moment of the muon a much better probe for possible deviations from the standard model, while the more massive τ is too short lived to allow precise measurements [11]. The anomalous magnetic moment of the muon is a very important observable in physics as it can be both measured experimentally and predicted theoretically with extremely high precision. And, as a_μ receives contributions from all forces in the standard model (and possibly contributions from beyond standard model physical processes), a highly sensitive test for new physics can be carried out by performing this measurement.

The current highest precision experimental measurement of a_μ was carried out at Brookhaven National Laboratory (BNL) in 2001 after multiple previous experiments at CERN, resulting in a world average measurement of [12],

$$a_\mu(\mathbf{exp}) = 11659209.1(5.4)_{stat}(3.3)_{sys} \times 10^{-10}, \tag{1.4}$$

where the statistical (*stat*) and systematic (*sys*) errors are given separately, showing that the measurement is statistically limited. While the standard model prediction currently stands at, [13]

$$a_\mu(\mathbf{theory}) = 11659182.04(3.56) \times 10^{-10}. \tag{1.5}$$

This creates a discrepancy between the experimental measurement and the standard model prediction of 3.7σ which, if not a statistical fluctuation, suggests the existence of a new physics process that affects a_μ [13, 14].

A new experiment, E989, has been set up at Fermi National Accelerator Laboratory with the aim of collecting 20 times the statistics of BNL and lowering the experimental uncertainty to 140 parts per billion (ppb) while parallel efforts in the theoretical community aim to calculate a_μ with comparable precision. When these experimental aims are met, if the central value of a_μ does not change the discrepancy will be greater than 5σ, as shown in figure 1.2 [15]. Many improvements have been made to the theoretical calculation recently, the following section will give a breakdown of the

current theoretical calculation pointing out the separate contributions towards a_μ^{SM} and potential contributions to $\delta a_\mu^{\mathrm{SM}}$ [13].

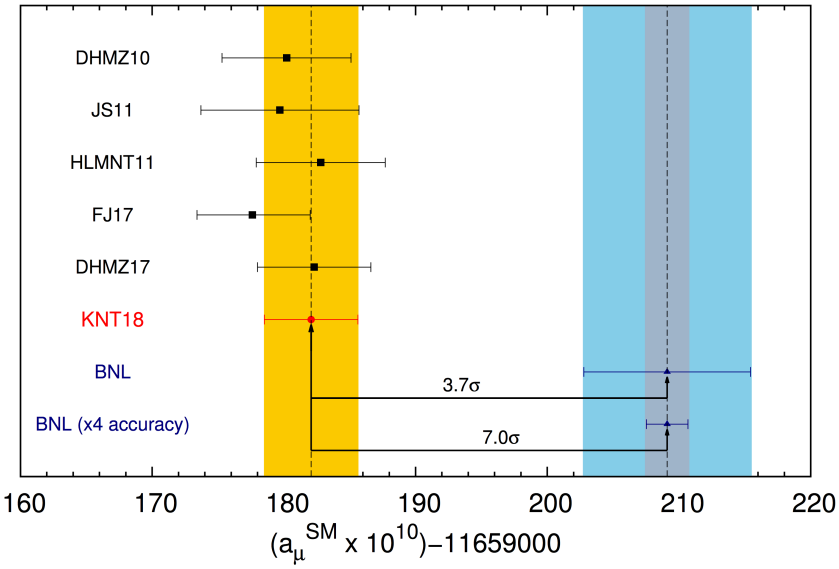

Figure 1.2: A comparison between the theoretical calculations of a_μ^{SM} and the BNL measurement showing the current experimental uncertainty in light blue and projected uncertainty in grey. The projected uncertainty shown is the four-fold improvement in uncertainty aimed for by E989, with the central value remaining the same as that from BNL [13].

1.1 Standard model contributions to a_μ

As outlined above the anomalous magnetic moment of the muon, a_μ, is composed of contributions from all sectors of the SM,

$$a_\mu^{\mathrm{SM}} = a_\mu^{\mathrm{QED}} + a_\mu^{\mathrm{EW}} + a_\mu^{\mathrm{had}}. \tag{1.6}$$

The QED contributions to a_μ^{SM} are $a_\mu^{\mathrm{QED}} = 11\,658\,471.8971 \times 10^{-10}$ which accounts for around 99.99% of the standard model anomaly, a_μ^{SM}. However, as QED is well-known perturbatively to five-loops, it only contributes 0.007×10^{-10} to the total theoretical uncertainty on a_μ^{SM}, $\delta a_\mu^{\mathrm{SM}}$. To obtain the five-loop calculation a total of 12,672 diagrams

had to be numerically calculated, which was completed by Kinoshita *et al.* [16] [17]. Figure 1.3 shows the Feynman diagrams for the 9 universal second order contributions to a_μ^{SM} while figure 1.4 shows Feynman diagrams for the typical five-loop contributions.

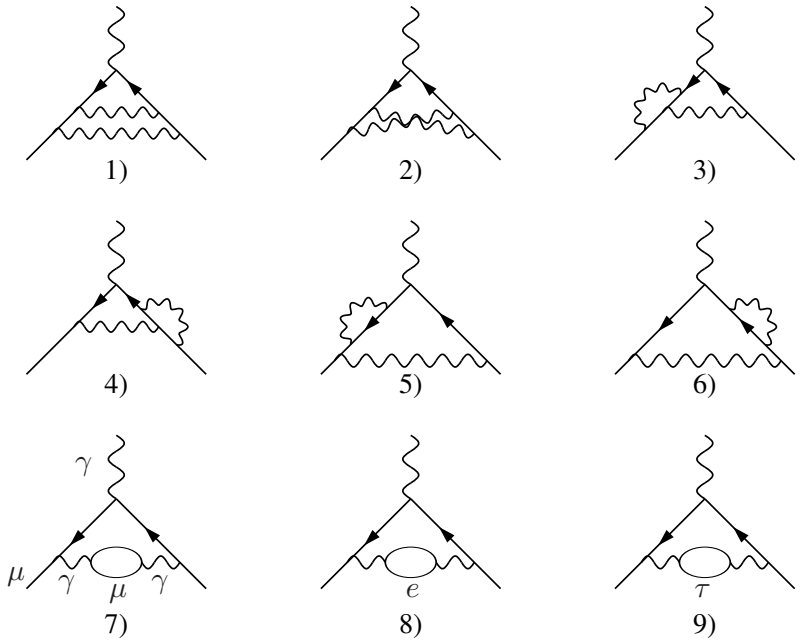

Figure 1.3: Feynman diagrams showing the 9 two loop QED processes which contribute to a_μ^{SM} [11].

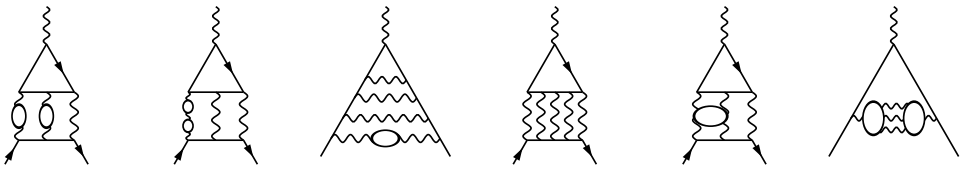

Figure 1.4: Feynman diagrams for a number of typical five-loop contributions to a_ℓ including fermion loops, diagram modified from [11].

The smallest contribution to a_μ^{SM} comes from EW interactions, where $a_\mu^{\mathrm{EW}} = 15.36 \times 10^{-10}$. This corresponds to 0.0001% of a_μ^{SM} and holds 0.2% of the overall error, $\delta a_\mu^{\mathrm{SM}} = 0.10 \times 10^{-10}$. The small contribution from the EW is due to the large mass of the W and Z bosons suppressing the effect. The Feynman diagrams showing the leading EW contributions to a_μ^{SM} are given in figure 1.5 [18][19].

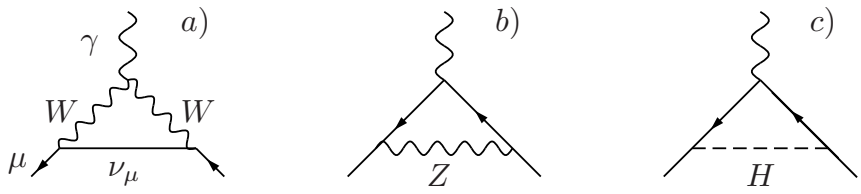

Figure 1.5: Feynman diagrams showing the leading weak contributions to a_μ^{SM} [11].

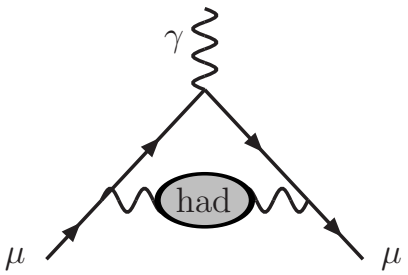

Figure 1.6: Feynman diagram showing the leading order hadronic contribution to a_μ^{SM} [11].

The majority of the uncertainty on the anomaly, $\delta a_\mu^{\mathrm{SM}}$, comes from hadronic effects a_μ^{had} which can be split into the hadronic vacuum polarisation (HVP) and hadronic light-by-light (HLbL) terms,

$$a_\mu^{\mathrm{had}} = a_\mu^{\mathrm{HVP}} + a_\mu^{\mathrm{HLbL}}. \tag{1.7}$$

Unlike the QED and EW contributions, the hadronic contribution, a_μ^{had} cannot be calculated in perturbative theory. However, the leading order (LO) HVP contribution can be connected via a dispersion relation to the cross section for e^+e^- annihilation into hadrons. The leading order hadronic contribution to a_μ is shown in figure 1.6 as coming from the hadron 'blob' (which includes all hadronic states).

Many experiments including BES-III, KLOE, CMD-2, SND and BaBar have precisely measured these cross-sections and, in doing so, have motivated multiple analyses dedicated to combing these data whilst carefully incorporating the statistical and systematic uncertainties to reach a robust determination of a_μ^{SM} [13, 20]. Of key importance to a_μ is the cross-section of the process $e^+e^- \to \pi^+\pi^-$. This channel contains the large ρ resonance which is the lowest lying resonance in terms of energy and, as

the hadronic vacuum polarisation dispersion integral has a $\sim \frac{1}{s}$ dependence, it gives a large weight to lower energies, making this channel dominant (over 70% of the total hadronic contribution to a_μ^{SM}). [21, 13, 20]

Overall, HVP is the second largest contribution a_μ^{SM}, at $\sim 0.006\%$, with $a_\mu^{\mathrm{HVP}} = 684.68 \times 10^{-10}$ [13]. However, a_μ^{HVP} contains 46% of the error on the calculated anomaly, at $\delta a_\mu^{HVP} = 2.42 \times 10^{-10}$.

The hadronic light-by-light term (with an example of these interactions given in figure 1.7) contributes $\sim$0.0001% to a_μ^{SM} at $a_\mu^{\mathrm{HLbL}} = 9.8 \times 10^{-10}$ but it contributes 53% towards $\delta a_\mu^{\mathrm{SM}}$ with a uncertainty of $\delta a_\mu^{HLbL} = 2.6 \times 10^{-10}$ [22] [23]. Like HVP, HLbL also cannot be calculated in perturbative theory but differs from HVP as it has only been possible up until now to fully determine it using models. The presented value for δa_μ^{HLbL} was determined by a global collaboration of theorists, this determination is known as the 'Glasgow Consensus' [22].

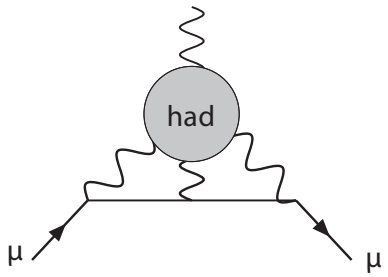

Figure 1.7: Feynman diagram showing hadronic light-by-light process [11]

Adding together each contribution (in units of $\times 10^{-10}$) gives the total theoretical calculation, a_μ^{SM},

$$a_\mu^{\mathrm{SM}} = (\underbrace{11658471.8971 \pm 0.007}_{\mathrm{QED}} + \overbrace{15.36 \pm 0.10}^{EW} + \underbrace{684.68 \pm 2.42}_{HVP} + \overbrace{9.8 \pm 2.6}^{HLbL}), \quad (1.8)$$

giving,

$$a_\mu^{\mathrm{SM}} = (11659182.04 \pm 3.56) \times 10^{-10}. \quad (1.9)$$

Comparing this with the worlds best experimental measurement of a_μ shows the discrepancy between experiment and theory,

$$\begin{aligned} a_\mu(\textbf{exp}) &= 11659209.1(6.3) \times 10^{-10}, \\ a_\mu(\textbf{theory}) &= 11659182.04(3.56) \times 10^{-10}, \\ a_\mu(\textbf{exp}) - a_\mu(\textbf{theory}) &= 27.06 \pm 7.26 \times 10^{-10}, \end{aligned} \tag{1.10}$$

This difference currently stands at 3.7σ, as shown in figure 1.2. Soon the physics community will be presented with a new experimental measurement in the form of the Fermi National Accelerator Laboratory muon g-2 experiment, which aims to find if the cause of this discrepancy is from statistical fluctuations, previous experimental issues, misunderstandings in the theoretical uncertainties or new physics.

1.2 Possible new physics contributions to a_μ

There are multiple beyond standard model (BSM) theories which aim to understand this discrepancy. In general, the contribution to a_μ decreases as the mass scale of the new physics process increases. One BSM explanation that has been considered is supersymmetry (SUSY). If SUSY exists the super-partner particles would also contribute towards a_μ. The contribution towards a_μ from SUSY is approximately,

$$a_\mu^{\text{SUSY}} \approx 13 \times 10^{-10} \left(\frac{100\text{GeV}}{M_{\text{SUSY}}}\right)^2 \tan\beta \ \text{sign}(\mu), \tag{1.11}$$

where M_{SUSY} is the mass of the SUSY particle, $\tan\beta$ the ratio of the two Higgs vacuum expectation values and μ is the mass parameter for the supersymmetric Higgs boson. Given this approximation, the observed value of a_μ could be explained with SUSY particles of roughly 200 GeV with a $\tan\beta \approx 10$ or SUSY particles of roughly 500 GeV with a $\tan\beta \approx 50$. Leading supersymmetric contributions to a_μ come from sneutrino-chargino and smuon-neutralino loops, as shown in figure 1.8.

For an in-depth discussion on BSM contribution to a_μ see [24–27, 11].

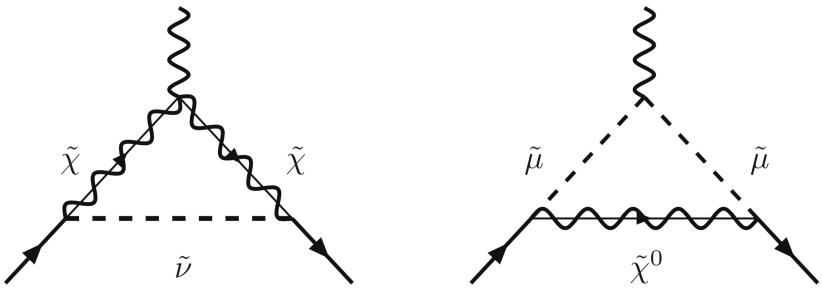

Figure 1.8: Leading SUSY contributions to g-2 coming from sneutrino-chargino and smuon-neutralino loops when considering a supersymmetric extension of the standard model [26, 11].

1.3 Overview

This work will cover the history of the experimental effort into measuring the muon g-2, in Chapter 2, showing the improvements made at each new experiment. The experimental technique is outlined in Chapter 3 before presenting the Fermi National Accelerator Laboratory g-2 experiment in more detail in Chapter 4. In the Fermi National Accelerator Laboratory g-2 experiment a key improvement over its predecessor, E821, will come from the use of new straw tracking detectors positioned around the ring. The key benefits of using these straw trackers will be explained in 5 with the construction of these detectors being shown in Chapter 6. One of the key benefit of the straw trackers focused on in this work will be the ability to match the straw tracker *tracks* with the calorimeter *clusters*. This allows many indispensable analyses to be carried out, some of which will be shown in Chapter 7.

The author has made key contributions to many of the areas outlined in this work. These include the design, construction, testing, installation, commissioning and running of the straw tracking detectors at the University of Liverpool as well as at Fermi National Laboratory. Included in this is the development of the high voltage monitoring and control software, tests of material used within the detector to ensure long term stability as well as a device to non-invasively measure and record the tension of the sense wire inside each straw. Development was also made to the straw tracker data quality monitoring software which provides the ability to monitor the performance

of the detector in near real-time as well as displaying key measurements made by the trackers. The latter are useful for experimental diagnostics, beam tuning as well as everyday running of the experiment. Another substantial area of work involved writing software in the *art* software framework [28] to match extrapolated tracks to calorimeter clusters to enable comparisons between the detector systems. This work resulted in using the matched tracks and clusters taken during the first physics quality data run to identify pileup in the calorimeters. In this the composition of the events was determined as well as the time spectrum. These were used together with a simulation tool to determine the effect on the measurement from these events.

Chapter 2

History of the Muon g-2 Measurements

This chapter will give an overview of the discovery of the muon as well as the history of the muon g-2 measurements, showing the incremental improvements made by both the multiple different experiments and the theoretical predictions. A brief outline of the experimental procedure developed to measure the anomalous magnetic moment of the muon will be given and expanded on in more detail in Chapter 3.

2.1 The discovery of the muon

The first published observation of the muon was unknowingly made by Kunze in 1933 using a Wilson cloud chamber [29]. At the time Kunze reported that 'The nature of this particle is unknown; for a proton the ionisation is probably too small, and for a positive electron too large'. It was later reported by Anderson and Neddermeyer in 1936 that they had observed particles 'less massive than protons' but 'more penetrating than electrons' while imaging cosmic rays using a cloud chamber at both sea level and an elevation of 4300 meters [30]. This particle was confirmed by many other experiments over the following years and in 1941 Christy and Kusaka presented their findings that

their '[...] evidence thus favours spin 0, or possibly spin half, but tends to exclude spin 1.' [31].

During the 1950's advances in accelerator technology led to the invention of the synchrotron, these accelerators made it possible to produce proton beams with enough energy to create pions and therefore muons in the laboratory. One key aspect of the pion decay is that it creates polarised muons, this is presented in more detail in section 3.0.1. This experimental advance allowed many experiments to study the properties of the muon. In 1953 Fitch and Rainwater carried out experiments using the 164-inch Columbia-Nevis Cyclotron to create and study the properties of exotic atoms where a μ^- orbits about a positive nucleus. They announced that the results could be explained if "[...] the μ^- meson is a spin $\frac{1}{2}$ Dirac "heavy electron" of 210 electron masses, having the expected Dirac magnetic moment and having no strong non-electromagnetic interaction with nuclear matter." [32]. This experiment represents the first attempt to measure the magnetic moment of the muon.

2.2 History of muon g-2 measurements

In 1958 *European Organisation for Nuclear Research* (CERN) launched the g-2 experiment with the aim of measuring the anomalous magnetic moment of the muon, a_μ. At the time there had been no direct measurement of a_μ, but it was known indirectly to an accuracy of about 10% [33]. Over the next 40 years, three experiments at CERN and one at Brookhaven National Laboratory measured a_μ with increasing precision. These experiments shared the same basic principle of measuring the frequency at which the spin vector precesses relative to the momentum vector, referred to as the anomalous precession frequency, ω_a. As, importantly, ω_a only depends on a_μ rather than g_μ, if a frequency varying with ω_a is recorded then this only relates to the quantum-loop effects, more details about this are given in Chapter 4.

At this time the main difficulty in making the measurement was being able to store muons in a magnetic field while they make many turns. This process was studied

heavily prior to the first CERN experiment using a 83cm x 52cm x 10cm magnet borrowed from the University of Liverpool. However, due to the size of the magnet only ~ 30 turns were possible before the muons reached the other end of the magnet [34]. It did however make it possible to lower the limit on the electric dipole moment of the muon by nearly a factor of 10 to $(1.1 \pm 0.9) \times 10^{-15}\ e \cdot \text{cm}$ [33] [35].

CERN I

To obtain many more turns using the same technique, a magnet of the same width but six metres long providing a magnetic field of 1.58 T was constructed in the experimental hall of the CERN Synchro-Cyclotron (shown in figure 2.1 and 2.2). In 1960 this experiment, referred to as CERN I, was able to store muons for up to one thousand circular orbits while they drifted along the horizontal axis of the magnet. The spin directions of each surviving muon were measured by stopping the muons in an absorber and recording the decay electrons in forward and backward counters. This experiment provided a measurement of $a_\mu(\text{exp}) = 0.001162(5)$ which agreed well with the theoretical value at that time of $a_\mu(\text{theo}) = 0.001165(5)$ [33] [36] [37].

CERN II

After the success of CERN 1 measurement the role of the muon g-2 measurement as the best measure of QED at short distances had been firmly established. In order to search for new interaction characteristics of the muon it was highly desirable to design the next generation of experiment which could push the measurement accuracy to new levels. CERN II was set up to achieve this where the operating principle of the experiment was improved to utilise a weak-magnetic-focusing storage ring. Pions were produced in a target on the entrance to the ring so muons would be created inside the storage volume itself - greatly increasing the stored muon intensity. It was also advantageous to use the new CERN Proton-Synchrotron to generate high-energy muons and by taking advantage of relativistically dilated lifetimes a higher number of cycles can be observed, as the g-2 precession frequency is unaffected by time dilation. This

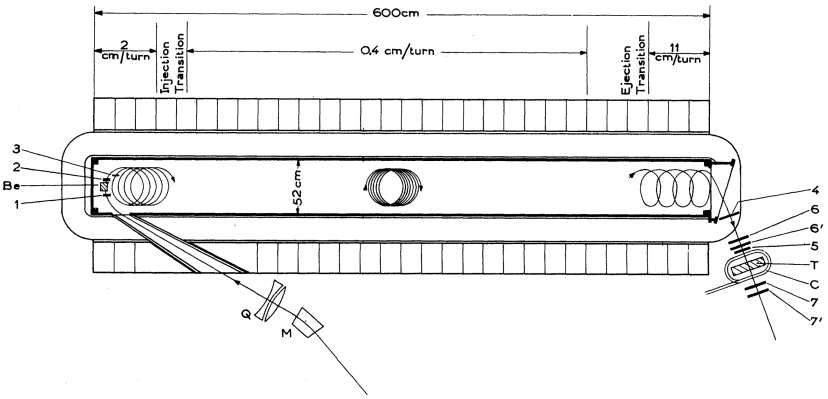

Figure 2.1: General plan of the 6-metre magnet. M: bending magnet; Q: pair of quadrupoles; 1, Be, 2, 3: injection assembly consisting of Be-moderator and counters 1, 2, 3; T: methylene-iodide target; counters 6,6',7,7': backward and forward electron telescopes [37].

Figure 2.2: From left to right: Johannes Cornelius Sens, Georges Charpak, Théo Müller, Francis Farley (standing) and Antonino Zichichi on the 6 metre long magnet at CERN in 1960.

method reduced the uncertainty on the experimental value by a factor of 16 revealing a quantitative discrepancy with the theoretical prediction, thus prompting theorists to recalculate their predictions. The result averaged over both muon polarities was $a_\mu = 116616(31) \times 10^{-8}$ (270 ppm), where the difference between this experimental result and theory prediction was $a_\mu(\text{exp}) - a_\mu(\text{theo}) = 28(31) \times 10^{-8}$. The magnetic storage ring used for this measurement had a 5 m diameter and provided a magnetic field strength of 1.72 T [36]. The limiting factor of this experiment was the magnetic field gradients required to vertically focus the muons, this destroyed the homogeneity of the magnetic field introducing a large systematic error on the measurement of the average magnetic field which the muons experienced.

CERN III

The method was improved again at the CERN III experiment in 1974 where a 14m diameter storage ring was installed into the South-East hall of the CERN Super-Proton-Synchrotron (SPS). CERN III used focusing electrostatic quadrupoles within the ring to keep the beam vertically aligned. This allowed a more precise determination of the magnetic field. The largest improvement from the previous measurement arose from increasing the relativistic factor, γ, from 12 to 29.3, this value was chosen to remove the effect of the electric fields on the spin precession frequency and also increased the number of (g-2) oscillations per muon lifetime, as discussed in Chapter 4. The final results were published in 1979 for both μ^+ and μ^- with an overall average of $a_\mu = 1165924(8.5) \times 10^{-9}$ (7.3 ppm) and confirmed the theoretical predictions of the first-order hadronic loop contributions to a_μ [38].

Brookhaven National Laboratory

Brookhaven National Laboratory continued the measurement of the anomalous magnetic moment of the muon in 1997, designated as "E821". E821 is based on the same experimental principles as CERN III with the goal of a 20-fold improvement in the error. The Brookhaven Alternating Gradient Synchrotron (AGS) provided an increase of

muon flux by a factor of 200 over the CERN SPS which greatly reduced the statistical error. Another major improvement was moving from pion injection to muon injection, allowing for a large improvement in the level of statistics recorded. In 2000 BNL released the measurement of $a_{\mu+}$ with a result of $a_\mu = 11659204(9) \times 10^{-10}$, the wiggle plot recorded for one of the data taking periods is given in 2.3 [39] [38]. This stands as the current world's best measurement of a_μ.

Overall, a_μ(exp) stands at $11659208.0(6.3) \times 10^{-10}$ which corresponds to a measurement precision of 0.54 ppm [12]. The results gained from these measurements of a_μ are shown in figure 2.4.

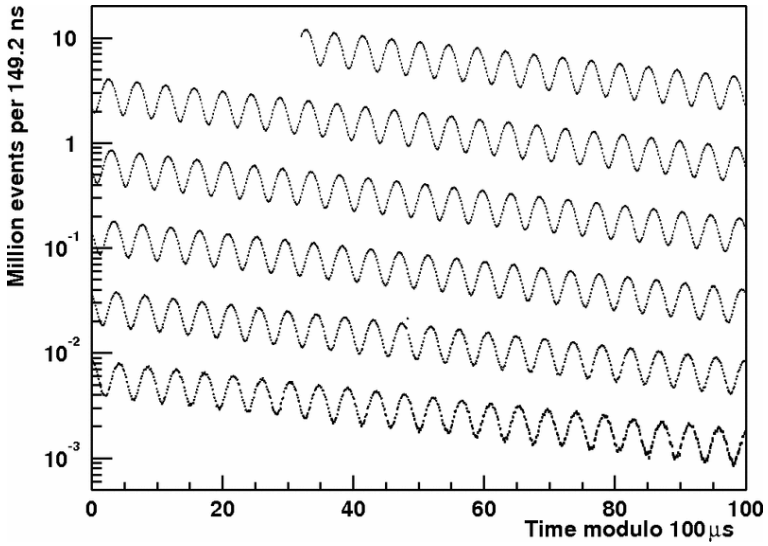

Figure 2.3: Distribution of electron counts versus time for the 3.6×10^9 muon decays in the R01 μ^- data-taking period at BNL. The data is wrapped around modulo 100 μs. [39]

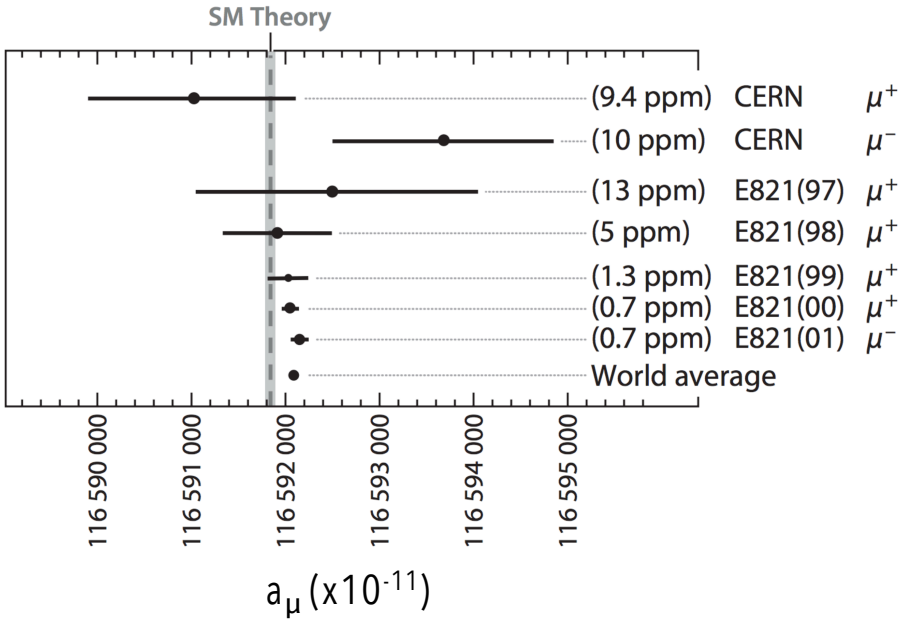

Figure 2.4: Measurements of a_μ with the uncertainty given compared to the SM theory prediction. [19]

Chapter 3

Experimental Technique

The experimental principle used for the Fermilab E989 experiment is mostly unchanged from the E821 muon g-2 experiment as well as the late CERN measurements, as covered in Chapter 2. This principle relies on two frequencies being measured experimentally, the rate at which the muon spin vector turns relative to the momentum vector called the muon anomalous precession frequency, ω_a, and the strength of the magnetic field as measured by the Larmor frequency of a free proton, ω_p. To achieve this an intense beam of polarised relativistic muons are injected and stored in an extremely precise magnetic field. Because of parity violation in the weak decay of the muon, a correlation exists between the muon spin and decay electron direction, resulting in the highest energy positrons being preferentially emitted in the direction of the muon spin. Therefore, measuring the arrival time of positrons above a certain energy threshold allows the anomalous precession frequency, ω_a, to be determined. The value of the magnetic field felt by the stored muons around the ring is measured using indexable probes. These measurements are then weighted by the muon distribution to determine $\widetilde{\omega}_p$ and used along with the muon anomalous precession frequency, ω_a, to determine a_μ. It is important to note that the contribution from a non-zero electric dipole moment is assumed to be negligible.

3.0.1 Determining ω_a

The equation of motion for a charged particle moving at relativistic velocities in a external magnetic and electric fields is given by,

$$\dot{\vec{p}} = \vec{\omega}_c \times \vec{p} = q\left(\vec{\beta} \times \vec{B} + \vec{E}\right), \tag{3.1}$$

where the cyclotron frequency, $\vec{\omega_c}$, is given by,

$$\omega_c = \frac{Qe}{m_\mu}\left[\frac{1}{\gamma}\vec{B} - \frac{\gamma}{\gamma^2 - 1}\left(\vec{\beta} \times \vec{E}\right)\right]. \tag{3.2}$$

Here the external magnetic field is the main dipole field of the storage ring, assumed here to be $\vec{B} = (0, B_y, 0)$. While the electric field is due to the electrostatic quadrupoles used to vertically focus the muon beam. This field has radial and vertical components, $\vec{E} = \left(E_x\left(\vec{r}\right), E_y\left(\vec{r}\right), 0\right)$

The spin of the muon in the external magnetic and electric field is also explained by an equation of motion, referred to as the Bargmann-Michel-Telegdi (BMT) equation [40],

$$\vec{\omega_s} = \frac{Qe}{m_\mu}\left[\left(\frac{g_\mu}{2} - 1 + \frac{1}{\gamma}\right)\vec{B} - \left(\frac{g_\mu}{2} - 1\right)\frac{\gamma}{\gamma+1}\left(\vec{\beta}\cdot\vec{B}\right)\vec{\beta} - \left(\frac{g_\mu}{2} - \frac{\gamma}{\gamma+1}\right)\left(\vec{\beta}\times\vec{E}\right)\right] \tag{3.3}$$

Taking the difference between the the cyclotron frequency, $\vec{\omega_c}$, and the spin precession frequency, $\vec{\omega_s}$, (equations 3.2, 3.3) gives the anomalous spin precession frequency, $\vec{\omega_a}$,

$$\vec{\omega_a} = \frac{Qe}{m_\mu}\Bigg[a_\mu\vec{B} - a_\mu\left(\frac{\gamma}{\gamma+1}\right)\underbrace{\left(\vec{\beta}\cdot\vec{B}\right)}_{\vec{\beta}\cdot\vec{B}=0}\vec{\beta} - \overbrace{\left(a_\mu - \frac{1}{\gamma^2-1}\right)}^{\gamma=\gamma_{magic}}\left(\vec{\beta}\times\vec{E}\right)\Bigg], \tag{3.4}$$

where e is the charge on the muon and Q is the sign of the charge, m_μ is the mass of the muon, $\gamma = 1/\sqrt{1-\nu^2/c^2}$ is the relativistic Lorentz factor.

There are two important assumptions that can be made which are under and over-braced in equation 3.4. First, assuming that the stored muon beam motion

stays perpendicular to the main dipole storage field removes the $\vec{\beta} \cdot \vec{B}$ term. A small contribution remains which arises from a fraction of muons which do not remain perpendicular to the magnetic field, this correction is called the *pitch correction*.

The second assumption made is that the γ of the muons can be chosen as to remove the $\vec{\beta} \times \vec{E}$ term which comes from using electric fields in the storage ring. This "magic" gamma, or "magic" momentum, is chosen so $a_\mu - 1/(\gamma^2 - 1) = 0$ and ω_a therefore becomes independent of $\vec{E}$. This magic momentum, $\gamma_{magic} = \sqrt{(1 + a_\mu/a_\mu)} \simeq 29.378$ which makes the time dilated muon lifetime 64.435 μs from the rest lifetime of 2.197 μs. Consequently this lifetime becomes long enough to observe multiple oscillations of the anomalous precession frequency ~ 4.4 μs as well as enabling the measurement to be possible in a storage ring of reasonable size, approximately 14 m diameter. Again, this second assumption is not entirely true for all muons as a fraction of the stored muons do not have the magic momentum, this correction is called the *radial E-field correction*. For E821 these two corrections together came to introduce a 0.03 ppm systematic error. Removing these terms reduces ω_a from equation 3.4 down to,

$$\vec{\omega_a} = \frac{Qe}{m_\mu} a_\mu \vec{B}. \tag{3.5}$$

An important feature of the anomalous spin precession frequency is that it depends on the anomalous magnetic moment of the muon a_μ rather than g_μ, therefore relating directly to the quantum-loop effects only. It is also worth noting that if the muon just had its Dirac magnetic moment of $g = 2$, then $a_\mu = 0$ and the spin would follow the momentum turning at the cyclotron frequency, $\omega_s = \omega_c$.

Measuring the muon spin direction from ω_a

Pions decay via the parity violating weak interaction, as shown in figure 3.1 and figure 3.3. It is thought that only left-handed neutrinos exist meaning that the neutrino spin vector is anti-parallel to its momentum vector. The opposite is true for anti-neutrinos which are right handed so have their spin vector parallel to its momentum vector. Since

the pion is spin-0 the spin of the muon is required to be anti-parallel to the neutrino (to conserve angular momentum), conveniently resulting in spin polarised muons.

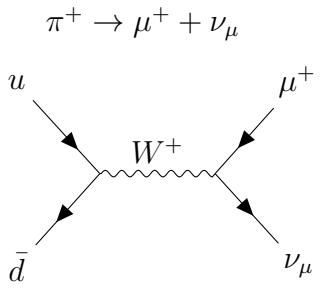

Figure 3.1: Pion decay Feynman diagram

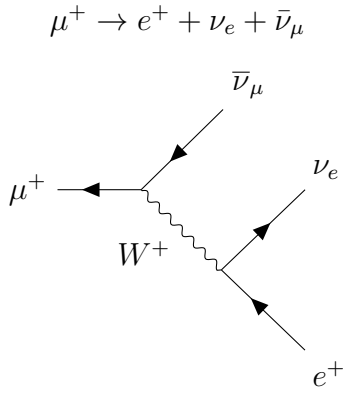

Figure 3.2: Muon decay Feynman diagram

The muon also decays via the parity violating weak interaction, shown in figure 3.2 and 3.4, meaning that the weak force only couples to particles that are left-handed and anti-particles that are right-handed. This handedness refers to chirality but in the massless limit this chirality handedness is equal to helicity in which left-handed particles have their spin and momentum anti-parallel to each other while right-handed particles have their spin and momentum parallel. The neutrinos in the muon decay can be thought of as massless so the ν_e particle is left-handed while the $\bar{\nu}_\mu$ anti-particle is right handed. This means that the two neutrinos have their spin opposite to each other and due to spin angular momentum conservation results in the positron preferentially having its spin in the same direction as the muon's spin. As the positron is right handed its momentum vector is along the same direction as its spin vector. Therefore the positron is preferentially emitted in the same direction as the muon spin, with the highest energy positrons being emitted in the direction of the muon's spin. So measuring the average direction of the highest energy electrons over time enables the spin precession of the muon sample to be determined.

In the lab frame the differential probability for the electron to be emitted with normalised energy $y = E/E_{max}$ (where E_{max} is 3.1 GeV) with the angle between the emitted direction and the muon spin, θ, is

$$\begin{aligned} \frac{dP}{dyd\Omega} &= \left(\frac{1}{2\pi}\right) N(y)\left[1 - A(y)\,cos\theta\right] \\ \text{where } N(y) &= y^2(3-2y) \\ A(y) &= \frac{q}{e}\frac{2y-1}{3-2y} \end{aligned} \tag{3.6}$$

Figure 3.5 shows the relative number (N) and asymmetry (A) distributions versus energy [12]. Here the differential quantity NA^2 gives the relative weight by electron energy to the ensemble average figure-of-merit where the statistical uncertainty of measuring ω_a is inversely proportional to NA^2, showing the importance of the higher-energy electrons in reducing the measurement statistical uncertainty.

There are 24 calorimeters inside the storage ring, shown in figure 3.6, which are responsible for measuring the arrival time and energy of the decay positrons. Using this information it is possible to place an energy cut on the positrons detected to ensure a sample of forward decay positrons are recorded. Along with this information the stored muon distribution must also be measured to allow the determination of the magnetic field felt by this ensemble of particles. The muon distribution is measured using the straws tracking detectors by recording the positron decay trajectory and extrapolating this backwards to the muon decay point.

The number of decay positrons with energy greater than E at a time after muon injection, t, is given by,

$$N(t) = N_0(E)e^{(-t/\gamma\tau_\mu)}\left[1 + A(E)cos(\omega_a t + \phi(E)),\right] \tag{3.7}$$

where $N_0(E)$ is a normalisation factor, τ_μ is the muon rest frame lifetime, and $A(E)$ is the asymmetry factor for positrons of energy greater than E. Figure 2.3 shows the positron arrival time data recorded by the calorimeters from the E821 experiment, it is

possible to see the g-2 modulation on top of the muon exponential decay and how ω_a can be determined from this data given equation 3.7 [11].

3.0.2 Measuring ω_p

As shown in equation 3.4 in addition to measuring the arrival time of decay positrons the magnetic field experienced by the muons has to be precisely measured. This is carried out by a Nuclear Magnetic Resonance (NMR) system that is capable of determining the magnetic field to better than 100 ppb by measuring the Larmor frequency of a free proton ω_p while in the storage field. The relation between the magnetic field strength, B, and ω_p is shown in equation 3.8, where μ_p is the proton magnetic moment.

$$B = \frac{\omega_p}{2\mu_p}. \tag{3.8}$$

In order to measure the field in the storage region a trolley fitted with NMR probes travels around the storage ring taking measurements. There is also a plunging probe which determines the field in the storage region at a position measured by the trolley probes. As the plunging probe is calibrated against a special, spherical probe of H_2O, a cross-calibration between the sample probe, plunging probe and trolley probes can be carried out. The NMR probes measure ω_p by using a $\pi/2$ RF pulse to rotate the proton spin with the resulting free-induction decay being detected by a pick-up coil around the sample, more information about the experimental hardware required to measure the magnetic field will be given in section 4.5.

3.0.3 Determining a_μ

It is important to point out that it was chosen to measure the magnetic field via ω_p rather than in Tesla directly as if using B with equation 3.4 as precise knowledge of the muon charge to mass ratio is also required in that case [11]. Now a_μ can be expressed

in terms of the Larmor frequency of a free proton ω_p and ω_a through,

$$a_\mu = \frac{R}{\lambda_+ - R} \text{ where } R = \omega_a/\omega_p \text{ and } \lambda_+ = \mu_{\mu^+}/\mu_p, \tag{3.9}$$

where μ_{μ^+}/μ_p is the muon-to-proton magnetic moment ratio. Measurements made of muonium (the μ^+e^- atom) hyperfine splitting allow the value of λ to be determined precisely,

$$\lambda_+ \; = \; \mu_{\mu^+}/\mu_p \; = \; 3.183 \;\; 345 \;\; 137 \;\; (85). \tag{3.10}$$

This measurement can be used with ω_p and ω_a in equation 3.9 to determine a_μ. It is also key to point out that using λ_+ to determine a_{μ^-} requires the assumption of CPT invariance, where,

$$a_{\mu^+} = a_{\mu^-} \text{ and } \lambda_+ = \lambda_-. \tag{3.11}$$

The comparison of R_{μ^+} with R_{μ^-} provides a high precision CPT test. This was carried out by E821 where they found, [12]

$$\Delta R = R_{\mu^-} - R_{\mu^+} = (3.6 \pm 3.7)10^{-9}. \tag{3.12}$$

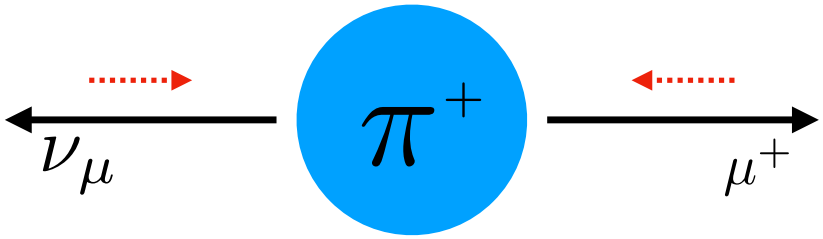

Figure 3.3: Diagram showing pion decay where the black arrows denote the momentum vectors while the red arrows denote the spin-vectors.

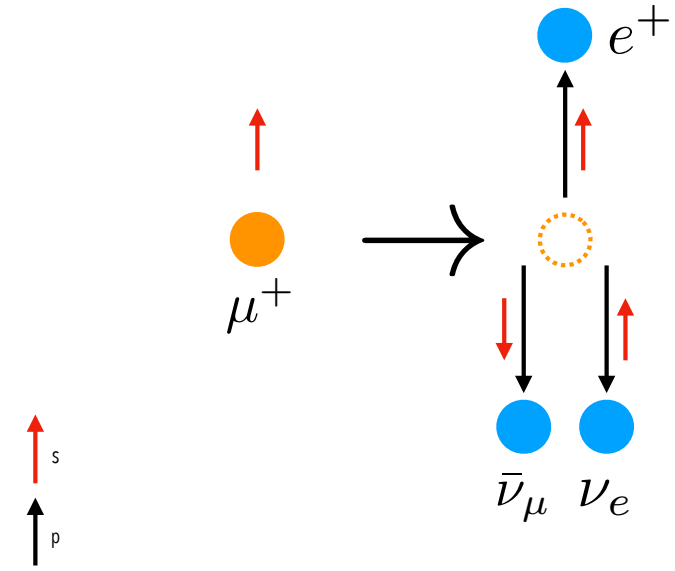

Figure 3.4: Diagram showing the decay of a muon with the decay products having their momentum vectors and spin vectors labelled, the black arrows denote the momentum vectors while the red arrows denote the spin-vectors.

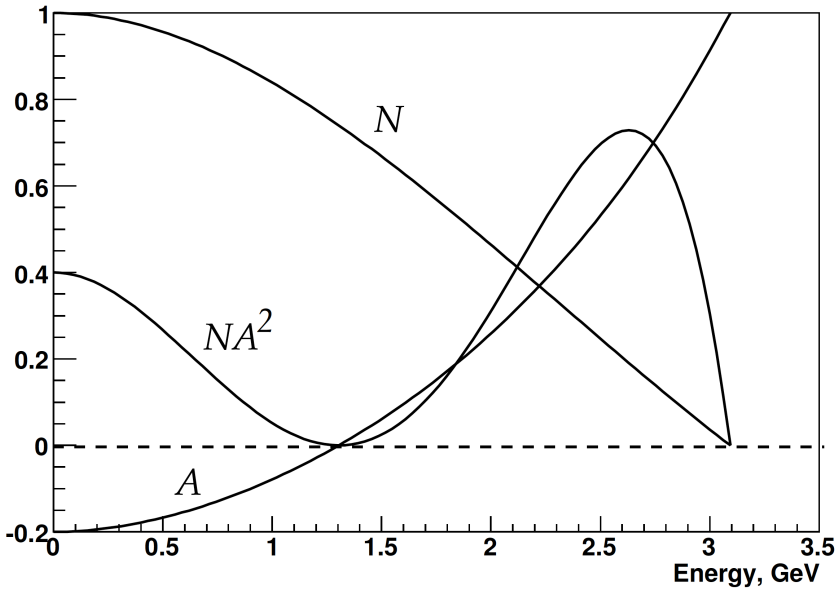

Figure 3.5: Relative number and asymmetry distribution versus energy of the electron in the laboratory frame.

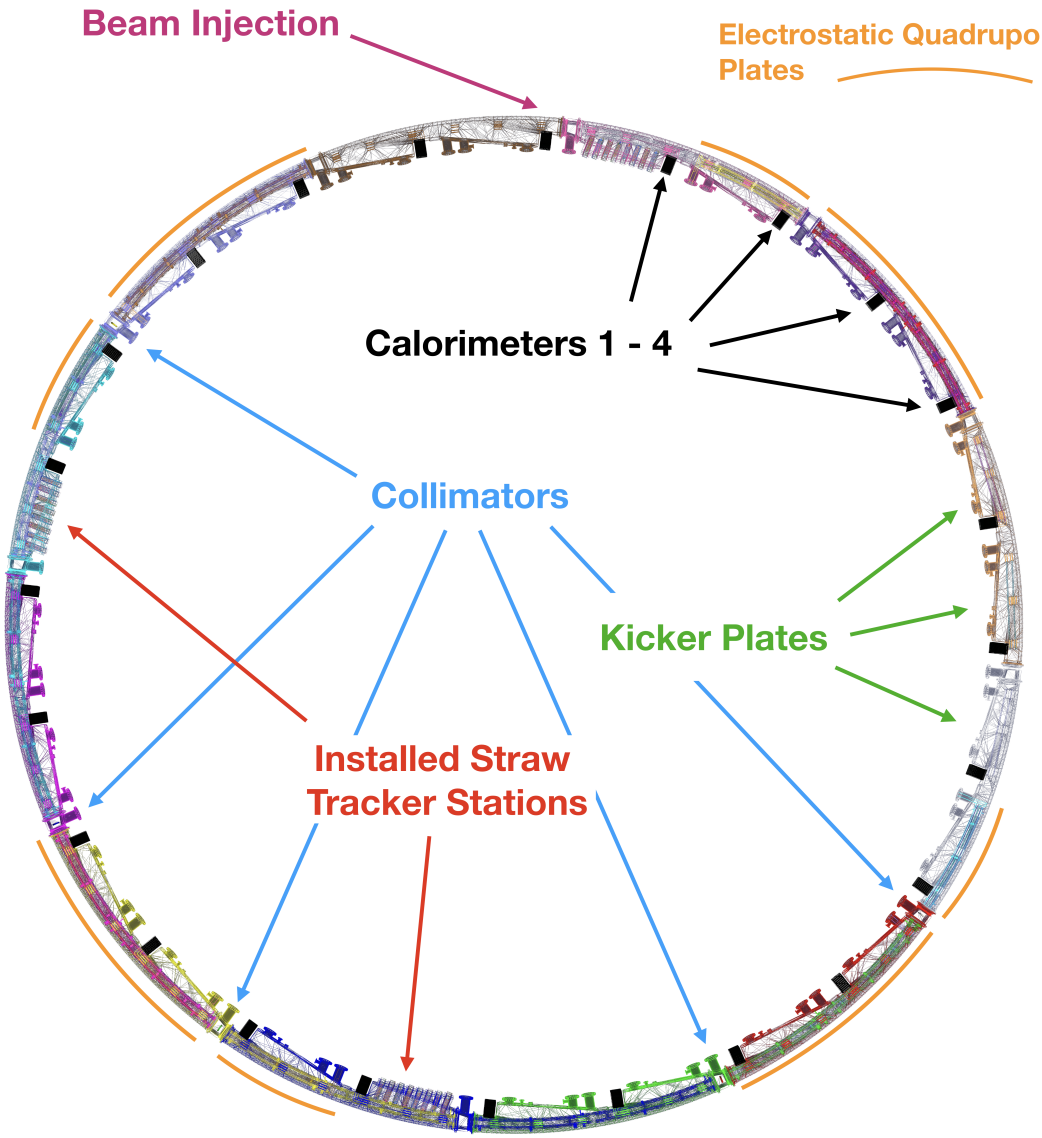

Figure 3.6: Diagram showing a wireframe model of the storage ring vacuum chambers and key experimental components. This model was produced from the geometries used in the g-2 ring simulation.

Chapter 4

Fermilab g-2 Experiment

In 2001, after the previous muon g-2 measurement at Brookhaven National Laboratory, a $\sim 3\sigma$ deviation between the experimental results and theoretical prediction remained. To answer this outstanding question a new muon g-2 experiment at Fermi National Accelerator Laboratory (FNAL) was designed with the overall aim to reduce the error on the measurement to 0.14ppm - a factor 4 improvement over the previous measurement. An overview of the experimental technique was given in Chapter 3, here each of the key experimental apparatus used at FNAL will be explained with a focus on how each can help to reduce the overall systematic error. The straw tracking detectors will be mentioned but focussed on in more detail in Chapter 5 as this detector system is the major focus of the work presented.

4.1 Producing the polarised muon beam

To reach the statistical uncertainty of 0.1 ppm, 1.8×10^{11} positrons above 1.8 GeV have to be recorded. This translates to a total of 4×10^{20} protons on target and 1.1×10^{3} positrons recorded above the 1.86 GeV threshold per fill. Running with these statistics it will take approximately 400 days to collect the data required.

Many different stages are required to generate, transport and inject the high intensity muon beam at FNAL, the path of the beam lines used to achieve this at FNAL in figure 4.1. These stages include;

- Production of the high intensity proton beam using the Booster and Recycler rings.
- Directing the proton beam at a target to create secondaries (including pions).
- Momentum selecting the secondaries and direct the beam towards delivery ring, at this point the main components of the beam are protons, muons and pions.
- Allow the beam to circulate around the delivery ring where any remaining pions decay to muons and the muons and protons physically separate.
- Kick the protons out of the delivery ring while allowing the muons to continue to travel downstream towards the MC1 building.
- Focus the muon beam to allow it to travel though the narrow superconducting inflector and into the storage ring.

Booster and recycler rings

The FNAL Booster is supplied with 400 MeV protons and produces 8 GeV protons in batches. Four Booster proton batches are directed down the MI-8 line and injected into the Recycler ring every 1.4s. Each of the four batches are re-bunched in the recycler into four bunches with an average intensity of 1×10^{12} protons per bunch and are produced temporally narrow enough to fit in the MC1 storage ring (< 147 ns). Bunches are directed one at a time down the P1, P2 and M1 lines to the g-2 Target Station located in the AP0 hall. Figure 4.2 shows the time structure of beam pulses used for E989 [41] [14].

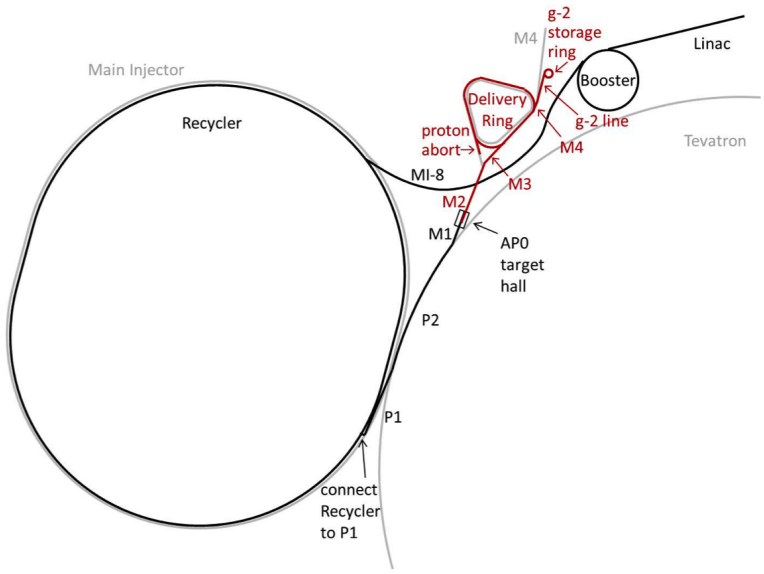

Figure 4.1: Overview of the beam line from production at the Linac to injection into the g-2 storage ring.

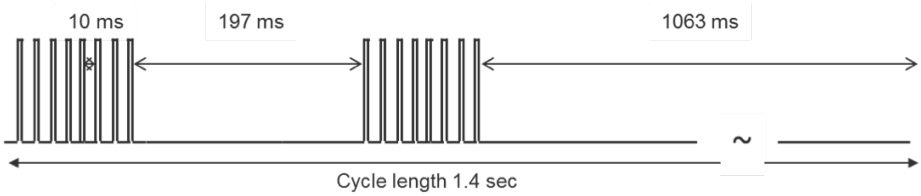

Figure 4.2: Figure showing the beam timing structure for injection into the g-2 storage ring.

Target and secondary momentum selection

The production target station consists of five main devices: the pion production target, the lithium lens, a collimator, a pulsed magnet and a beam dump. The target is constructed with a solid Inconel 600 core and has a radius of 5.715 cm with a typical chord length of 8.37 cm and was designed to produce a yield of approximately 1×10^{-5} π^+ within $\frac{dp}{p} < 2\%$ per proton on target (POT). The secondary beam from the target is focussed using a lithium collection lens which provides strong isotropic focusing to divergent secondaries. Positively-charged particles leaving the lithium collection lens are then momentum-selected centred around a momentum of 3.115 GeV/c ($\pm$ 10%) using a

Table 4.1: Beam target parameters.

Parameter	
Proton intensity (per pulse)	1×10^{12}
Total POT (per cycle)	16×10^{12}
Number of pulses per cycle	16
Cycle length	1.33 s
Primary energy	8.89 GeV
Secondary energy	3.1 GeV
Beam power at target	17.2 kW
Beam size at target	0.15-0.30 mm
Selected particle	π^+
|dp/p| (PMAG selection)	10%

pulsed dipole magnet (PMAG) and a collimator. The momentum selected particles are bent through 3° and directed down the M2 and M3 lines which capture particles with momentum 3.094 GeV/c. Particles which are not momentum-selected continue forward and are absorbed into the target-vault beam dump [42]. Key parameters for the target station are summarised in table 4.1. The pions created during the proton interaction with the target undergo weak decay to polarised muons as outlined in section 3.0.1.

Delivery ring and routing to MC1

The composition of the beam on entry to the delivery ring is mostly protons, pions and muons. One key improvement for the FNAL g-2 experiment is the use of the delivery ring which is designed to allow the pions to decay to muons as well as removing the protons from the beam, leaving a clean muon beam injection into the storage ring. It does this by directing the beam around the delivery ring four times which allows the pions to decay to muons, through the process given in figure 3.3, leaving muons and protons in the beam. As the protons in the beam have a higher mass they travel slower than the muons which results in a debunching effect after four cycles around the delivery ring. The protons become physically separated by approximately 180 ns allowing a kicker magnet to kick the protons out of the beam, this can be seen in figure 4.3. The muon beam is then directed towards the MC1 experimental hall through the

M4 and M5 lines where the beam undergoes the final focus using magnetic quadrupoles before entering the inflector and on into the g-2 storage ring.

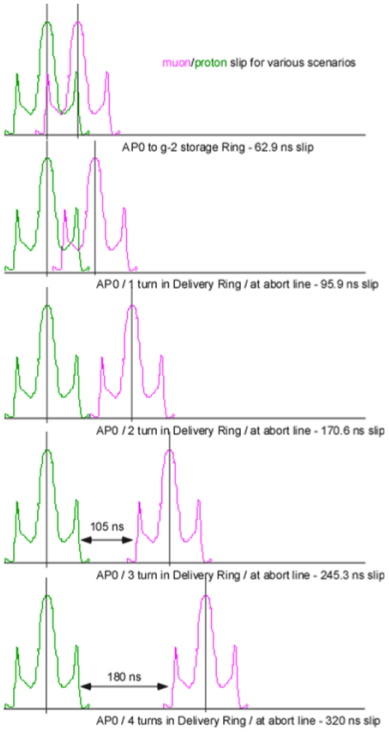

Figure 4.3: Separation of the muons *(pink)* and protons *(green)* after circulating the delivery ring multiple times.

4.2 The magnetic storage ring

The magnetic storage ring is responsible for creating the magnetic dipole field for the experiment. It is built as one continuous superferric magnet, which is where an iron magnet is excited by superconducting coils. The field created is designed to be vertical and uniform at a central value of 1.4513 T. A cross-section of the magnet is shown in figure 4.4 where it is possible to see the three superconducting coils, iron yoke, the pole pieces, the 'air gap' between the yoke and pole pieces as well as the storage region. When constructed the ring is around 3 m tall, 15 m in diameter and has a radius of 7.112 m at the ideal storage region. The Fermilab E989 experiment will make use of the storage ring magnet designed and built for the Brookhaven E821 experiment.

The 15 m diameter superconducting coils were transported as one piece in order to avoid disturbing the exceptional magnetic field and required special transportation from BNL to FNAL due to its size. The steel yoke and pole pieces were disassembled and transported by road [42] [12].

The superconducting coils are built from Niobium-titanium (NbTi) and typically operate at 5.0 K while being powered by a 5 V power supply at a nominal current of 5200 A. The magnet had to be designed as a "C"-shape to allow for the detection of the decay electrons which spiral inwards towards the centre of the ring. Two of the coils sit at $R_{inner} = 6677$ mm and the outer coil sits at $R_{outer} = 7512$ mm and run at opposing current directions to create a vertical B-field between them. As shown in figure 4.4, there is a physical gap between the pole pieces and the iron yoke, this 'air gap' decouples the field in the storage region from imperfections in the yoke allowing for an extremely uniform field [42][43].

The final uniformity of the dipole magnetic field achieved at BNL was around ± 50 ppm [12]. To achieve a uniform magnetic field passive and active shims are used. There are over 1000 ferric passive shims which alter the local field as well as many active shims used for fine adjustments to the magnetic field. The active shims work by creating controllable electric currents close to the storage field. For E989 the goal on the azimuthally averaged storage magnetic field was to have deviations from the mean to less than 1 ppm, an explanation of how this is measured is given in section 4.5 as well as figure 4.5 showing the measured current uniformity of the dipole field [43] [44].

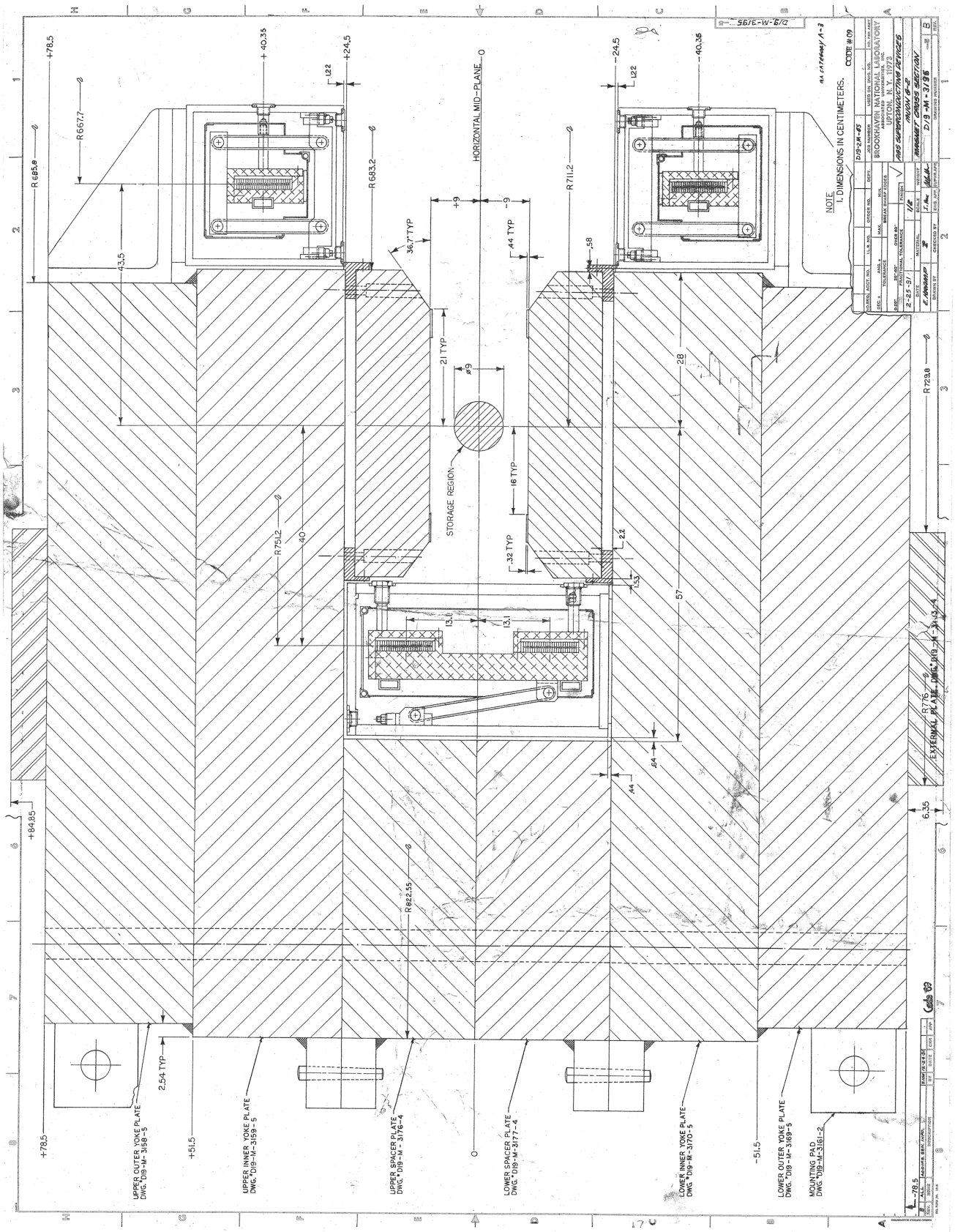

Figure 4.4: Engineering drawing showing a cross section of magnetic storage ring where the four superconducting coils, two pole pieces and storage region are visible.

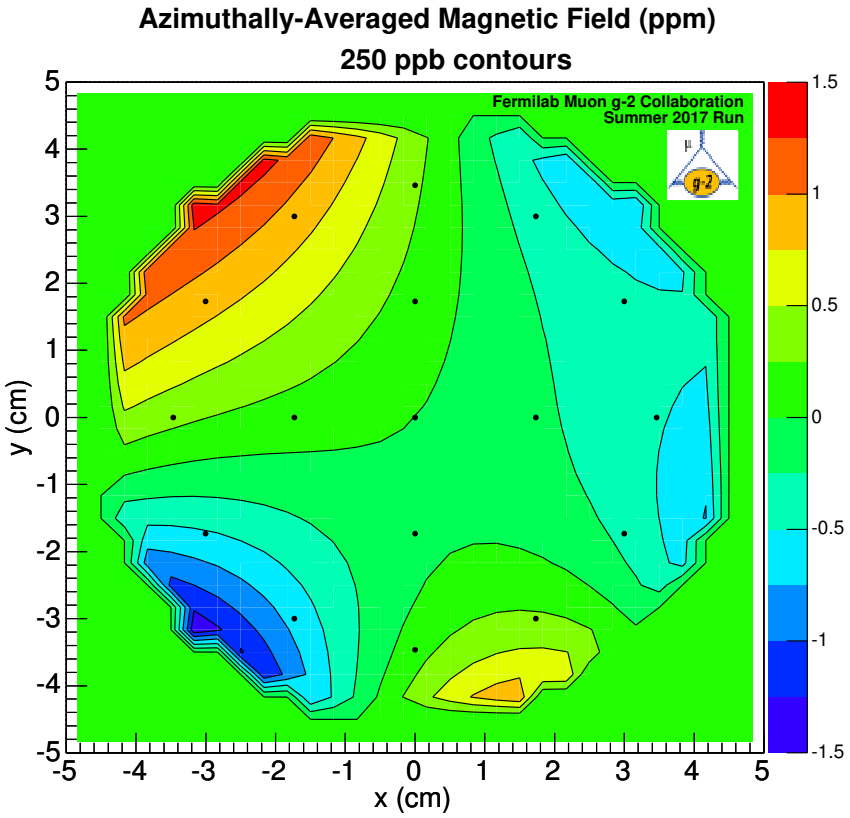

Figure 4.5: An early magnetic field map as measured by the NMR probes located in the trolley, showing overall uniformity but with areas differing from the central value by 1.5 ppm.

4.3 Muon Injection and Storage

To inject muons into the magnetic storage ring they must be transported through the magnet iron where a fringe field exists, without being influenced by this field. To achieve this a 1.7 m long superconducting magnet called the inflector is used which was designed and used throughout E821 and is shown in figure 4.6. This magnet creates a 1.5 T vertical and uniform field which nullifies the main storage ring field, permitting the muons to pass largely undeflected into the storage ring. The inflector is also designed to prevent its own magnetic flux from leaking out and perturbing the nearby main magnetic field. The location of the inflector can be seen in figure 4.11, and a diagram showing the inflector passing through the magnetic storage ring

is shown in figure 4.8. The inflector axis is approximately tangential to the storage ring. When the beam exits the inflector the beam path is a circle displaced by 77 mm radially from the storage region centre, therefore a device is needed to centre the beam correctly. If this device does not give the beam a 'kick' to centre it onto the storage radius then it will propagate around the ring and collide with the vacuum chamber wall close to where it was injected.

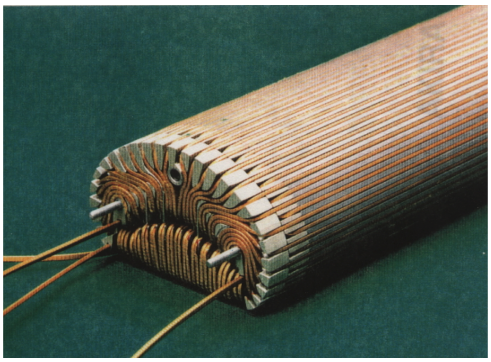

Figure 4.6: Inflector During Construction

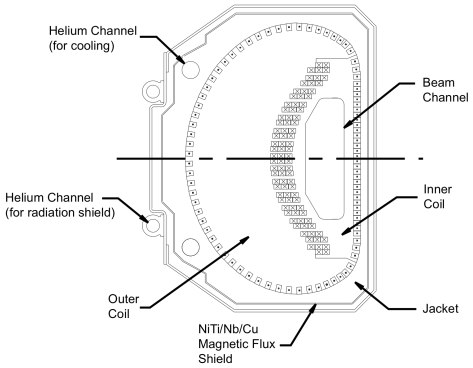

Figure 4.7: Diagram showing a cut through of the inflector.

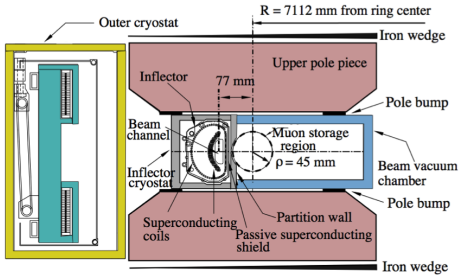

Figure 4.8: Cut through of the magnetic storage ring showing the offset between the inflector beam position and muon storage region.

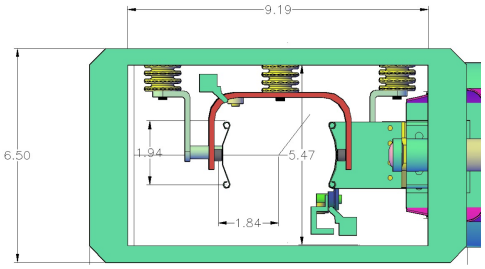

Figure 4.9: Diagram showing a cut through of the kicker plates.

To correct for the fact that the beam is injected off the stored orbit a device called a Fast Kicker or just Kicker creates a strong magnetic field which 'kicks' the beams closed orbit onto the correct path. The muons receive the kick as they cross the central orbit at an angle of 10.8 mrad - 90 degrees around the ring from injection - the kick aims to cancel out this angle leaving the beam with a closed orbit on the storage

region. The design of the E989 kicker can be seen in figure 4.9, and centres the beam by creating a 280 G field between each pair of the three 1.7 m long kicker plates. The current required to achieve this field is around 4.7 kA [42].

Ideally, after the kick the beam is perfectly centred on the storage radius. However, in reality there is a small momentum spread in the μ^+ beam and this results in a spread in orbit radii. Collimators are used to remove μ^+ which sit with momenta near the extremes of the distribution, the period of time where the beam is being collimated is known as scraping. Removing these particles reduces the overall momentum spread of the stored beam to 0.15%. The positions of the collimators in the ring are shown in figure 3.6.

To provide vertical focussing to the stored beam four symmetrically spaced electrostatic quadrupoles are used in the ring. Without this vertical focusing the beam would diverge vertically until the beam leaves the stable orbit. Ideally these focussing quadrupoles would have full coverage around the ring but due to the inflector and the kicker being present gaps are left at 0° and 90°, along with empty gaps at 180° and 270° which provide a four-fold symmetry and importantly gives space for the straw tracking detectors to be installed. Overall the electrostatic quadrupoles cover 43% of the ring's circumference.

4.4 Particle detector systems

There are multiple different detector systems used to detect the muons while they are travelling through the inflector and circulating the storage ring or to detect the decay positrons. These are the injection beam monitors, entrance counters, fiber beam monitors, straw trackers and the calorimeters. Each of these systems which operate in or close to the precise dipole field have been designed to minimise the number of magnetic components in use to avoid perturbing the field.

4.4.1 Calorimeters

There are 24 calorimeters equally spaced around the inside of the ring with the aim of measuring the hit times and energy of the decay positrons. Each calorimeter is constructed from 54 PbF_2 crystals (6 high by 9 wide) with each crystal being 25 mm wide, 25 mm tall and 140 mm deep [45]. Decay positrons create electromagnetic showers as they enter the crystal, these showers generate Cherenkov radiation with the amount of light generated proportional to the initial positron energy. The Cherenkov radiation propagates to the back end of the crystal where it is detected and readout by a Silicon Photo-Multiplier (SiPM). Each crystal is clad in light-tight wrapping to minimise light transmission between crystals which allows for better position reconstruction [14].

PbF_2 has many useful characteristics for use in the calorimeters; it has a high density at 7.77 g/cm^3, short radiation length of 0.93 cm and transmittance range from 250 nm to 1100 nm. As PbF_2 is a Cherenkov radiator and therefore does not produce as much light as a scintillating crystal, high time resolution is possible which greatly reduces pileup. A design requirement of the calorimeter is that it must be able to resolve two showers temporally separated by 5 ns and can use spatial resolution to reduce this further. This requirement limits the effect of unidentified pileup events to a 40 ppb systematic error [46].

One key improvement over E821 is the use of an updated laser calibration system required as the SiPM readout devices are sensitive to bias voltage and temperature stability. Injecting a known signal allows for these changes to be measured and corrected for. Attached to the front face of each calorimeter is a Delrin panel with implantation of NBK-7 right-angle prisms for installation of the laser calibration system. This system can be used in fill, to detect fill to fill variations, as well as out of fill, to detect long term gain drifts over many muon spills with a precision of 0.04% [47]. It is also possible to carry out double pulse studies varying the time between laser pulses which allows the time resolution of each SiPM to be measured [48]. A wiggle plot from an early dataset at E989 is given in figure 4.10.

Calorimeters are the primary detector responsible for the ω_a measurement but the storage ring is also outfitted with auxiliary detectors to measure the beam profile and help reduce systematic uncertainties with the ω_a measurement.

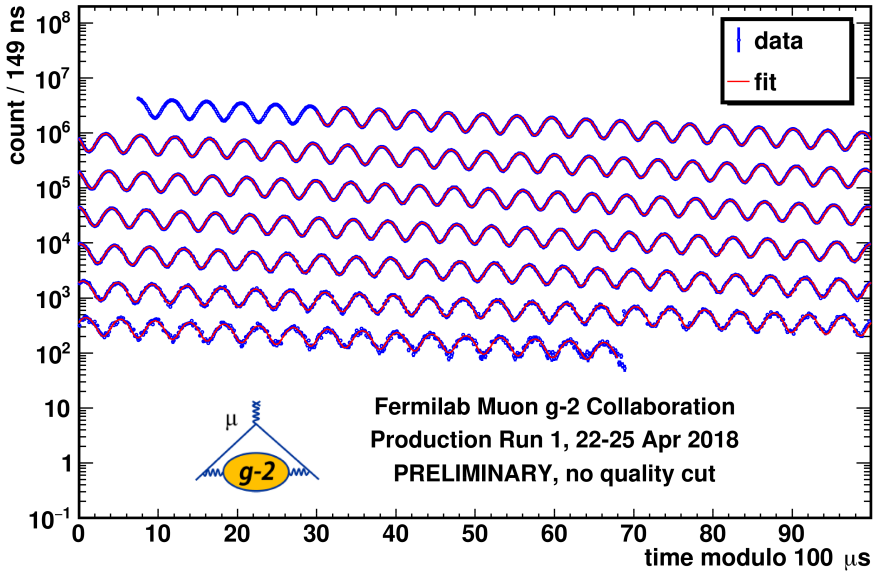

Figure 4.10: Wiggle plot produced from an early physics run at E989. Consists of 60 hours of data which produces approximately 0.95×10^9 positrons when an energy cut of 1.7 GeV is used, resulting in an error of 1.32 ppm, approximately equal to BNL 1999 dataset.

4.4.2 Fiber beam monitors

There are two distinct auxiliary detectors, the retractable fiber beam monitors which make destructive measurements of the beam and the straw tracker detectors which make non-destructive measurements. The fiber beam monitors are used to measure the position (x, y) and angle (x', y') of the muon beam at injection and throughout the muon fill with the aim of observing and directly characterising periodic beam motion such as those described in Chapter 5. Four fiber beam monitors operate in the ring by each holding seven 90 mm long scintillating fibers of 0.5 mm diameter separated by 13 mm in the beam and are present at two locations around the storage ring, two at 180°

and two at 270°. The fiber beam monitors are installed in the vacuum chamber and can be orientated in three ways, out of the beam during normal operation, perpendicular to the beam while operating and parallel to the beam so each fiber sees the same beam for calibration. Shortly after injection the two 180° fiber beam monitors should observe an image of the beam as it was injected at the inflector, while the two 270° fiber beam monitors map x' and y' at the inflector into x and y at 270°. However, this measurement gets distorted at later times due to Coherent Betatron Oscillation (CBO) as well as from scattering due to the fiber beam monitors themselves. These detectors are only used during dedicated beam commissioning runs as they are a destructive beam monitor because they rely on being installed directly into the beam [42] [12] [49].

4.4.3 Straw trackers

Straw Tracker detectors make a non-destructive measurement of the beam profile throughout the duration of each muon fill. This is possible as in certain places around the storage ring when a decay positron spirals towards the centre of the ring it travels through a section of the vacuum chamber which is fitted with straw tracker modules, passing through multiple straws on the way to the calorimeter. These hit straws can be used to reconstruct the trajectory of the positron as it passed through the tracking station which can then be extrapolated back to the decay point to build up a beam profile of the stored muons. The recorded trajectories can also be extrapolated forwards to help calibrate the calorimeter, further helping to reduce the systematic uncertainties within the ω_a measurement. The use of in-vacuum straw trackers in E989 provides a large upgrade over for E821, the straw tracking detectors and their uses will be expanded on in more detail in Chapter 5.

4.4.4 Inflector beam monitoring system

One improvement over E821 is the use of an Inflector Beam Monitoring System (IBMS) which consists of three scintillating fiber detectors that measure the beam profile

at three locations: immediately downstream of the magnet yoke hole, immediately upstream of the inflector and immediately downstream of the inflector - shown in figure 4.11. These detectors continuously monitor the muon beam as it passes from the final focus into the storage ring and operate as the primary diagnostic tool to verify the beam optics tune in the muon injection section as well as continuously monitoring the beam properties, relevant for detecting systematic problems [42].

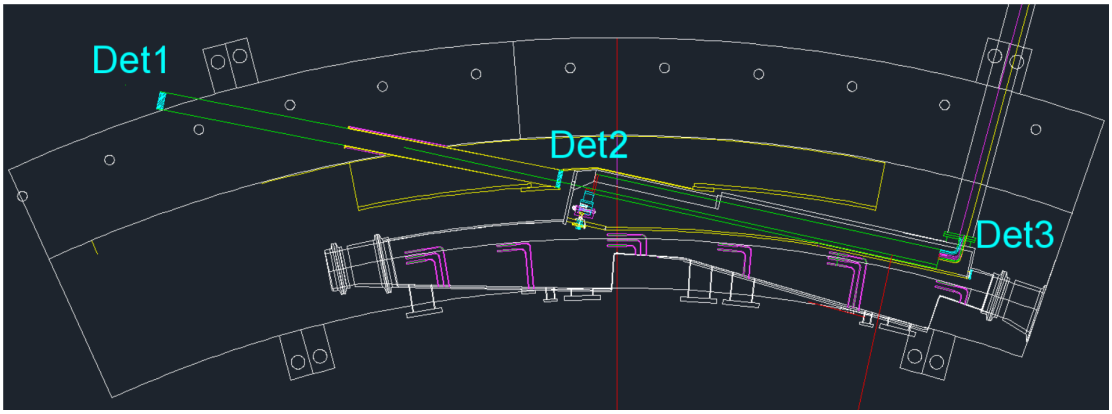

Figure 4.11: IBMS detector locations. Detector 1 at the entrance to the yoke hole, detector 2 at the entrance of the inflector and detector 3 inside the ring vacuum at the injection point to the ring.

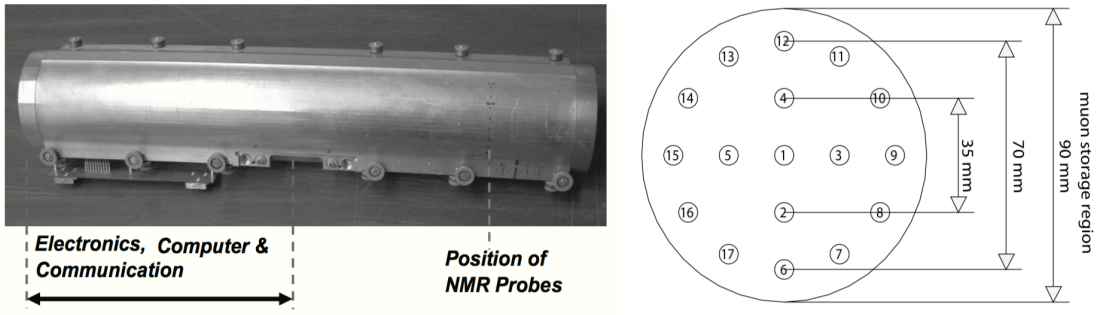

Figure 4.12: *Left:* Photograph of the trolley which holds 17 NMR probes used to measure the magnetic field in the storage region of the vacuum chambers. *Right:* The layout of the 17 NMR probes located inside the trolley.

4.4.5 Entrance counter

An entrance counter (T0) scintillator immediately outside of the storage ring prior to IBMS-1 provides a time and intensity profile of the incoming muon bunch. This is used to precisely align data from multiple fills which reduces smearing of the ω_a signal.

4.5 Field measuring equipment

As mentioned in section 3.0.1, E989 relies on precise measurements of two quantities, ω_a and $\widetilde{\omega}_p$. A number of systems have been developed to make the $\widetilde{\omega}_p$ measurement using pulsed proton NMR (pNMR) with a series of water and petroleum jelly probes. An absolute field measurement is made using a spherical reference probe - this is the same probe used in the muonium hyperfine experiment which determined the muon-to-proton magnetic moment ratio. This reference probe is cross calibrated with a Plunging Probe which can be extended into the storage region allowing for cross calibration with the trolley probes. Additionally, a Fixed Probe system - composed of 378 pNMR probes - is permanently mounted to grooves on the top and bottom of the vacuum chambers which read out continuously and provide a measure of the magnetic field stability over time. A number of the Fixed Probes are also used in a feedback loop with the main storage ring power supply which keeps the field stable over time [42].

The in-vacuum NMR trolley is able to measure the magnetic field within the storage region by supporting 17 pNMR probes on its front face arranged in concentric circles as shown in figure 4.12. The trolley can take measurements of the magnetic field around the full circumference of the storage ring which gives the multipole composition of the field averaged over the ring azimuth. During data taking periods the trolley will be moved into the storage ring and pulled through the entire storage volume, a process which takes 2 hours, during this time the field is sampled at 6000 locations in azimuth by each of the 17 probes. The trolley also carries a precise bar code reader which provides the position of each reading.

4.6 Overview of computing

The computing effort of E989 can be roughly divided into two parts: online computing and offline computing. Here online computing needed to record ω_a data will be outlined, offline computing necessary for straw tracker reconstruction will be explained in section 6.2.

The data acquisition system for E989 is required to read, process, monitor and store all of the data produced by the many detector systems at an average rate of 12 Hz. The spill structure comprises of four consecutive 700 μs spills with 11 ms spill to spill separation. The raw data rate from the 24 calorimeters while operating at a 12 Hz spill rate is 18 GB/s, this is processed using Nvidia K40 GPUs (1 per calorimeter) at a rate of around 80 MB/s which is saved to disk. The data coming out of each calorimeter consists of photodetector (SiPM) signals from all 54 channels, these are digitised continuously at 800 MHz for 700μs after receiving an accelerator trigger. For the straw tracker detectors the full system consists of 3072 channels and has a data rate of approximately 3 MB/s, this rate is much lower than the calorimeters as only the channel number and hit times are saved rather than digitised waveforms. The data rate from auxiliary detector systems total less than 20 MB/s [42][50].

The data coming from all of these systems is initially stored on a local RAID array before being transferred to onsite tape storage (dCache) area using Fermilab's Transfer Service (FTS). The data flow for ω_a processing can be seen in figure 4.13.

The MIDAS package is used to control the data acquisition system as well as performing many other tasks, such as handling the read out from frontend electronics, event building, data logging DAQ operations, storing experimental configurations in an online database and displaying alarms on a local or remote viewable web interface.

A custom built data quality monitoring tool was also built for E989, this is capable of unpacking data to the art (event-processing framework used by E989) format in real time to allow low level data processing and reconstruction prior to being published to a web page for visualisation. This will be described in more detail in section 6.5.

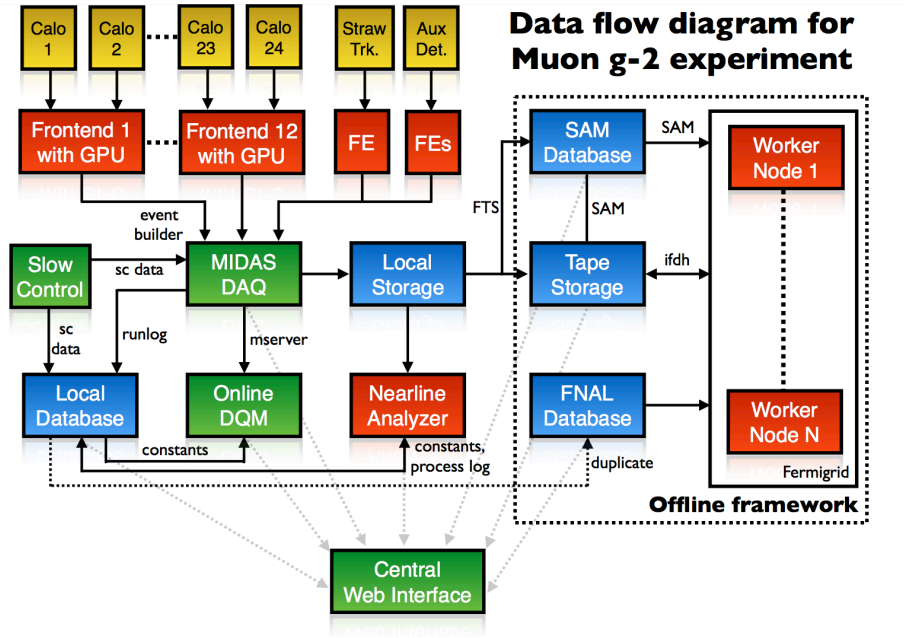

Figure 4.13: Data flow for ω_a data processing [50]

.

Chapter 5

Straw Tracking Detectors

The role of the trackers is to precisely measure the momentum of the decay positrons and reconstruct the trajectory as the positron travels from the storage region to the calorimeter. This trajectory can either be extrapolated backwards to the muon decay point to build up a picture of the muon beam profile as a function of time, or forwards into the calorimeter to make a comparison between the two detectors. The ability of the straw trackers to probe many different aspects of the muon beam allows them to be the 'Swiss Army Knife' of the experiment giving key measurements for many different analyses although optimised for radial beam measurements. The straw trackers are also the only detector present in the experiment able to precisely measure a tilt in the muon precession plane from vertical, which would indicate a non-zero muon EDM.

There are three straw tracker stations positioned at 15°, 180° and 270° around the ring - where the injection point is at 0°. Each tracker station contains 8 identical straw tracker modules which are installed in the scalloped area directly in front of the calorimeter, as shown in figure 5.1. These three locations were chosen to maximise the azimuthal coverage around the ring while avoiding conflicts with other ring mounted systems.

This chapter will cover the physics goals, requirements, design and operational principles of the straw tracking detectors as well as giving an overview of the electronics

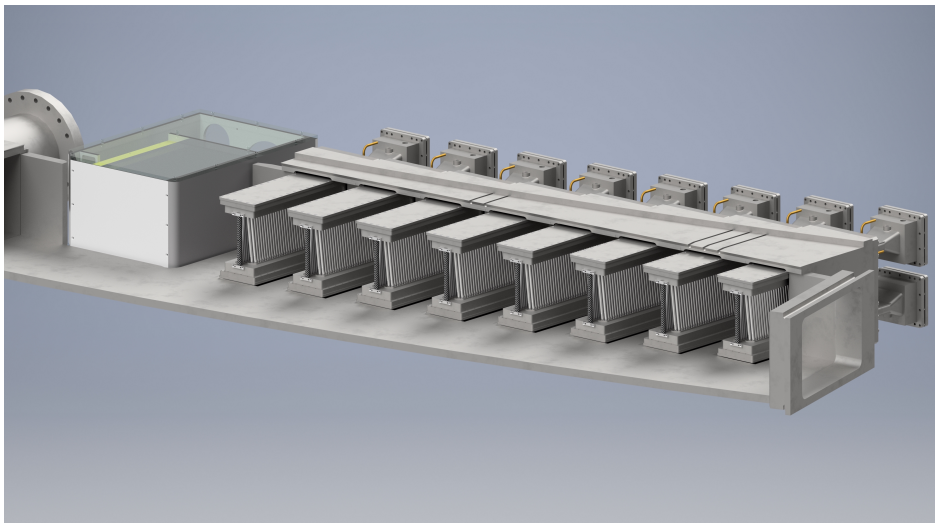

Figure 5.1: Cut away render of a straw tracker station looking from the outside of the ring inwards showing the locations of the straw tracker modules in front of a calorimeter.

and other services required to operate them. Chapter 6 will present the construction of the straw tracking detectors.

5.1 Physics goals

As previously mentioned the straw trackers have many wide ranging purposes, these will be outlined here with the improvement in experimental uncertainties related to the measurement of ω_a noted. Primarily the goal of the tracking detectors is to measure the muon beam profile as a function of time through each fill, this information is then used to determine several beam dynamics parameters. The straw trackers can also be used to help reduce the uncertainties present within the operation of the calorimeters as well as validating reductions in the uncertainties provided by the updated calorimeters. These two areas are presented below and summarised in table 5.1.

5.1.1 Beam related physics goals

Beam oscillation

Coherent Betatron Oscillation (CBO) occurs when the stored beam oscillates around the closed orbit in the radial direction due to a combination of the defocusing electric field and the central magnetic field providing a linear restoring force radially. This causes the acceptance of the calorimeters to change, manifesting itself in the data as an amplitude modulation in the decay e^+ time spectrum introducing an associated systematic error. The CBO can be measured using the straw tracking stations which give vital information to the associated analyses. The width of the CBO is also important for the fast rotation analysis, presented below. Also measured by the straw trackers is the vertical betatron oscillation, which is due to the quadrupole electric field providing a linear restoring force vertically. Initial measurements of these effects are presented in section 6.4

Fast rotation

The inflector used in E989 allows a momentum distribution of $\pm 0.15\%$ to enter the ring, as the muon beam circulates muons at a lower radius (lower momentum) eventually overtake those at a larger radius (higher momentum) and carry on to do so many times after multiple orbits around the ring. This is initially visible in the data as a broadening of the bunch structure seen by individual calorimeters until the beam fills the ring uniformly. This shows that a fraction of muons do not have the magic momentum required, therefore the electric field term can not be completely eliminated. This introduces a systematic error in the measurement of ω_a. Evolution of the muon distribution measured by the straw trackers throughout the fill will be valuable to the fast rotation analyses and will help to reduce the systematic uncertainty.

Muon spatial distribution

The effective magnetic field seen by the muons alters the precession frequency. As shown in section 3.0.1, this is accounted for recording the trajectory of tracks passing through the tracker station and using this information to extrapolate the track back to the muon decay point thus building up a map of the muon spatial distribution. An initial measurement of the muon spatial distribution is given in section 6.4. This measurement can then be convoluted with the measurement of the magnetic field map within the storage region required for the a_μ measurement. Also, the straw trackers are able to make a measurement of the muon spatial distribution every fill, while other methods are destructive so are infrequently used. The trackers can therefore precisely ensure that the beam injection remains constant from fill to fill and that the final dataset used is comprised of well behaved fills.

Muon losses

Muons at the edge of the storage region are more likely to be lost at early times, leading to a deviation from pure exponential muon decay in equation 3.7 which can affect the fits. These muons that leave the storage region are called Lost Muons. The average spin of the lost muons can differ from that of the fully stored muons, and this difference in average spin phase can cause a shift in the measured ω_a [51]. E989 aims to reduce the muon losses by more than an order of magnitude compared to E821. This requires precise knowledge of the muon population phase-space after scraping, which the straw trackers can measure each fill. In E989 lost muon rates will be measured in the same way as in E821, using triple calorimeter co-incidences. However in E989 this analysis can be cross checked with information gained from the straw tracking stations which will be vitally important.

Pitch correction

The vertical angle in the precession plane caused by any radial field means that the direction of the muon spin and the B-field are not exactly aligned, reducing the rate

of precession. The pitch correction accounts for this in terms of the vertical betatron oscillations where the muons have some vertical component to their momentum. This vertical oscillations causes the 'pitch' angle, ψ, between the muons momentum and the horizontal plane to vary with a certain frequency,

$$\psi = \psi_0 cos(\omega_y t), \tag{5.1}$$

where the vertical betatron frequency is given by ω_y. Using this with equation 3.5 for ω_a gives,

$$\omega_a^{'} \approxeq -\frac{Qe}{m} a_\mu B_y \Big(1 - \frac{\psi^2}{2}\Big) = -\frac{Qe}{m} a_\mu B_y \Big(1 - \frac{\psi_0^2 cos^2 \omega_y t}{2}\Big). \tag{5.2}$$

The time average gives the pitch correction, C_p, required,

$$C_p = -\frac{\langle \psi^2 \rangle}{2} = -\frac{\langle \psi_0^2 \rangle}{4} = \frac{n}{4} \frac{\langle y^2 \rangle}{R_0^2}. \tag{5.3}$$

Where n is the electrostatic quadrupole field index and R_0 is the magic radius. The value for $\langle y^2 \rangle$ can be measured by the calorimeters however the straw trackers are able to measure this value precisely as well as measuring the vertical positron decay angle which is vital to the pitch correction analysis. The vertical pitch motion acts to lower the observed frequency so the observed frequency must be increased by this correction. The pitch correction applied at BNL for the 2001 data taking period was 0.270 ± 0.036 ppm [42].

This up-down asymmetry is in phase with the ω_a oscillation. However, as described in section 5.1.3, if an muon electric dipole moment were to be present this would be 90 degrees out of phase with the ω_a oscillation.

5.1.2 Detector relations physics goals

Calorimeter pileup correction

Due to timing and segmentation limitations with the calorimeter detectors it is possible for two positrons to arrive at same position within a short time window and get counted

as a single hit. If this occurs with two low energy positrons it is possible that they get resolved into one high energy event. The probability of this happening depends on the incoming rate therefore becomes more of an effect at early times rather than late times, called an early to late effect. As pileup is rate dependent then it also oscillates at the ω_a frequency. Using the information from the straw trackers it is possible to isolate time windows in which more than one positron hits the calorimeter to verify the calorimeter based pileup correction. This will be looked at in more detail in Chapter 7.

Calorimeter gain stability

As mentioned in section 4.4, the calorimeter uses SiPM to read out the signals deposited in the crystals. The SiPM readout system is particularly sensitive to small changes in bias voltage and temperature. It is known that short and long timescale gain fluctuations introduce a systematic uncertainty. The laser calibration subsystem provides the means to monitor the detector gain stability while single track events from the straw trackers can be used to determine the absolute energy calibration.

5.1.3 Measuring the muon precession plane

The straw tracking detectors are able to precisely measure the vertical positron decay angle, any up-down asymmetry in this angle would indicate a tilt in the muon precession plane from vertical. This can either be explained by a component of the storage ring magnetic field or a permanent electric dipole moment (EDM) of the muon. The current best measurement of the muon EDM was made by the E821 muon g-2 experiment and this will be significantly improved at E989 with the use of the straw trackers.

Uncertainty	E821 Value	E989 goal	Role of tracking
Magnetic field seen by muons	0.03 ppm	0.01 ppm	Measure beam profile on a fill by fill basis ensuring proper muon beam alignment
Beam dynamics corrections	0.05 ppm	0.03 ppm	Measure beam oscillation parameters as a function of time in the fill
Pileup Correction	0.08 ppm	0.04 ppm	Isolate time windows with more than one positron hitting the calorimeter to verify calorimeter based pileup correction
Calorimeter gain stability	0.012 ppm	0.02 ppm	Measure positron momentum with better resolution than the calorimeter to verify calorimeter based gain measurement
Precession plane tilt	4.4 uRad	0.4 uRad	Measure up-down asymmetry in positron decay angle

Table 5.1: Beam dynamic related uncertainty goals for the E989 Muon g-2 experiment and how the straw trackers can be used to meet these goals.

5.2 Requirements and design

The role of the tracking detectors is to measure the trajectory of a charged particle through the tracking region with enough precision to allow a track to be reconstructed, this makes it possible to extrapolate the track formed backwards to the muon decay point or forwards to the calorimeter. To achieve this the straw tracking detectors were designed to make as many measurements of the e^+ three-dimensional position as possible, with the measurement planes being as close together as possible to maximise acceptance for low momentum positrons as well as measurements being made over a large distance to enable the curvature of the track to be measured for accurate momentum reconstruction. This results in the detectors being installed in all of the useable space between two calorimeters while extending towards the storage region as much as possible without impinging on the space the NMR trolley requires to circulate the ring. The trackers are installed in the vacuum chambers in-between two calorimeters and are designed to produce as little multiple scattering as possible. The

location of the straw trackers in relation to the calorimeter as shown in figure 5.1, where the calorimeter is shown on the left of the figure and figure 5.3 shows a tracker module with key components highlighted.

In each straw tracker station there are 8 identical modules placed close together, the layout of the tracking station is shown in figure 5.4. Each of the straw tracking detectors, known as modules, consist of 128 aluminised Mylar tubes (referred to as straws) arranged into four layers with two of the layers angled at $+7.5°$ from vertical and the other two angled at $-7.5°$, this stereo angle allows for the vertical height of the track to be measured. Each of the pair of layers orientated at the same angle are known as a view, the two views are named the U-view and the V-view. The straws are secured at the top and bottom in aluminium manifolds which house the front-end electronics and supply gas to the straws - this design can be seen in figure 5.2.

At the centre of the straw is a 25 μm gold plated tungsten wire which is held at high voltage, the strong electric field generated ensures the ionisation created as a particle travels through the gas drift towards the wire and deposits a charge. The straw trackers are designed and built to use low mass materials to ensure the decay positrons are not perturbed through the tracking region as well as minimising magnetic components to prevent distorting the magnetic field.

The straw wall is made of two layers of 6 μm Mylar, wound in a spiral with a 3 μm layer of adhesive between the two layers. The total thickness of the straw wall is 15 μm. The inner surface has 500 Å of aluminium overlaid with 200 Å of gold as the cathode layer, while the outer surface has 500 Å of aluminium deposited to act as additional electrostatic shielding and reduces the leak rate of ionising gas into the vacuum. A cut through render of a straw with aluminium end caps, plastic inserts and the 25μm gold plated tungsten wire is shown in figure 5.2 and table 5.2 shows the material budget in the path of a positron through a single straw.

As the straw trackers operate within the storage ring vacuum many design considerations had to be made. These include the use of materials and glues which have low outgassing rates as well as considering the deformation and stresses that occur

from changing pressure environments. For example simulations were carried out of the modules in a vacuum and showed that without a carbon fibre post the manifolds deform inwards by 55 microns (a 110 micron reduction in space between the manifolds) which reduces the tension in both the straws and sense wires by an unacceptable amount. So the use of a physical restraint was required. With a carbon fibre post the maximum deformation is 22 microns per manifold (maximum reduction of a 44 microns in space between manifolds) [52]. As mentioned in section 6.0.1 there is a strict requirement that the leak rate of each module is less than 4.5×10^{-5} Tl/s, this value was reached with aid of vacuum pumping simulations and gives a vacuum level suitable for all systems within the storage ring vacuum (SRV) within an acceptable pump down time. As the permeation rate through mylar is different for different gases the total leak rate for a module has to be tested with multiple gas mixtures that may be used.

There are many different components used within the manifolds to either read out the signal deposited on the sense wire, provide high voltage to the sense wires or to support the wire restraining pins while allowing gas to flow through the straws. All of the materials used were chosen to ensure compatibility with a range of gases. Some materials were found to either absorb or react with the active gas which over time could degrade the material to failure or pollute the active gas which can be harmful for the long term operation of the detector. These materials were ruled out by either studying material property and compatibility sheets, reading previous experiment's experiences or carrying out long term tests where a material sample is monitored while immersed in different gases.

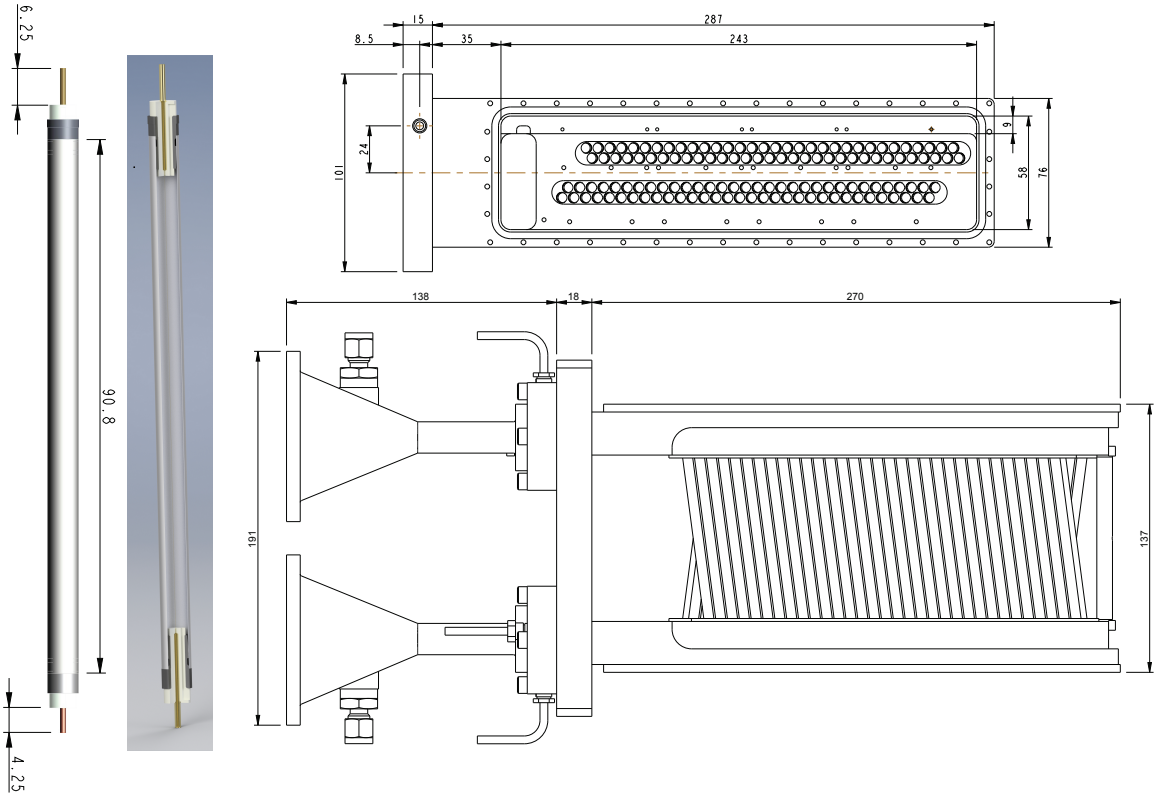

Figure 5.2: *Left:* Engineering drawing showing a built straw with a cut through render of a built straw for comparison. *Right:* Engineering wireframe drawings showing a manifold as well as a fully constructed straw tracker module.

Table 5.2: Thicknesses and radiation lengths of materials in the active area of the detectors.

Material	Thickness	Radiation Length (cm)	X/X0 (%)
Gold	200 Å	0.3	6×10^{-4}
Aluminum	500 + 500 Å	8.9	1×10^{-4}
Adhesive	3 μm	17.9	2×10^{-3}
Mylar	6 + 6 μm	38.4	3×10^{-3}
Argon Ethane	5 mm	1×10^{5}	4×10^{-2}

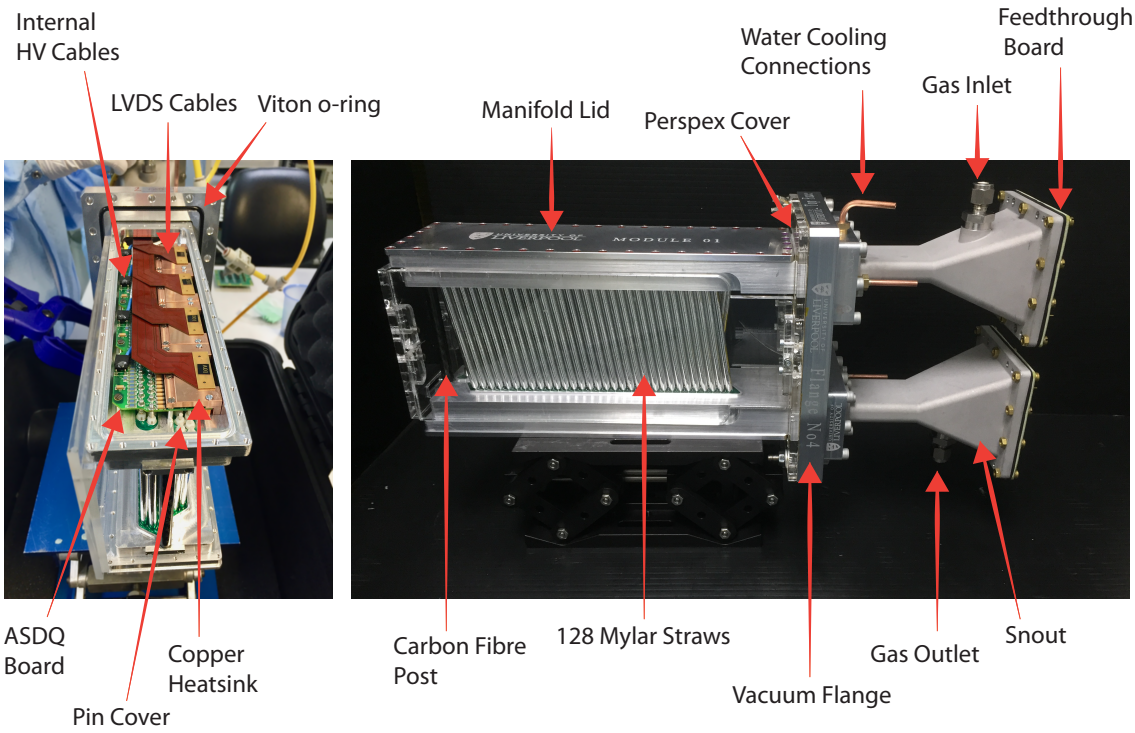

Figure 5.3: *Left:* Constructed tracker module prior to lid being fitted showing the in-manifold electronics with key components highlighted. *Right:* Fully constructed tracker module with protective plastic shield again with key components highlighted.

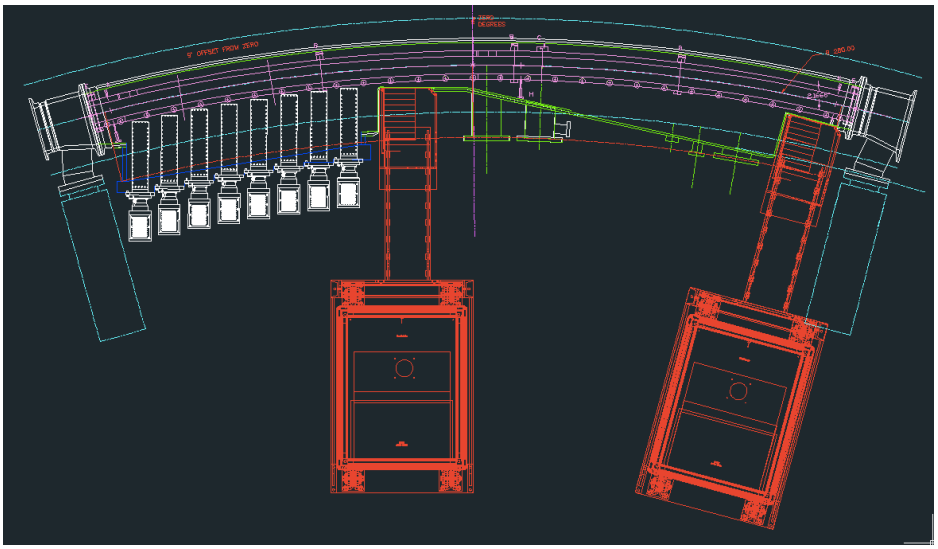

Figure 5.4: Placement of the straw tracking modules in the scallop region of the vacuum chamber.

5.3 Operating principles

Each straw within a straw tracking detector acts as an individual drift chamber and when fast charged particles travel through the straw interactions with gas atoms occur, the strongest and most probable interaction being an incoherent interaction between the electromagnetic field of the passing particle and the gas atoms, resulting in both excitation and ionisation. There are many factors which need to be considered when deciding on operating gas mixtures such as the number of primary electrons generated, electron drift velocity, stability of the avalanche as well as long term stability of the detector. Important properties of commonly used gases are given in Table 5.3. Noble gases are typically used as ionisation is the dominant form of energy loss in the energy range of interest. For use in the straw trackers a gas mixture of 50:50 Argon and Ethane was chosen.

The interactions between the impinging particle and gas atoms are purely random and can be characterised by a mean free path between ionising encounters, λ,

$$\lambda = \frac{1}{N\sigma_I}, \tag{5.4}$$

where σ_I is the ionisation cross-section per electron and N is the density of electrons. So the mean number of encounters along a length, L, is given by $\frac{L}{\lambda}$, this property has been measured for many gases. For reference, the number of primary ionising collisions per centimetre of track length through Argon has been measured to be 27.8 ± 0.3 where the fast ionising particle has a relativistic velocity factor, γ, of 4.0 [53] [54].

Another important property for gases used in ionisation chambers is the average energy required for the creation of one free ion electron pair, W_i,

$$W_i \langle N_I \rangle = L \left\langle \frac{dE}{dx} \right\rangle, \tag{5.5}$$

where $\langle N_I \rangle$ is the average number of ionisation electrons created along a path of length L, and $\langle \frac{dE}{dx} \rangle$ is the average total energy loss per unit path length of the fast particle.

The energy W_i spent on average for creating one ionisation electron in Argon is 26 eV, this property of other gases is listen in table 5.3 [54]. However, most of the charge

Table 5.3: Table showing the relevant important properties of different gases used in gaseous detectors. Where I_0 is the ionisation potential and W_i is the energy loss required to produce an electron ion pair.

Gas	ρ (g/cm^3)	I_0 (eV)	W_i (eV)	$\frac{dE}{dx}$ (MeVg^{-1}cm^2)
H_2	8.38×10^{-5}	15.4	37	4.03
He	1.66×10^{-4}	24.6	41	1.94
N_2	1.17×10^{-3}	15.5	35	1.68
Ne	8.39×10^{-4}	21.6	36	1.68
Ar	1.66×10^{-3}	15.8	26	1.47
Kr	3.49×10^{-3}	14.0	24	1.32
Xe	5.49×10^{-3}	12.1	22	1.23
CO_2	1.86×10^{-3}	13.7	33	1.62
CH_4	6.70×10^{-4}	13.1	28	2.21
C_4H_{10}	2.42×10^{-3}	10.8	23	1.86

produced along a track occurs from secondary ionisation processes where electrons are liberated from atoms which do not encounter the initial fast ionising particle. This secondary ionisation process either occurs through collisions of ionisation electrons with other atoms,

$$e^- A \rightarrow e^- A^+ e^-, \tag{5.6}$$

or via a process involving an intermediate excited state, A^*, which collide with a second species of atoms or molecules, B, present in the gas. This is known as the Penning effect and this process is shown in equation 5.7. Here A is Argon and A^* is the metastable state of Argon while B is a molecular additives (quencher), required for the stability of proportional wire operation.

$$\begin{aligned} e^- A &\rightarrow e^- A^* \\ A^* B &\rightarrow A B^+ e^-. \end{aligned} \tag{5.7}$$

As shown in in figure 5.2, each straw has a sense wire at the centre held at a high voltage acting as an anode while the straw wall is grounded to the aluminium manifold

acting as a cathode, this creates a strong electric field inside the straw radially outwards from the wire. When the liberated electrons are in the presence of this electric field they travel along the field lines towards the sense wire colliding with gas molecules producing ionisation along its path. This net motion of the electrons in the gas is known as drift and the velocity at which this happens is known as drift velocity, typically of the order 50 $\mu m/ns$. The vertical magnetic field present introduces an orthogonal force on the drifting charges giving the electrons a curved trajectory which can be seen in figure 5.5. The angle of curvature is known as the Lorentz angle and differs for different gases.

As the electrons reach the strong electric field surrounding the anode sense wire avalanche multiplication occurs, boosting the deposited signal amplitude by several orders of magnitude. This avalanche multiplication only occurs very close to the anode wire - typically at a few wire radii - as shown in figure 5.6. This effect allows for very small initial ionisation of only a few electrons to be detected, where the gain, G, can be defined by [55],

$$G = Q_{final}/Q_{initial\ ionisations}. \tag{5.8}$$

At high field strength collisions of electrons with atoms or molecules can also cause excitation, with the following de-excitation occurring via photon emission. These photons can escape the avalanche region and produce electrons via the photoelectric effect in the gas or at the straw wall which can undergo its own avalanche chain. This is where the gas can break down and the detector enters the Geiger-Müller mode of operation [55]. To combat this an additive or quencher gas is added, this is typically an organic molecule such as Ethane which has many degrees of freedom and so has a large photo-absorption coefficient [55]. Care was taken during construction to build and store the detectors in a clean environment as well as using gases of high purity during operation, as even small impurities of electro-negative gases can deteriorate the performance of the detector through electron attachment.

The signal measured on the wire from a single ionisation consists of two pulses, a short pulse from the avalanche electrons inducing charge on the close by wire, then a long tail, typically several hundred nanoseconds in duration, coming from the ions

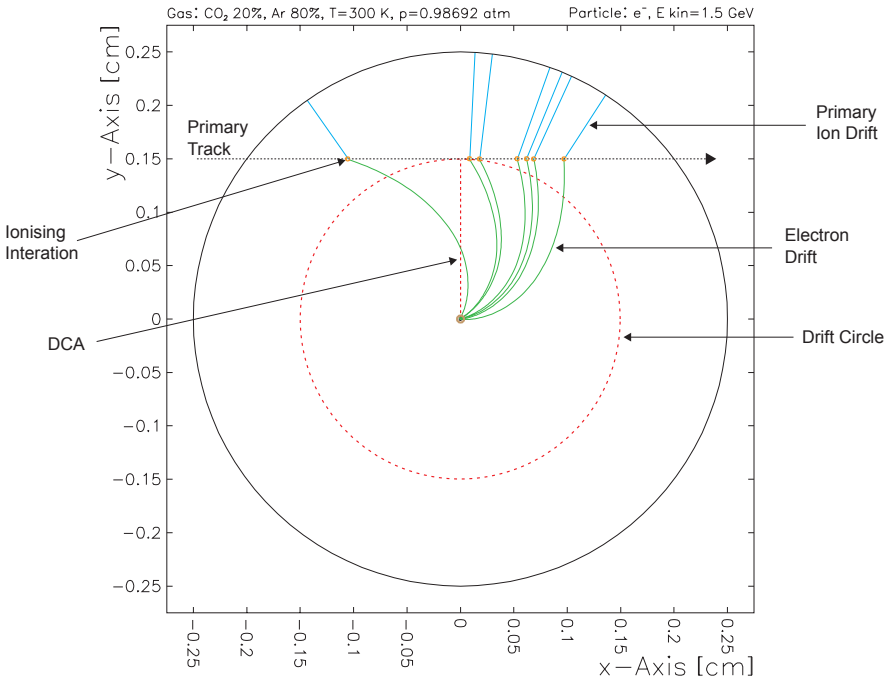

Figure 5.5: Garfield simulation of an ionising particle travelling through a gas filled straw with a high voltage wire held at the centre with key aspects highlighted.

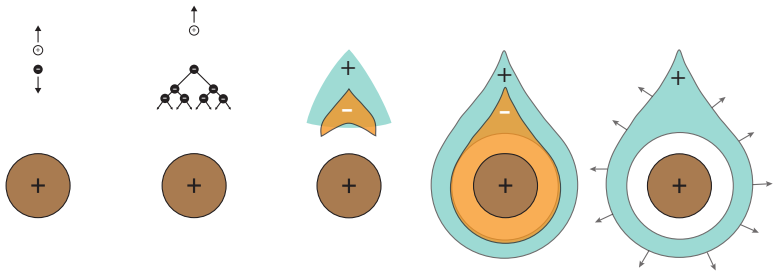

Figure 5.6: Time development of an avalanche in a proportional counter. A single primary electron proceeds towards the anode, in regions of increasingly high fields, experiencing ionising collisions; due to the lateral diffusion, a drop-like avalanche, surrounding the wire, develops. Electrons are collected in a very short time (1 ns or so) and a cloud of positive ions are left, slowly migrating towards the cathode [55].

diffusing to the cathode. Due to the large ion mass the drift to the cathode happens at a velocity much slower than the electron drift velocity, this is known as the ion tail. The ion tail is suppressed within the front-end electronics to avoid masking subsequent charged particle signals.

The signal recorded by the electronics indicates the time a signal was deposited on the wire but this alone would not allow for a precise reconstructed track. The measured hit time, t_h is composed of the time at which the particle entered the straw, t_0, as well the time it takes for the ionisation to drift to the wire, t_d. So, if the t_0 is known then the t_d can be calculated and with knowledge of the electron drift velocity in the gas the radius from the wire at which the particle travelled through can be measured. This is called the Distance of Closest Approach (DCA), shown in figure 5.5 and is explained in more detail in section 6.2. This DCA measurement for a single straw will result in no knowledge of the particle's direction of travel and just gives a cylinder around the wire. To gain a full 3D reconstruction of the particles trajectory, the DCA from multiple straws at different orientations need to be combined. Track formation will be explained in section 6.2.

For a gaseous ionisation detector, such as this one, there are multiple different operating modes that have different characteristics, these are known as Ion Chamber Counter, Proportional Counter and Geiger-Müller regions. The straw trackers will operate in the proportional counter mode where the electric field around the sense wire is large enough to produce an ionisation avalanche for every primary electron, so the number of particles liberated by secondary interactions is proportional to the number of ions produced by the passing ionising particle, as explained previously. With a lower sense wire voltage there is no avalanche produced which results in a collection of only the charges produced in the initial ionisation event, known as Ion Chamber Counter. When the voltage applied to the sense wire is higher than proportional counter it enters the Geiger-Müller region, where the avalanche is much larger and continues until the counter is saturated with ions. Here the size of the current pulse is independent of the size of the ionisation event that produced it.

5.3.1 Garfield simulations

Using the gaseous detector simulation package Garfield [56] it is possible to model ionising particles travelling through a gas filled straw, producing primary and secondary ionisations as well as the drifting of charged particles and avalanche close to the wire. Using Garfield it is possible to simulate the behaviour of gas mixtures at different temperatures, pressures and impurity levels as well as simulating the behaviour at different applied electric and magnetic fields.

A labelled event simulated in Garfield can be seen in figure 5.5. It is also possible for Garfield to give the signal induced on the sense wire which can be used as input to a simulated electronics model. An example of this is given in figure 5.9.

5.4 Readout electronics

The electronics required to readout each straw tracker module can be split into two groups, the front-end electronics - which detect and process signals from the sense wires, and the back-end electronics - which interface with the front-end electronics and manage the data, power, clock and control signals. The front-end electronics include the ASDQ (**A**mplifier **S**haper **D**iscriminator with charge (**Q**)) board housed inside the straw tracker manifolds, as well as the TDC (**T**ime to **D**igital **C**onverter) boards located inside the FLOBBER (**F**rontend **L**ow voltage **O**ptical **B**ox to **B**ack**E**nd **R**eadout) which provides RF shielding. While the back-end electronics consists of the logic board located in the FLOBBER, the FC7 and AMC13 are located in the centre of the ring as well as the back-end computer located in the counting house. All of the tracker modules internal electronics as well as the FLOBBER mounted electronics were designed to be free of magnetic components to avoid perturbing the precise magnetic field within the storage ring. A high level overview of the straw tracker electronics layout can be seen in figure 5.7 with the readout for one view of a tracker module being given in 5.8.

The low voltage power supply for the front-end boards comes from a low voltage crate housed in a rack in the centre of the ring, this low voltage crate also manages the slow control communication between the straw tracker modules and the slow control computer located in the same rack. This rack also houses the High Voltage (CAEN SY127) crate used during tracker operation, this will be expanded on in more detail in section 5.4.5.

5.4.1 Front-end electronics

The charge deposited on a wire from the impinging ionising particle first reaches the ASDQ board which contains two ASDQ ASIC (application-specific integrated circuit) chips. This signal goes through many steps of signal processing on this chip. These are amplification, shaping, baseline restoration and discrimination. During shaping the many peaked structure in the signal coming from multiple primary ionisations drifting to the wire is made into a single smooth peak before baseline restoration is used to remove the long tail arising from the slow ion drift signal. A discriminator then detects if and when this pulse crosses a programmable threshold, when it first crosses the threshold the leading edge is set and when it goes below the threshold the trailing edge is set. These are outputted as digital signals which are high for the duration between the leading edge and the trailing edge. An example of a signal from a sense wire passing through these signal processing stages is given in figure 5.9.

The digital signal from each of the ASDQ boards housed in the straw tracker manifold travel along Low Voltage Digital Signal (LVDS) cables to the TDC boards housed in the FLOBBER. This LVDS cable also supplies low voltage power and reference voltages to the ASDQ board. The TDC board is able to time stamp the transitions in the ASDQ output with a 625 ps precision, using a 40 MHz experiment-wide external clock. This data is buffered during a μ^+ fill of the storage ring into a data-block before being read out to the backend electronics. Each straw tracker module requires eight ASDQ boards, four TDC boards (each with two TDC chips), two logic

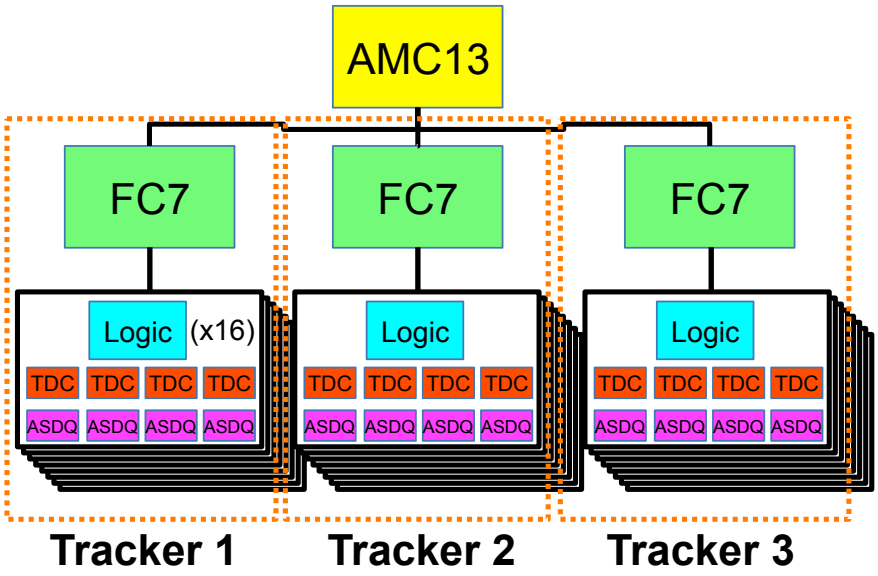

Figure 5.7: Block diagram giving an overview of the readout for the three trackers.

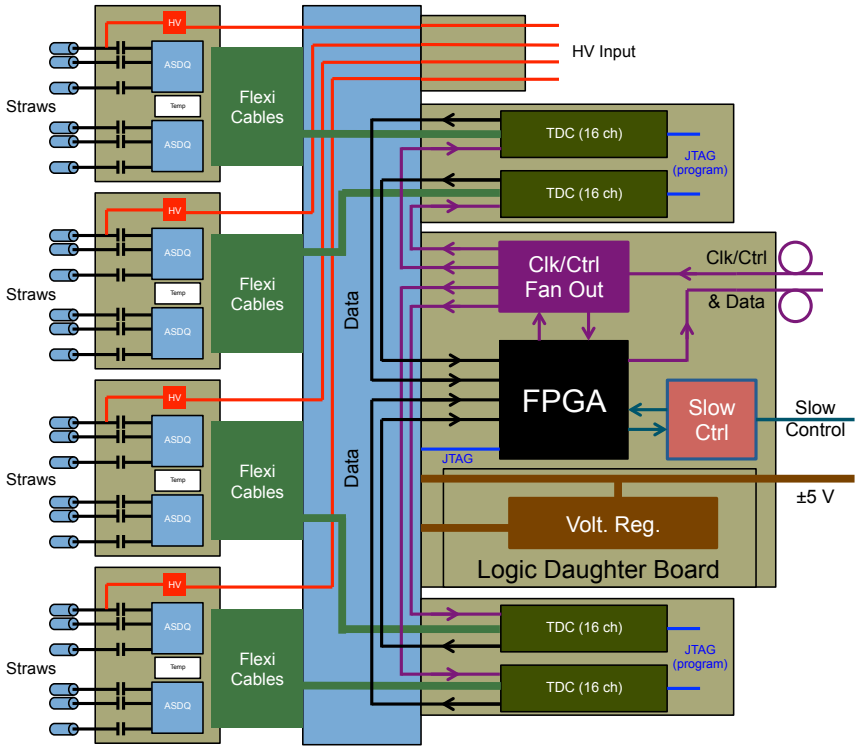

Figure 5.8: Tracker readout chain - Diagram courtesy of James Mott.

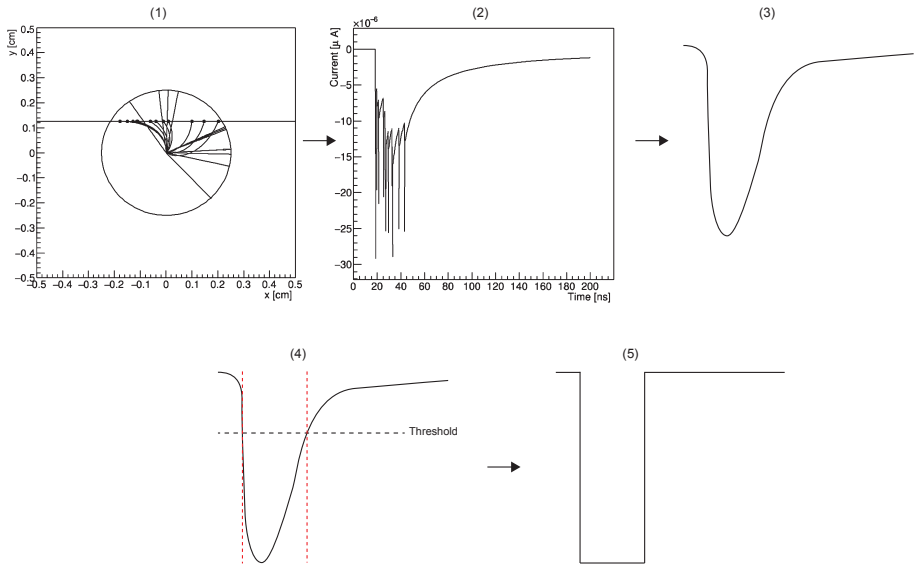

Figure 5.9: Stages of signal creation and ASDQ processing. 1) Ionising particle travels through a straw ionising gas along its track. 2) Signal created in the sense wire from multiple primary ionisations. 3) Signal smoothed into a single peak with baseline restoration 4) Threshold checked as well as detecting the leading and trailing edges. 5) Digital signal produced high for the duration between the leading edge and the trailing edge.

boards and two high voltage cards, these boards are split between the layers of the straws at different angles (known as a views).

5.4.2 Back-end electronics

The back-end electronics consist of the logic board, FC7 and AMC13 - for the complete tracker system of three tracker stations there are 48 logic boards (two per module), three FC7s and one AMC13, as shown in figure 5.7. Together they manage, synchronise and read out data from multiple front-end electronic boards. The logic boards mounted in the FLOBBER serve as an interface to the four TDC-ASDQ pairs found in one view of a straw tracker module, fanning out clock and control signals to these boards as well as collating all the data received into one data-block. The logic board has three external interfaces, a fibre optical link to the higher level backend electronics, a serial communication port to the slow control hardware and low voltage supply

line. Communication between the logic board and front-end electronics is through a backplane called the feedthrough board. This board also acts as a gas seal between the active gas inside the module and the atmosphere. The logic boards store configuration parameters for the operation of the TDCs and ASDQs in registers which can be read or modified via the slow control serial connection. The Logic Board receives the clock/control stream using the C5 (Clock-Command Combined Carrier Coding) protocol, at a rate of 10 MHz, via a fibre optic cable from the FC7, the same fibre cable is also used to transfer the output data at a rate of 25 Mbit/sec serial encoded using 8b10b.

The FC7 carries out a similar job to the logic boards by being responsible for fanning out clock and control signals to all the attached logic boards as well as collating the data it receives into a single data-block, during nominal operation each FC7 is connected to 16 logic boards via fibre optic cables. The three FC7 boards are located in a microTCA crate in the centre of the ring and each communicate via the backplane in the crate with the AMC13.

The AMC13 produces a single data stream from the data received from all three FC7s and is the top level board responsible for fanning out the clock and control signals to the global tracker system. The ACM13 is connected to a computer in the counting room via a Gigabit Ethernet (GbE) fiber where the data is saved to disk. Both the AMC13 and the FC7 boards have been re-purposed from the Compact Muon Solenoid (CMS) experiment at the Large Hadron Collider (LHC) at CERN.

5.4.3 Slow control

Serial communication with all the logic boards in a tracker station is carried out using a controller card housed in a custom made low voltage crate located in a rack on the inside of the ring, shown in figure 5.10. This makes it possible to issue commands to individual logic boards or broadcast messages to all logic boards at the same time. This system has multiple purposes; using the serial communication it is possible to send configuration parameters to the ASDQ and TDC boards and allows temperature

readings of each of the boards to be taken. The broadcast message function can be used for loading firmware onto all of the the logic boards and TDCs at once. There is one controller card per tracker station which is connected via USB to a rack mounted computer in the ring.

(a) Tracker Station 12

(b) Tracker Station 18.

Figure 5.10: Two photographs showing both currently installed tracker stations with their rack mounted hardware visible.

5.4.4 Low voltage

Low voltage power is supplied from the rack mounted low voltage boards to the logic board which manages power to the front end electronics. It would have been cost prohibitive to use individual commercial power supplies for the full 48 logic boards, so

Parameter	A333	A431
V_{max}	$4kV$	$8kV$
$V_{resolution}$	1 V	2 V
Current full scale	2 mA	$200\mu A$
Current resolution	$1\mu A$	$0.1\mu A$
Maximum Power	32 W	6.4 W
Max Ramp Up/Down	500 V/s	500 V/s
$Ripple_{p-p}$ (full load)	$< 80mV$	$< 150mV$

Table 5.4: Technical characteristics of the HV outputs for both HV cards used

custom made low voltage power supply boards were produced, these output +/- 5 V via a DB-9 cable to the logic board.

5.4.5 High voltage

As outlined in section 5.3, the straw tracker modules require a source of high voltage (HV) to create an electric field around the sense wire. This is achieved using a rack mounted CAEN SY127 crate which houses CAEN HV cards, each straw tracker module requires 8 HV inputs, one for each ASDQ. The CAEN SY127 crate can hold and operate 10 HV units which each have 4 HV outputs. Each tracker station has 8 tracker modules which gives a total of 64 HV channels to supply, so two CAEN SY127 crates are required, if fully populated with HV cards this gives 16 spare channels. This hardware has been repurposed from a different experiment as it is capable of suppling the correct voltage with long term stability to avoid varying gain values as well as being able to have a low trip current set point as to not damage the straw wall if a sense wire breaks. The specifications for the two different HV card used are given in table 5.4. The status for each channel is read out via an RS232C port on the CAEN SY127 to the rack mounted slow control computer for each tracker station. There is also a python based graphical user interface (GUI) for each HV unit to give a convenient way to apply changes per channel, this GUI is is shown in figure 5.11 where two modules are powered with one HV output tripped and shown in red.

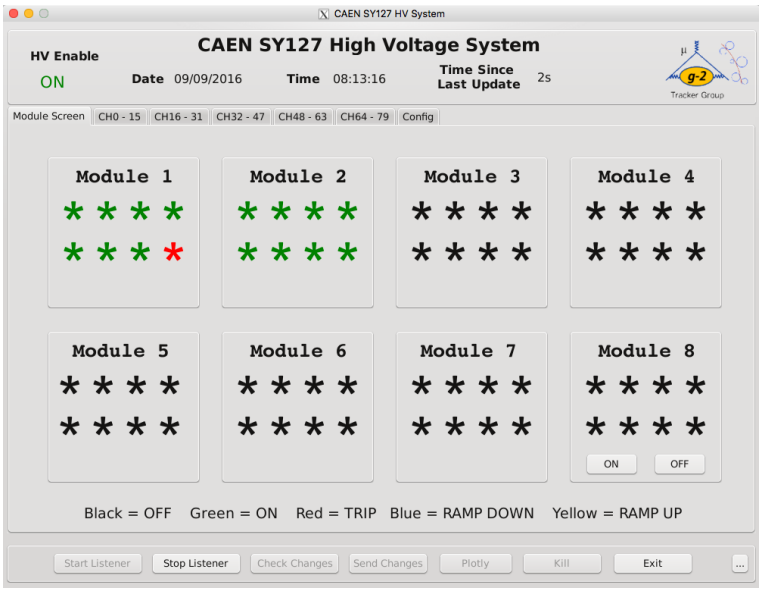

Figure 5.11: Main display of the HV monitor and control GUI showing the status of each of the HV channels required by a tracker station. Here it is clear to see that two tracker modules are currently being supplied with high voltage with one tripped channel.

5.4.6 Tracker services

To operate the trackers multiple services are required such as gas supply to the straws, water cooling to cool the internal electronics in each manifold and air cooling to cool the electronics in the FLOBBER.

The trackers operate with a 50/50 Argon/Ethane gas mixture supplied by a flammable gas delivery system. This is comprised of different stages, gas storage, automatic mixing of individual gases and precise pressure and flow control to each module. The gas is stored in a gas storage shed attached to the MC-1 building which houses eight liquid ethane cylinders and eight Argon gas cylinders, where the pressure to the experimental hall is limited to 20 psig and total flow is kept below 720 cc/min. The gas mixing occurs in the experimental hall and provides a 50/50 Argon-Ethane mixture by volume prior to being cycled through two filters and reduced to 2 psig where the line splits to be routed to the three tracker stations. Due to the delicate nature of the straws the pressure is reduced to 2-5 inches of water column on the exhaust of each module. Each tracker station is also fitted with a pneumatic three

way valve which can switch the flow to a tracker station between Argon-Ethane and Nitrogen. All the flow and pressure elements involved in mixing are closely monitored and automatically controlled by the PLC located in the computer room to ensure a precise mixture and to allow quick detection of leaks.

The water supply is required to cool the internal electronics, this is achieved with one water pump and reservoir per tracker station. The water leaves the pump, travels through a filter then passes through each tracker module in parallel. This system was designed to flow 1 litre per minute through each tracker module which is enough to cool the electronics in each manifold - which require 4 W per manifold - to below $35°C$.

Air cooling is required to cool the electronics in the FLOBBER, each of these boards have temperature sensors which read out into the slow control. The air cooling system consists of an air distribution system located outside of the ring which draws air through tubes connected to each tracker module, this is the preferred method as an off-the-shelf electrical fan connected to the FLOBBER would perturb the main storage ring magnetic field as well as having a small effect on the iron yoke temperature in these areas.

Chapter 6

Detector Construction

This chapter will give an overview of the detector construction carried out at the University of Liverpool along with the quality control steps taken during production to ensure performance requirements are met. Figure 5.3 shows a diagram of a completed straw tracker module with each component highlighted. Construction of each module was carried out in a class 5 clean room prior to being tested in a class 7 clean room.

Mechanical fabrication

Each of the straw tracker manifolds, vacuum flange and manifold lids are fabricated in the Physics Department Mechanical Workshop. The manifold is a complicated part which starts off as a block of stress relieved 6061 aluminium. This grade of aluminium was chosen for its relatively low magnesium content and therefore low magnetism. First the stock piece has one end faced off before locating details are machined in, shown in figure 6.1a. Then a 260 mm long cooling hole is drilled down the length of the manifold, this allows cooling of the internal electronics. The electronics pocket is then roughed out on a 3-axis milling machine, shown in figure 6.1b, before more complex features such as the angled straw holes, lid through holes and lid o-ring groove are machined on a 5-axis milling machine. Once this is completed many features are hand finished such as threading the holes needed for the ASDQ ground pins, threading the lid holes and deburring each of the straw holes using polishing wax and elasticated nylon cord

to prevent straw tears from occurring during population. Before use in a straw tracker module the fully machined manifold has an Alocrom 1000 coating applied which gives the manifold excellent electrical conductivity and corrosion resistance. A set of finished manifolds can be seen in figure 6.1c and 6.1d.

Once finished the position and diameter of each straw hole is measured precisely on a coordinate measuring machine (CMM) along with other features, such as the dowel holes and vacuum o-ring position, for a total of 1326 positions mapped out per manifold. This data is checked to ensure each measurement is within tolerance before the manifolds are paired up and fitted into the vacuum flange. These two processes are shown in figure 6.1e and 6.1f. This process would take around 6 hours by hand but after automation takes 50 minutes. This data is saved into a construction database which can be used for alignment studies throughout the lifetime of the detector.

Straw production

Each straw is constructed of two $6\mu m$ layers of Mylar wound in a spiral, with a $3\mu m$ layer of adhesive between the two layers. The inner surface has 500 Å of aluminium overlaid with 200 Å of gold as the cathode layer, while the outer surface has 500 Å of aluminium deposited to act as additional electrostatic shielding and reduces the straw leak rate [42].

Straws are produced approximately 130 cm long and are constructed with a removable paper insert for rigidity as well as making them easier to handle, the straws are transported in individual plastic tubes for protection. Prior to use a full visual inspection is carried out as well as measuring the resistance of the inner surface of a full straw, typically before removing the paper insert a long straw will have a resistance of approximately 200 Ω. Once the straw is prepared for use a gas leak test is carried out. The leak testing procedure involves filling a straw with a 50:50 mixture of Argon CO_2, sealing up the ends of the straws and placing this sealed straw into a chamber that is flushed with nitrogen. After flushing the chamber with nitrogen the amount of

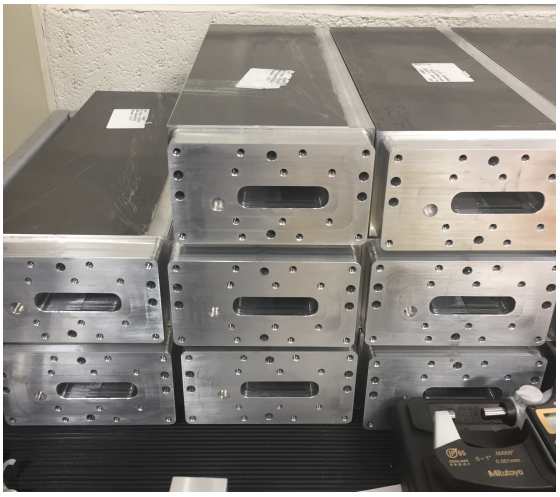

(a) Stock aluminium with one face machined and alignment holes added.

(b) Pocket for electronics roughed out on 3-axis CNC.

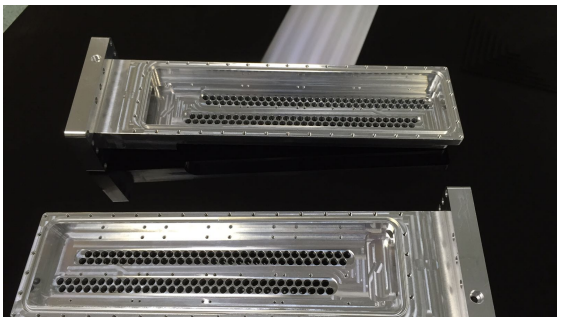

(c) Fully machined pair of manifolds.

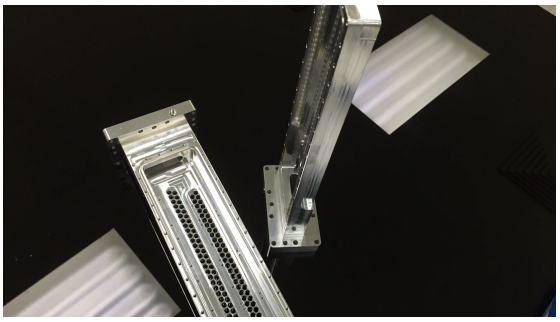

(d) Fully machined pair of manifolds.

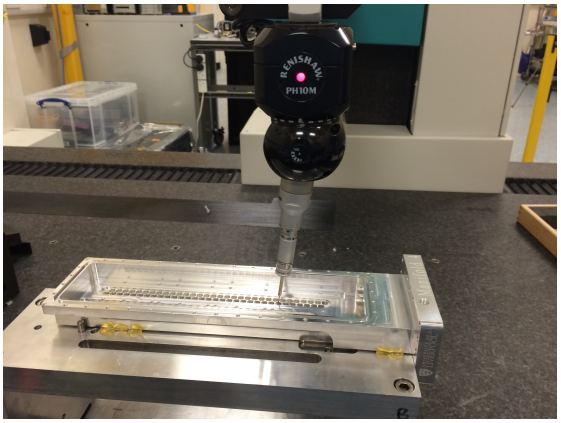

(e) Manifold undergoing metrology.

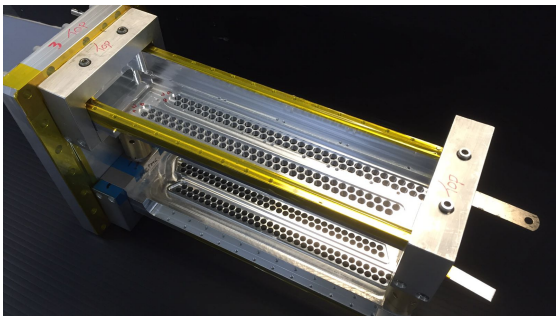

(f) Manifolds and flange paired with jacks

Figure 6.1: Stages of manifold production and module construction

CO_2 present in the chamber is monitored and can be used to determine the leak rate out of the straw. The straw leak testing setup can be seen in figure 6.3a.

There is a stringent tracker station leak rate limit of 4.5×10^{-5} Torr ·L/s, this limit was calculated to allow the storage ring vacuum to reach acceptable levels ($< 1 \times 10^{-6}$ Torr) after 24 hrs of pumping given the vacuum pump system specifications. This is necessary to allow the electrostatic quadrupoles to operate at nominal voltage without sparking promptly after pumping is started. This corresponds to a long straw leak rate limit of 4×10^{-4} cc/min, any straws above this limit is not used for module production.

Many tests were carried out during the prototyping stages to ensure straw tracker modules were optimally designed as well as being constructed without imperfection such as;

- Repeated pressure cycles of multiple straws to demonstrate robustness of the straw wall, glue seal and seams.
- Overpressure failure tests of straws where it was found that straws could routinely experience over 30 psi of pressure before tearing at a seam at 60 psi.
- Repeated tension cycle at extensions below the deformation point with leak testing before and afterwards showed no noticeable increase in leak rate.
- High precision mass tests of the straws before and after experiencing a humid environment showed that the straws are highly hygroscopic and absorb water. This can be mitigated through storage in a nitrogen environment.

Module production

Once the straws pass the leak testing stage they are cut to 90.8 mm using a custom made guillotine then have aluminium end pieces glued into each end using silver epoxy to ensure a good electrical contact. These end pieces allow the straws to be inserted and affixed into the manifolds as well as providing structural rigidity for plastic inserts - which hold the wire central in the straw. Half a tray of built straws can be seen in

figure 6.3b. After inserting all 128 straws into a pair of manifolds jacks are applied to hold the manifolds a set distance apart. Silver epoxy is then applied between the manifolds and the straw end pieces to achieve good electrical contact prior to a gas seal being made around each straw. The gas seal prevents gas from leaking into the vacuum and is made using Araldite 2020 epoxy with an added colouring agent. This is visible on the inside of the manifolds in figure 6.3c with the main gas seal being on the outside of the manifolds, seen in figure 6.3d and 6.3e. At this stage the lids can be fitted to allow a rough overpressure test to be carried out to ensure no leaks have been introduced during the early module production stages.

The 25 μm Gold plated Tungsten-Rhenium wire is threaded through a 'short' non-annealed gold plated copper pin and plastic insert. The pin is glued into the plastic insert and crimped between custom made jaws with 1 kN of force on a material testing machine. This built wire can then be threaded through a straw and fixed in place while the other end of the wire is threaded through a second plastic insert and a 'long' annealed pin prior to being hand crimped all while the wire is held under 30 g of tension from an attached mass to the free end. The two pins and two plastic inserts used were designed to position the wire within μm of the centre of the straw. The pin and insert used to achieve this on one side of a module can be seen in figure 6.3d. The long pins are annealed to reduce the force required to hand crimp the pin around the wire, figure 6.2 shows a comparison of the force required to crimp the annealed and non-annealed pins.

Once the module has been threaded with 128 wires the two manifolds are jacked apart a set distance to ensure equal tension is applied to each of the straws and all of the wires, and held in position with a carbon fibre post at the far end of the module. Each wire has its tension measured at this point with a custom made tension testing device, the requirement being 50 ± 20 g.[1] The device works by pulsing current down the wire at varying frequencies while in a strong external magnetic field. As the changing

[1]This fairly relaxed requirement is because there is no measurable operational difference between wires of differing tensions in this range. Additionally, the tension testing device has a precision of ± 5 g.

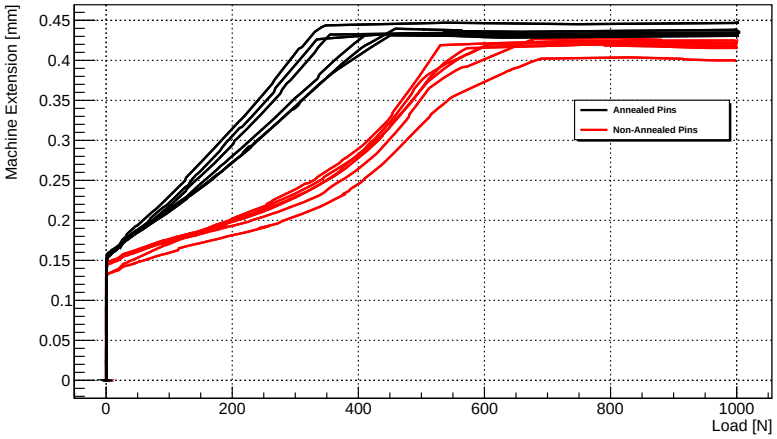

Figure 6.2: Force required to crimp the annealed and non-annealed pins.

electric field creates a magnetic field the wire resonates in the external magnetic field. After each pulse the current on the wire is read, if it is resonating strongly in the opposing external magnetic field a current will be induced on the wire. As the frequency of the current pulse changes it will pass through the resonating frequency of the wire, once this point is measured the tension on the wire can then be calculated.

After the tension and resistance of each wire have been measured and pass the requirements the ASDQ boards can be inserted onto the readout pins the rest of the HV and LVDS connections can be made and the snout, feedthrough board and lids can be attached to the module - a module with electronics fitted without lids can be seen in figure 6.3e. The module can then be paired up with the remaining front-end electronics and backend electronics and go through the pre-shipping performance tests, this include noise scans, vacuum tests, cosmic ray scans and source scans.

6.0.1 Pre-shipping performance testing

Multiple tests are carried out on each tracker module prior to shipment to FNAL, these tests ensure that there are no leaks present in the module as well as confirming that each channel is capable of holding high voltage, recording hits and can operate stably over a 24 hour period. Once these tests are carried out and recorded the module is

(a) Straw leak testing setup.

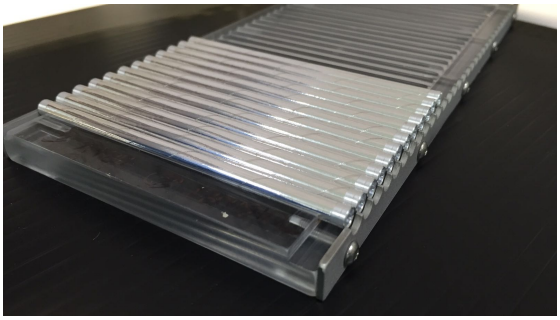

(b) Straw production.

(c) Straws glued into module.

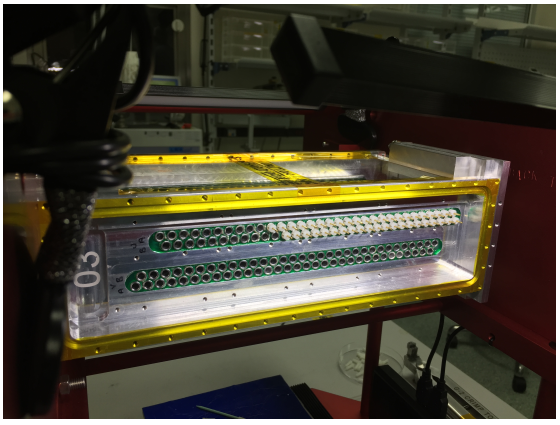

(d) Module in wiring jig.

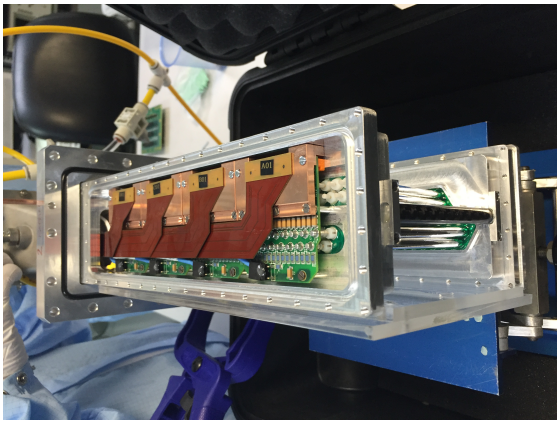

(e) Module with electronics fitted.

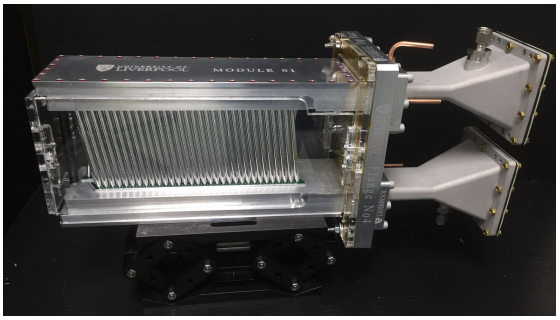

(f) Finished Module.

Figure 6.3: Steps through module construction.

Figure 6.4: Liverpool module test setup with Ar:CO_2 gas bottle, vacuum chamber, turbo pump, water cooling system, low voltage supplies and rack mounted high voltage and backend electronics.

shipped to FNAL where it undergoes further testing. These pre-shipping performance tests are carried out in a class 7 clean room to prevent any contaminants from entering the module, a photo of the vacuum tank and electronics test stand used can be seen in figure 6.4.

The leak rate of each module must be measured to be less than 5.5×10^{-6} Torr ·L/s to ensure the total leak rate of a tracker station is within the capability of the vacuum pumps in tracker station vicinity. This test is carried out by securing a module into the vacuum chamber, flowing Ar:CO_2 gas through it while pumping down the chamber with a roughing and a turbo pump. A graph of the vacuum pressure inside the chamber is automatically made and published onto a viewable graph to allow remote monitoring of the setup, typically the chamber has reached a suitable pressure within 24 hours. To measure the total leak rate - including permeation rate of the straws - the gate valve between the chamber and the pump is closed so the pumping speed goes to zero and the rise in vacuum pressure is recorded over the course of around 300 seconds.

This change is built up from either outgassing, where the pressure will level out after an initial rise, or a leak, where the pressure carries on rising when the pumping speed is zero. This test gives the rise in pressure for a given time which allows the total leak rate to be calculated. If the leak rate is above the specification of 4.5×10^{-5} Torr ·L/s then further tests are carried out to diagnose the problem.

Once the vacuum tests are completed noise scans are performed, this immediately shows if all connections to the internal electronics are made correctly as well as detecting other sources of unwanted noise. This is carried out by raising the discriminator threshold from 0 - 500 mV to find the point at which the noise hits stop. A graph of the output is shown in figure 6.6, typically the noise level is below the 200 mV level and further investigation will occur if this value is not met.

High voltage scans are performed to detect broken wires or shorted connections between the sense wire and the aluminium manifold as well poor internal high voltage connections. These scans involve applying HV in stages to each ASDQ (16 sense wires) from 0 - 1500 V, the current draw on each channel can be monitored during this period to ensure desired operation, if each channel successfully ramps up to 1500 V a 24 hour test is taken to ensure long term stability.

After it has been proven that the module is stable at high voltage for over 24 hours as well as being below the desired leak rate the data acquisition (DAQ) tests can be carried out. These involve exercising the full DAQ system to take cosmic data as well as a radioactive source scan using a collimated Strontium−90 source to ensure each channel is capable of detecting hits.[2] This test also detects if any channels are producing noise hits which would require further attention.

Given successful completion and full documentation of the above tests the module is encased in a perspex shield, wrapped in an antistatic plastic and packaged in a crushproof *Peli 1510 Protector Case*. The modules gas inlet and outlet connections are partially covered but not fully sealed to allow the pressure to equalise during transport and avoid damage to the straws.

[2]Strontium-90 (^{90}Sr) undergoes β^- decay with an energy of 0.546 MeV to the yttrium isotope ^{90}Y which in turn undergoes β^- decay with a decay energy of 2.28 MeV.

6.1 Arrival tests and installation

Modules are transported via carry on hand luggage during the flight from the United Kingdom to Chicago, precautions are made to prevent damage to the tracker modules from the pressure changes that occur during the take off ascent and landing descent. Arrival tests are carried out to ensure no damage to the modules occurred during transport as well as to characterise the operational properties of each channel, these tests include vacuum tests, noise scans as well as gain and plateau scans.

6.1.1 Vacuum performance

As mentioned in section 6.0.1 the leak rate of each module is required to be less than 4.5×10^{-5} Tl/s prior to shipping but due to the possibility of damage during transport these tests are redone. It is also important to take an independent measurement to verify the leak rate prior to installation within the storage ring vacuum (SRV). These tests use the same method as outlined in section 6.0.1 but have the ability to flow both $Ar : CO_2$ as well as $Ar : C_2H_6$.

6.1.2 Module testing

A dedicated test stand was constructed to carry out gain and plateau studies in order to find the optimal operational wire voltage as well as carrying out quality control arrival tests. This setup provides precise movement of a "horse-shoe" holder in the same plane as the straws using a stepper motor, with one side of the horse-shoe being a radioactive source holder and the other being a collimated silicon photomultiplier detector with a module placed in between. This system is integrated into the main straw tracker DAQ and MIDAS sequencer which allows for automated measurements at multiple space points to be made with little to no user interaction. The first data taking test which is undertaken on a tracker module on arrival is a discriminator threshold scan. This threshold value sets the magnitude of the signal required to register a straw hit and quickly shows any problems which may have arisen during transport. This must be set

above the electronic noise level as well as above the signal deposited by low energy secondaries and not too high as to miss hits from decay e^+ from the stored μ^+. Figure 6.5 shows a typical noise scan carried out with a module on arrival at FNAL, from this it can be seen that a threshold value of 200 mV is suitable.

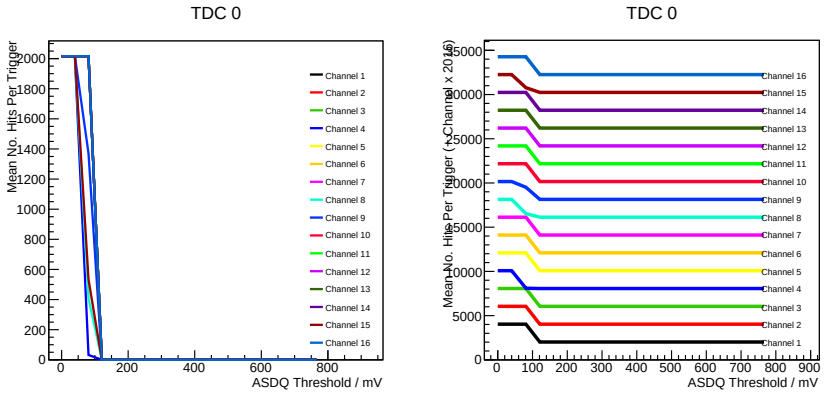

Figure 6.5: The number of hits for each channel versus the ASDQ board discriminator threshold voltage. On the right hand side figure each channel is separated to allow for the behaviour of each channel to be visible.

Plateau measurement

The plateau measurement is required to ensure the operational voltage is set to a point where the detector operates as a proportional counter, this is where all ionising events are detected and changing the operational voltage by a small amount does not result in a large change in the measured rate or a change in the electron drift velocity, v_d. If the voltage is set too low there will be a relatively low electric field strength around the sense wire and therefore interactions which liberate few electrons will not generate a signal size larger than the discriminator threshold, whereas if the voltage is set too high the gas in the straw starts to breakdown and many hits are registered. There exists a plateau region between these two points, the ideal voltage setting is close to the high end of the plateau region as at this point the resolution of the straw is maximised due to the increased gas gain.

This measurement is taken by setting the threshold value to above the noise level and recording the number of hits for different voltage values coming from a radioactive

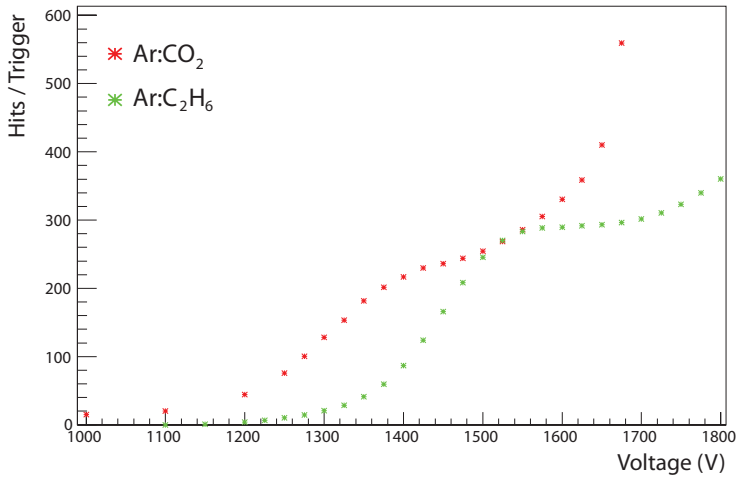

Figure 6.6: Plateau scan carried out on a production module with both a 50:50 Argon Ethane mixture as well as an 80:20 Argon CO_2 mixture.

source. Typically a Strontium-90 (^{90}Sr) source is used to carry out this measurement, ^{90}Sr undergoes β^- decay with a decay energy of 0.546 MeV - distributed to an electron and a anti-neutrino - to the yttrium isotope ^{90}Y which in turn undergoes β^- decay with a decay energy of 2.28 MeV. Figure 6.6 shows an example of a plateau scan carried out at a threshold of 200 mV using both Argon Ethane gas with a 50:50 mixture as well as Argon CO_2 a 80:20 mixture.

For Argon:Ethane it is clear that at low voltages, less than 1300 V, the gas gain is too low and straw events do not make it above the 200 mV threshold. At 1400 V the rate increases rapidly as the electronics record a larger fraction of the impinging β particles utill a plateau is reached at around 1550 V. This is the point at which approximately 100% of the impinging β particles are recorded as increasing the voltage, and gas gain, results in the same number of straw hits. At approximately 1700 V the plateau starts to up turn indicating a breakdown of the gas in which multiple straw hits are recorded for a single ionising event. From this it can be shown that the operational voltage set point should be approximately 1650 V.

Gas gain measurement

The principle behind measurement is to inject a known charge into a straw and record the detected charge. For this a ^{55}Fe source is used which decays via electron capture to ^{55}Mn emitting K-shell x-rays at 5.89 and 6.49 keV. The 5.89 keV x-rays will be the peak used as they have almost an order of magnitude larger branching fraction than the 6.49 keV x-rays but due to the limited energy resolution of a gaseous detector these two energies tend to be indistinguishable [57]. When an x-ray from the ^{55}Fe decay ionises an Ar atom an Ar K-shell x-ray with an energy of 3 keV is also emitted, these peaks can be seen in figure 6.7. Garfield simulation was run to measure the number of electrons produced from a single 5.89 keV x-ray, the results seen in 6.8 give approximately 225 electrons per 5.89 keV x-ray this corresponds to a deposited charge of 0.036 fC. Due to the electronics used it is not possible to directly measure the charge on the wire, so to measure the gas gain the number of hits per trigger is recorded for increasing threshold values while holding the voltage constant, it is then possible to fit the peak given by the 5.89 keV x-ray to give the corresponding threshold value in mV. For a 1275 V gain scan - shown in figure 6.9 - the peak of the 5.89 keV x-ray and fit is shown. This corresponds to a threshold value of 592 mV which, given the conversion of 2 fC into the pre-amplifier of the ASDQ resulting in 45 mV signal at the baseline restoration output, gives a charge of 26.31 fC measured [58]. A scan can be carried out for many different voltage values and each time finding threshold value which corresponds to the mean of the 5.89 keV peak to produce a plot of voltage verses mean threshold value, shown in figure 6.10. Due to restrictions within the electronics used this scan can not be carried out at the operational voltage as a saturation point is reached at around 1400 V.

Overall, 22 straw tracker modules were constructed and delivered. 16 modules are currently installed in the storage ring and operating well, from the modules currently installed 99.7% of the channels are fully operational.

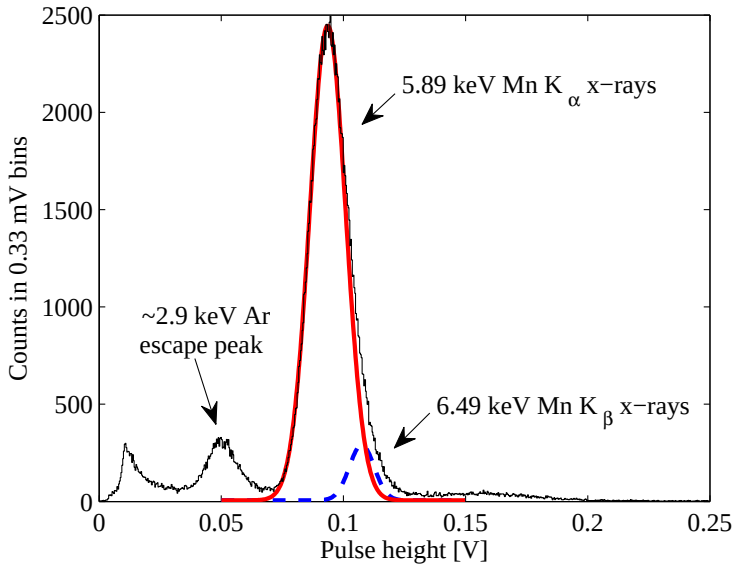

Figure 6.7: Iron-55 emission spectrum showing the 5.89 keV peak of interest.

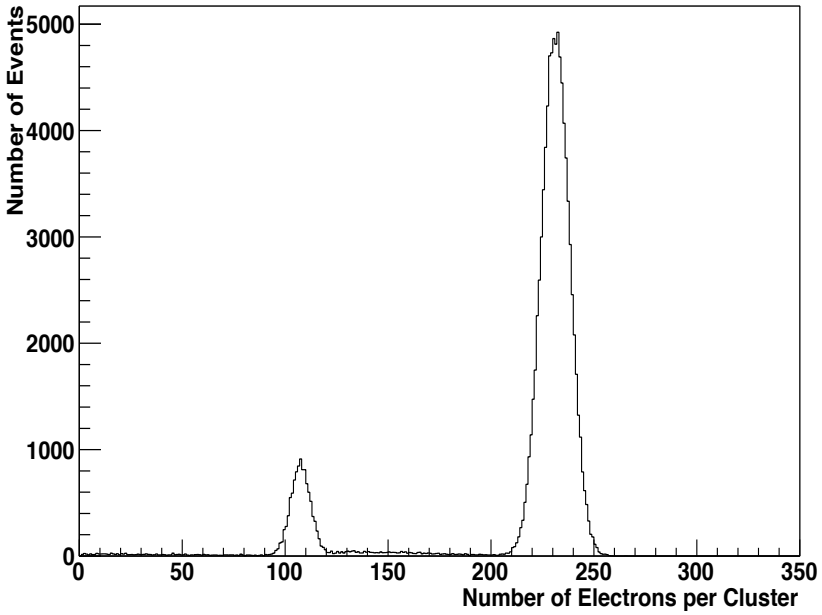

Figure 6.8: Number of electrons produced from a single 5.89 keV x-ray which travels through a straw.

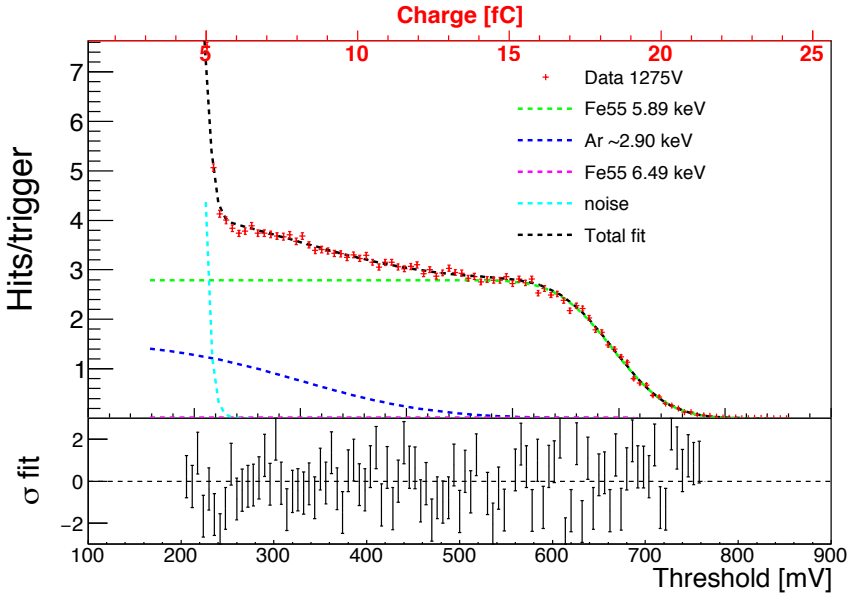

Figure 6.9: Gain scan at a voltage set point of 1275 V where the fitted functions are an exponential for the noise and an error function for the peaks

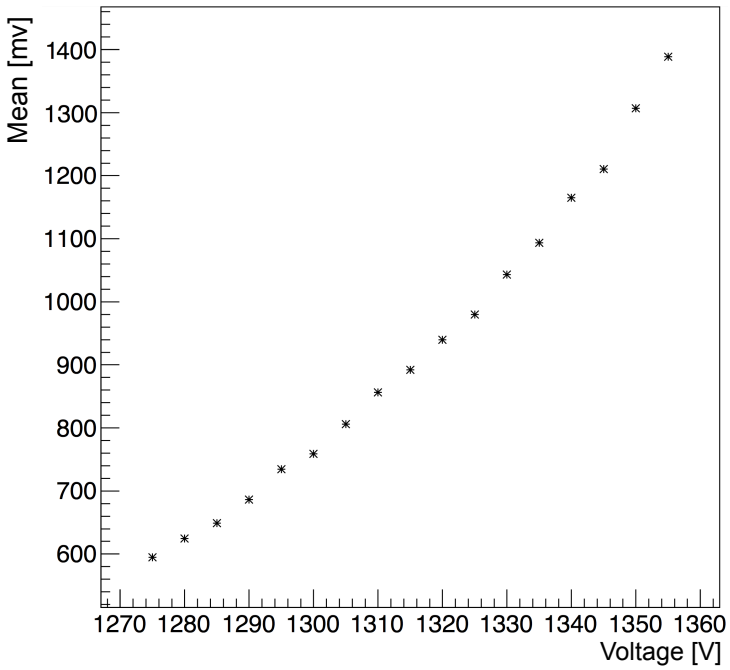

Figure 6.10: Scan over multiple voltages showing the mean of the fit to the 5.89 keV peak in mV.

6.2 Track reconstruction

As mentioned in section 4.6 the data outputted from a tracker module consists of the hit channel and hit time. This information goes through many stages to reach a reconstructed track, the simplest case of a track fit in which each layer of straws has a single hit coming from a single positron traversing the tracking station will be presented here. The important stages of track finding and track fitting are,

- Straw hits are grouped in time and separated into time islands (straws which register a hit within a $\sim$ 80ns time window) with the aim of grouping all straw hits from a single track into a single object.
- Hits within each time island are grouped spatially into clusters of hits in neighbouring straw tracker layers in a single view.
- Seeds are then formed by grouping clusters in neighbouring straw tracker views.
- Track candidates are formed of groups of seeds which are close in space.
- The t_0 for each straw hit in a track candidate can then be calculated and used to work out a drift distance for each straw.
- Tracks are formed using Geane [59] based track fitting using track candidates as an input.
- Fitted tracks can then be extrapolated backwards to decay point as well as forwards to calorimeter.

These steps can be seen in figure 6.11, 6.12, and 6.13.

During the 5th step, the drift distance in each straw is determined. This is achieved by subtracting the the time at which the particle entered a straw, t_0, from the hit time, t_h, to calculate the drift time, t_d, as the hit time is composed of both the t_0 as well as the drift time, t_d,

$$t_h = t_0 + t_d. \tag{6.1}$$

The drift time and drift distance plots as measured during data taking are given in figure 6.16 and figure 6.17 respectively. It is possible to infer the t_0 in multiple ways, either by using the hit time in a coincident calorimeter event and subtracting the time of flight between the two or by using the anti-correlation between the DCA for two hit straws in the same straw tracker view. This relation is simple for a straight, normally incident particle as the sum of the DCA for the two straws equals the pitch between straws in a view, d, then knowing the constant drift velocity, v_d, for the gas used the t_0 can be determined,

$$t_0 = \frac{1}{2}\left(t_{h1} + t_{h2} - \frac{d}{v_d}\right). \tag{6.2}$$

Calculation of the t_0 allows the drift time in each straw to be calculated given equation 6.1 and using the constant drift velocity v_d (calculated using Garfield simulation, as explained in section 5.3.1) once more allows a DCA in each hit straw to be calculated, which in 3D is a drift cylinder centred on the wire the full length of each hit straw. When looking at a single hit straw the drift distance is not enough information to know which side of the straw the particle travelled through, this ambiguity is removed when including the DCA from the straw in the next layer in the same view - as shown in figure 6.11. At this point the tracks position through these two straws in the same layer (a doublet) is known, which gives a line of possible positions the full height of the straws, to gain the vertical position of the track the next two layers of straws in the module have to be used. Carrying out the same procedure for the hits in the straw doublet in the next view of straws gives a second line of possible positions and given the stereo angle between the two views the intersection point of these two lines gives a 2D hit position - shown in figure 6.12.

Given this information a track fit can be carried out, for this the Geane [59] ('Geometry and Error Propagation') package is used. The Geane fitting routines originated in Fortran and was used in the PANDA experiment with some success [60]. Geane is a least squares global χ^2 minimisation fitting algorithm, which makes use of the Geant4 error propagation routines [59]. In absence of energy loss a charged

particle will follow a helical trajectory in a uniform magnetic field and the tracking of the particle as well as error propagation on a helical trajectory can be performed analytically. However, the straw trackers sit as close as possible to the muon storage region so lie within a region of varying magnetic field, shown in figures 6.14 and 6.15. The radial field in the tracking region raises from 0 T at the outer ends to approximately 0.3 T at the inner top and bottom ends while the vertical field drops roughly 50% from the storage dipole field of $\sim$ 1.45 T. While in this nonuniform magnetic field the tracking is performed in steps, this is one of the main motivations for using the Geane fitting algorithm and routines as it provides direct access to the Geant4 [61] geometry and field. For g-2 the tracking code was written to only require the U-layer or V-layer hit information, rather than a precise 2D hit position per straw. The χ^2 for a track can be defined by dividing the residuals of measured and predicted track parameters by their errors,

$$\chi^2 = (\vec{p} - \vec{x})^T(\sigma^{-1})(\vec{p} - \vec{x}), \tag{6.3}$$

where $\vec{p}$ are the predicted track parameters from a fit to the measured track parameters $\vec{x}$, and σ is a covariance matrix of errors on the fitted track parameters. By minimising this χ^2 with respect to the track parameters the track fit can be improved iteratively [59].

After calculating the track fit parameters for a track travelling through the straw tracking stations an extrapolated track can be formed both forwards towards the calorimeter as well as backwards towards the muon decay position. The extrapolation is carried out using a Runge-Kutta-Nyströem algorithm designed to solve second-order differential equations such as the equation of motion of a charged particle travelling through magnetic field. Performance of the track fitting and extrapolation is given in section 6.4.

It is important to note that the simple example presented here is true for a straight track travelling perpendicular to the straw planes. In reality these conditions are not true and more complexity arises, namely the fact that more than one possible track trajectory through the drift circles in the seed and cluster formation are possible. This

creates a left-right ambiguity for a track going through different straws, this is currently overcome by trying multiple track fits, one for each combination, and seeing which gives the best fit.

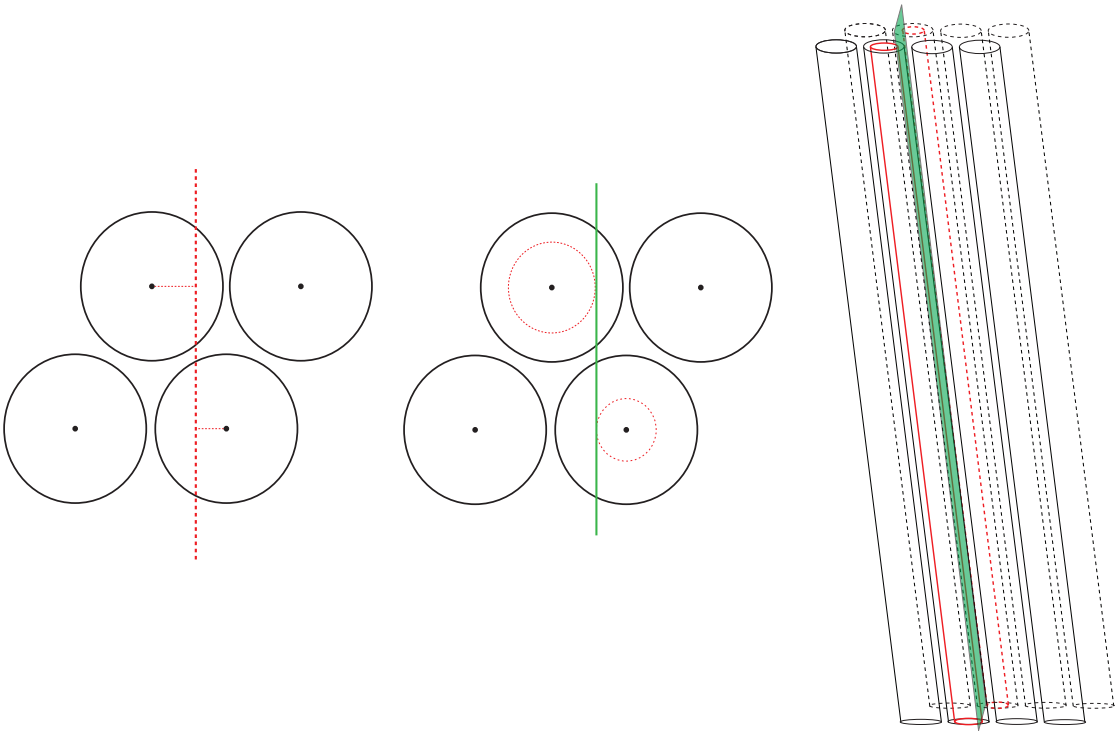

Figure 6.11: Formation of clusters for a normally incident track.

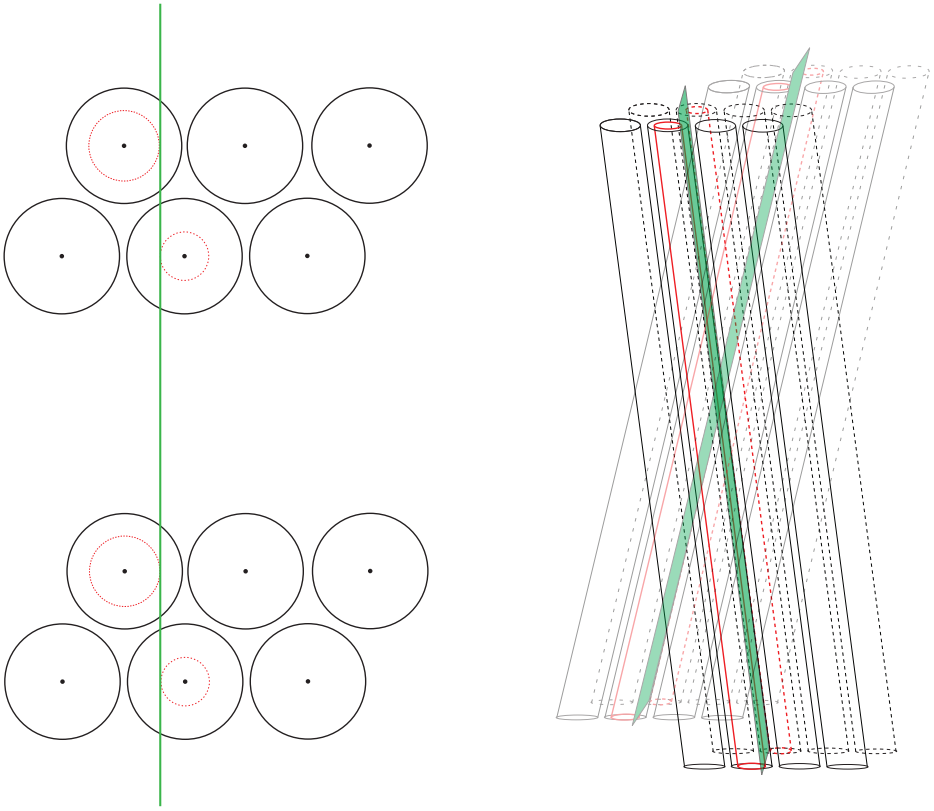

Figure 6.12: Formation of track seeds for a normally incident track.

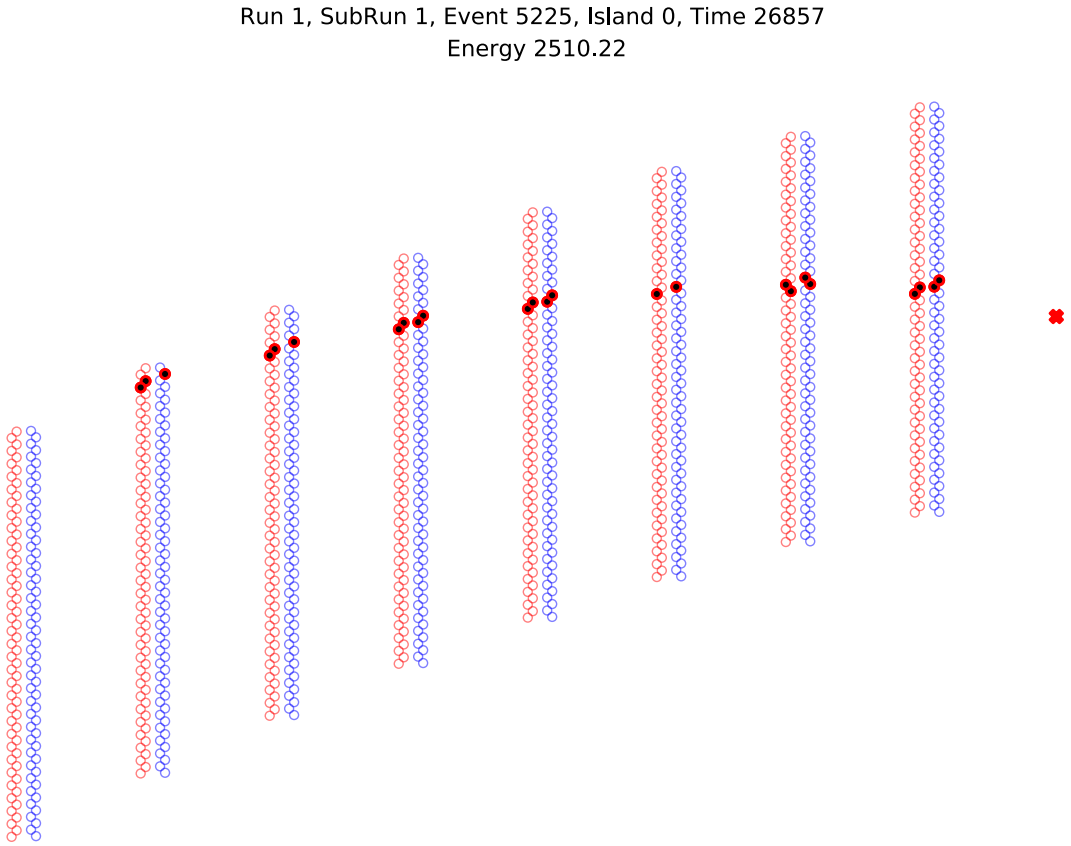

Figure 6.13: Event display showing an example of a track candidate.

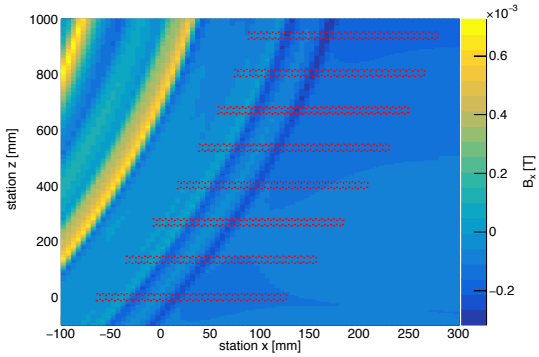

Figure 6.14: Radial component of the magnetic field in storage region at the centre of the straw trackers.

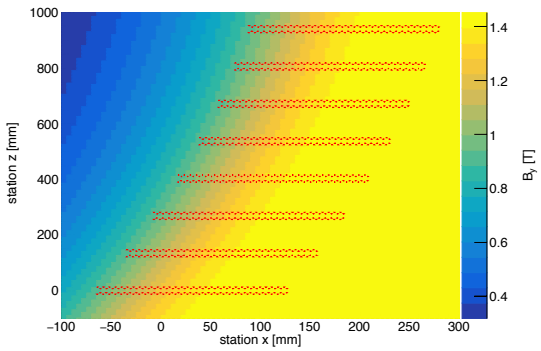

Figure 6.15: Vertical component of the magnetic field in storage region at the centre of the straw trackers.

6.3 Straw tracker installation

After each straw tracker module has undergone testing and proven suitable to be used in the experiment they are removed from the vacuum chamber and packaged in a modified protective case and flushed with nitrogen for 24 hours. The modules are then transported across the FNAL site in their protective Nitrogen filled cases and carefully installed into the storage ring vacuum (SRV) chambers and fitted with the water cooling lines, air cooling ducts, low voltage power cables, readout fibres, slow control cables as well as high voltage cables. These connections are verified while cooling tests are performed and once a SRV pump down is initiated a Helium leak check can be carried out to ensure the modules have been installed without introducing a leak. Care is taken to ensure the vacuum surfaces as well as viton o-ring are clear of debris as well as torquing down each vacuum flange bolt to a set value in the correct order, to compress the o-ring evenly as leaks can easily be introduced. Leaks are detected during a Helium leak test by attaching a Helium mass spectrometer to a vacuum port and pumping down and measuring the amount of Helium detected while spraying small amounts of Helium gas around the newly installed tracker module. If a leak is detected a more focussed investigation is carried out. In addition to the installation procedure outlined above the SRV pressure is monitored during pump down as well as when the low voltage electronics inside the manifolds are powered. Any change in pressure when the low voltage is applied could indicate an increased outgassing rate from the manifolds with increased temperature, indicating that surface water may be present on the modules. This effect was noticed during early installation of tracker modules and subsequently solved by flushing the SRV with nitrogen for 24 hours after any vacuum port is opened to the atmosphere.

6.4 Tracker performance

The Muon g-2 experiment at Fermilab received and stored beam for the first time during the engineering run carried out during the summer of 2017. This allowed the

first full test of the performance of a straw tracker station as well as the first test of the tracking code using experimental data. Shortly after this run physics data taking started which is the data sample used to produce the tracker data plots as shown in figure 6.18 to 6.23.

Figure 6.18 shows the time of received tracks with momentum greater than 1.8 GeV showing the clear g-2 oscillation. Figure 6.19a and 6.19b show the momentum of recorded tracks for all times and all times after 50 μs where the lost muon peaks are clearly visible in figure 6.19a.

The extrapolated beam profile is given in figure 6.20 with the radial and vertical profiles given in 6.21a and 6.21b. The radial profile versus time is given in figure 6.22a and 6.22b, for track station 12 and 18 respectively, showing the coherent betatron oscillation of the stored muon beam.

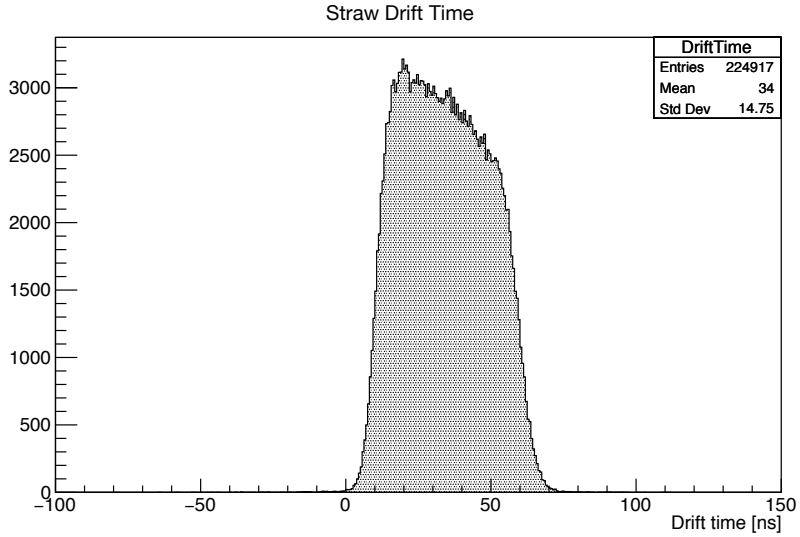

Figure 6.16: Global straw drift time as recorded during the physics data taking period.

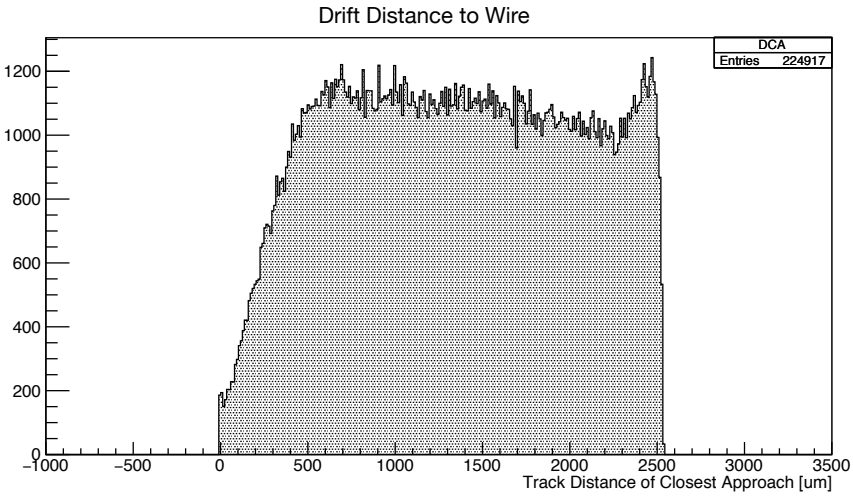

Figure 6.17: Global straw drift distance, where the drift velocity used is 54.6 $\mu m/ns$ as determined from Garfield simulation.

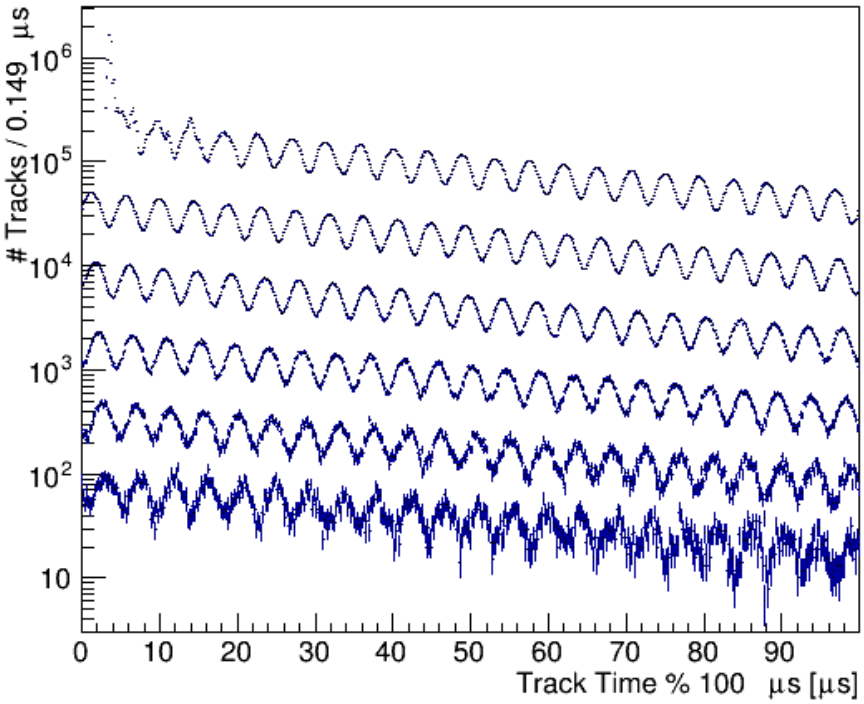

Figure 6.18: The time at which the straw tracker recorded a track with a momentum greater than 1.8 GeV.

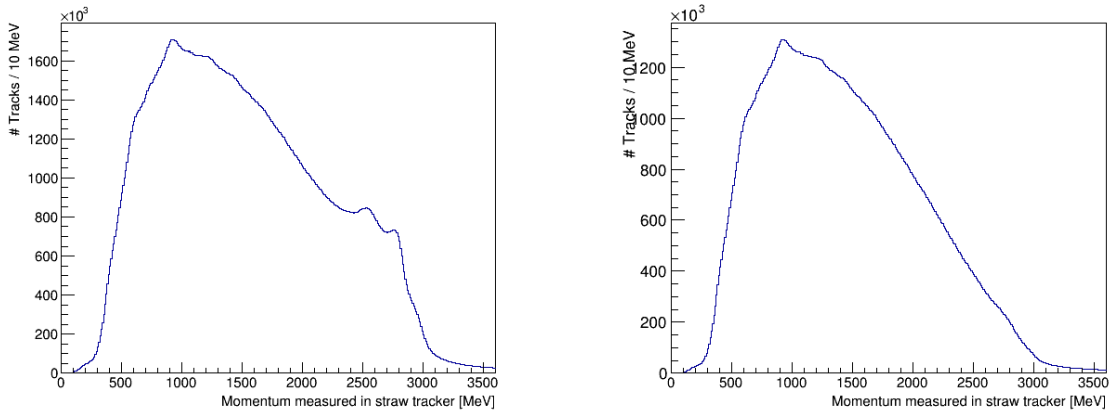

(a) All recorded tracks.

(b) Tracks recorded after 50 μs.

Figure 6.19: Track momentum distribution for tracks, *(left)*, as well as all tracks recorded after 50 μs, *(right)*, where the peaks around 2500 MeV and 3000 MeV are from lost muons at early times.

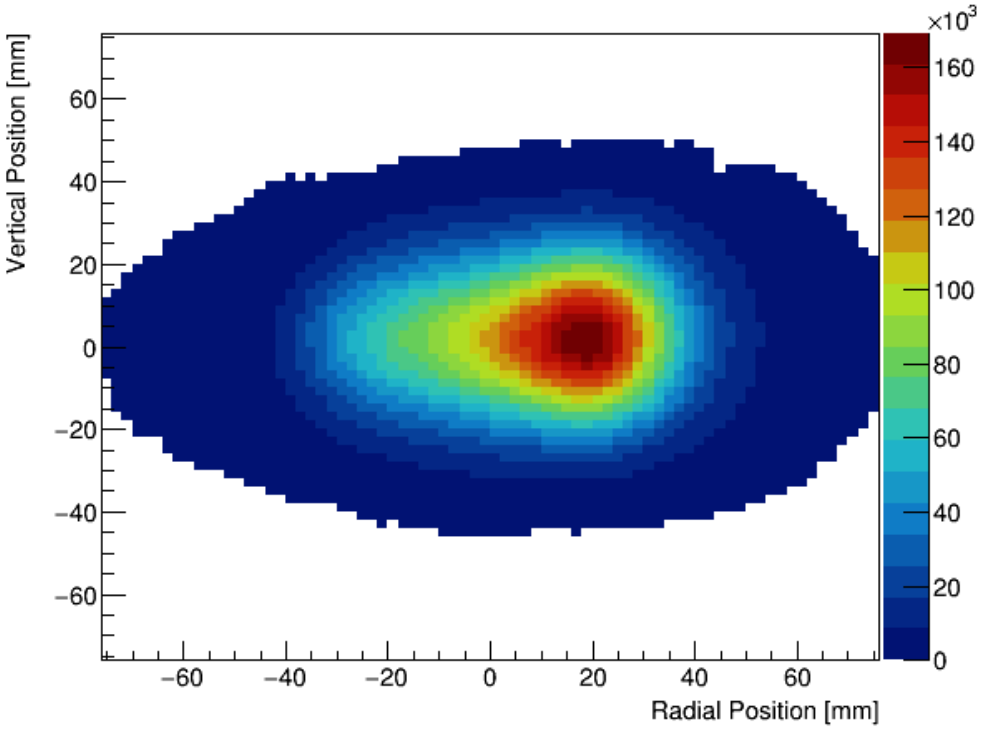

Figure 6.20: Track reconstructed decay position for all extrapolated tracks.

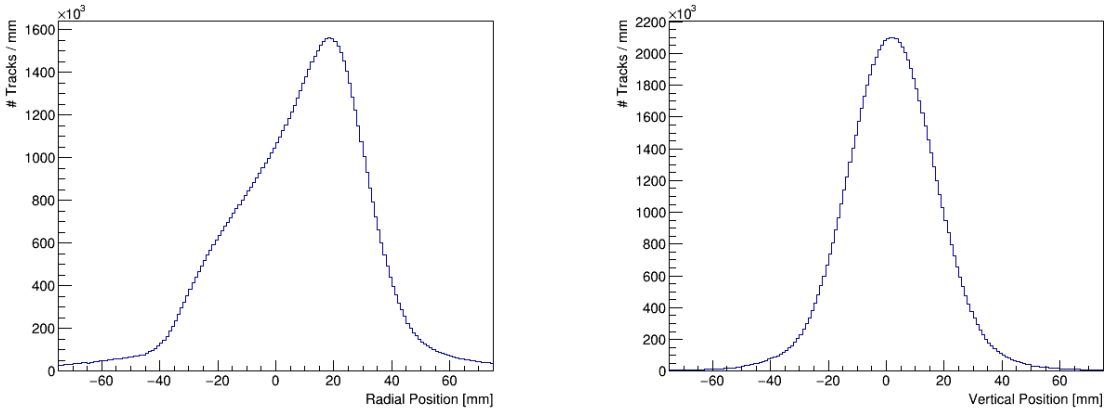

(a) Reconstructed decay radial position.

(b) Reconstructed decay vertical position.

Figure 6.21: Vertex radial position, *(left)*, and vertical position, *(right)*, for all tracks recorded.

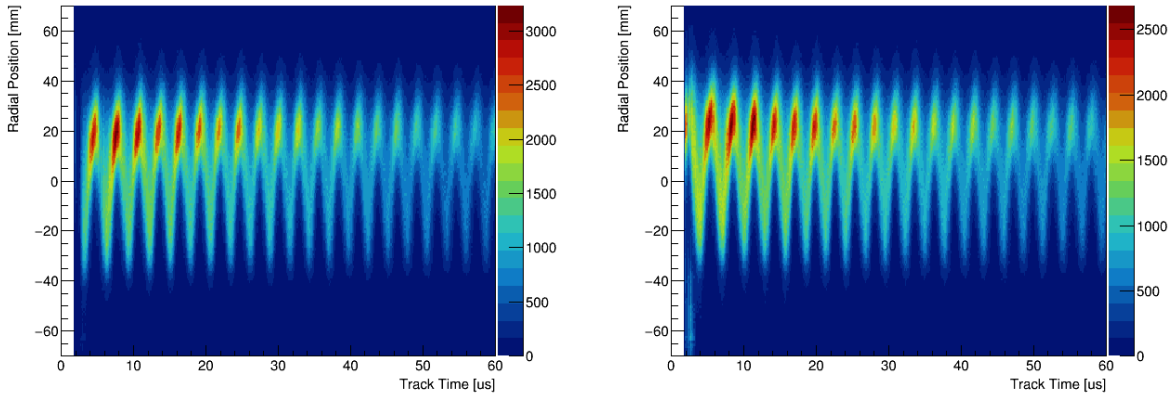

(a) Tracker Station 12 (b) Tracker Station 18

Figure 6.22: Track reconstructed decay radial position for tracker station 12 *(left)*, and tracker station 18, *(right)*, versus time for all tracks recorded.

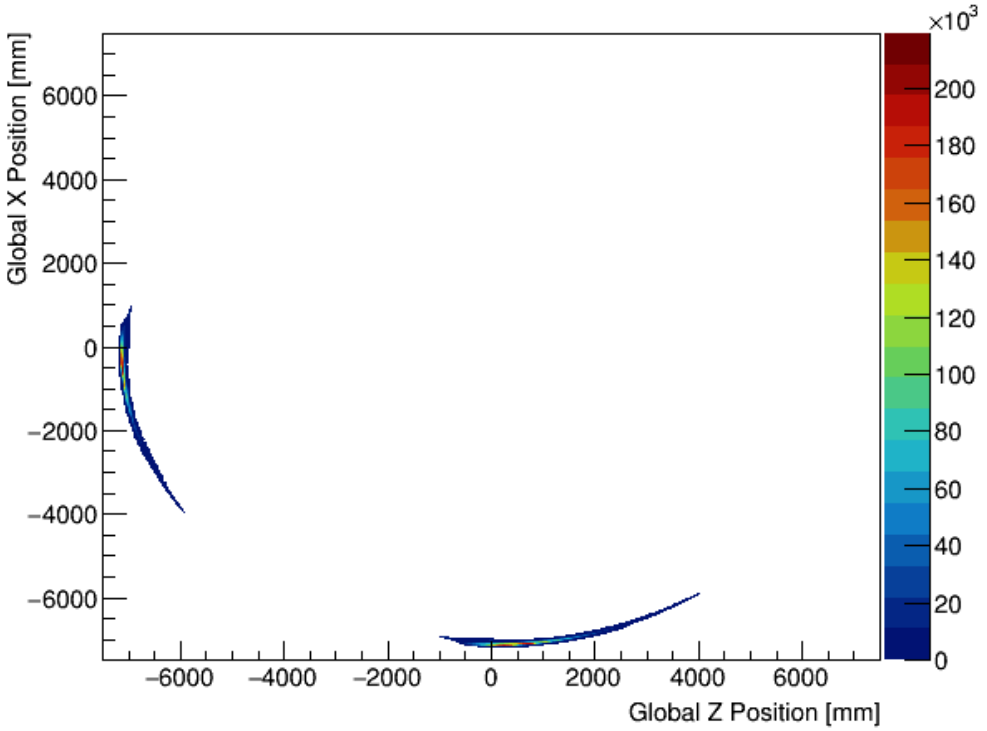

Figure 6.23: Track reconstructed decay position around the ring, top down view. With station 12 at the bottom middle of the figure and station 18 on the left of the figure.

6.5 Data quality monitoring

To enable real time monitoring of the performance of the detectors, quality of the data being taken as well as key beam related parameters a Data Quality Monitor (DQM) tool was developed within the *art* software framework. This tool is capable of receiving data from the data taking MIDAS server, converting the MIDAS banks to *art* event data (which allows any *art* module produced for reconstruction or analysis to be run over the data) before being published across a 0MQ socket to a javascript node server for visualisation. As the visualisation happens on the client side there is very little demand on the server if many peers are connected.

For the straw trackers there are many uses for this tool during running:

1. Ensure the data being taken is free of errors and can be processed.
2. Monitor the number of hits in each straw in a tracker module to check for dead or noisy channels - shown in figure 6.24.
3. Measure the straw drift time from module to module to ensure no contamination has entered the gas.
4. Display tracking related quantities for data currently being taken, including the momentum of each track, p-value as well as the number of clusters, seeds, tracks and vertices as a function of time.
5. Visualise the reconstructed beam spot built up from extrapolated tracks

These plots allow anyone on shift to easily monitor the health of the detector system and promptly raise an alert if any problems arise as well as being a great tool for an expert to gain information about the current running configuration by being able to see the beam profile in near real-time. This tool was also heavily during straw tracker production to allow quick and easy testing.

Shown in figure 6.24, 6.25, 6.26, 6.27 are examples of the DQM displays. Figure 6.24 shows a simple bar chart displaying the number of hits recorded in each straw

of a tracker module split between the two views, this allows easy identification of problems. Figure 6.25 shows a reconstructed beam profile recorded during initial commissioning. Figure 6.26 shows the main DQM display for a tracker station, the top plot shows backwards extrapolated muon decay position around the ring, below this the reconstructed beam profile is shown. The two distributions visible in the reconstructed beam profile plot is due to positrons building up the distribution on the right hand side and protons on the left hand side, protons were present in the beam during early commissioning as the delivery ring was not used. This distribution of protons is also visible in the plot below which shows the reconstructed track momentum. The plots below this show the number of clusters, seeds, track candidates, tracks and extrapolated vertices per event. Lastly, in figure 6.27 the occupancy of the tracker station at different time windows throughout the fill is shown, last time window shown is visibly more occupied than early and middle time windows, again, this is due to the protons being in the beam and being 'released' as the electrostatic quadrupoles are turned off at late times.

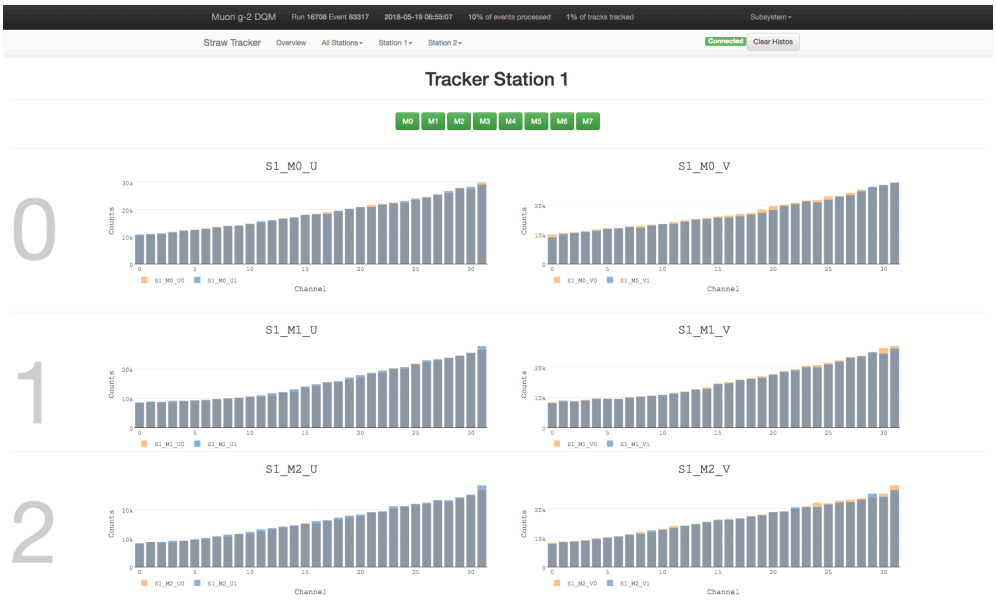

Figure 6.24: Data Quality Monitor (DQM) page showing the hits in the first three straw tracker modules of tracker station 1 in near real-time. The storage radius is close to the higher numbered straws so are expected to have more hits.

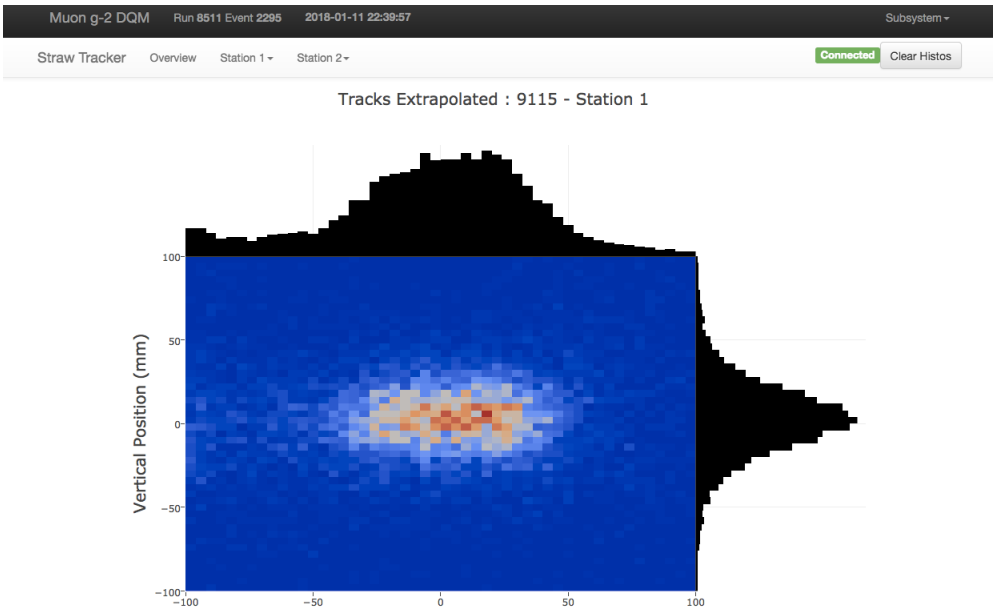

Figure 6.25: Data Quality Monitor (DQM) page showing the beam spot during data taking period.

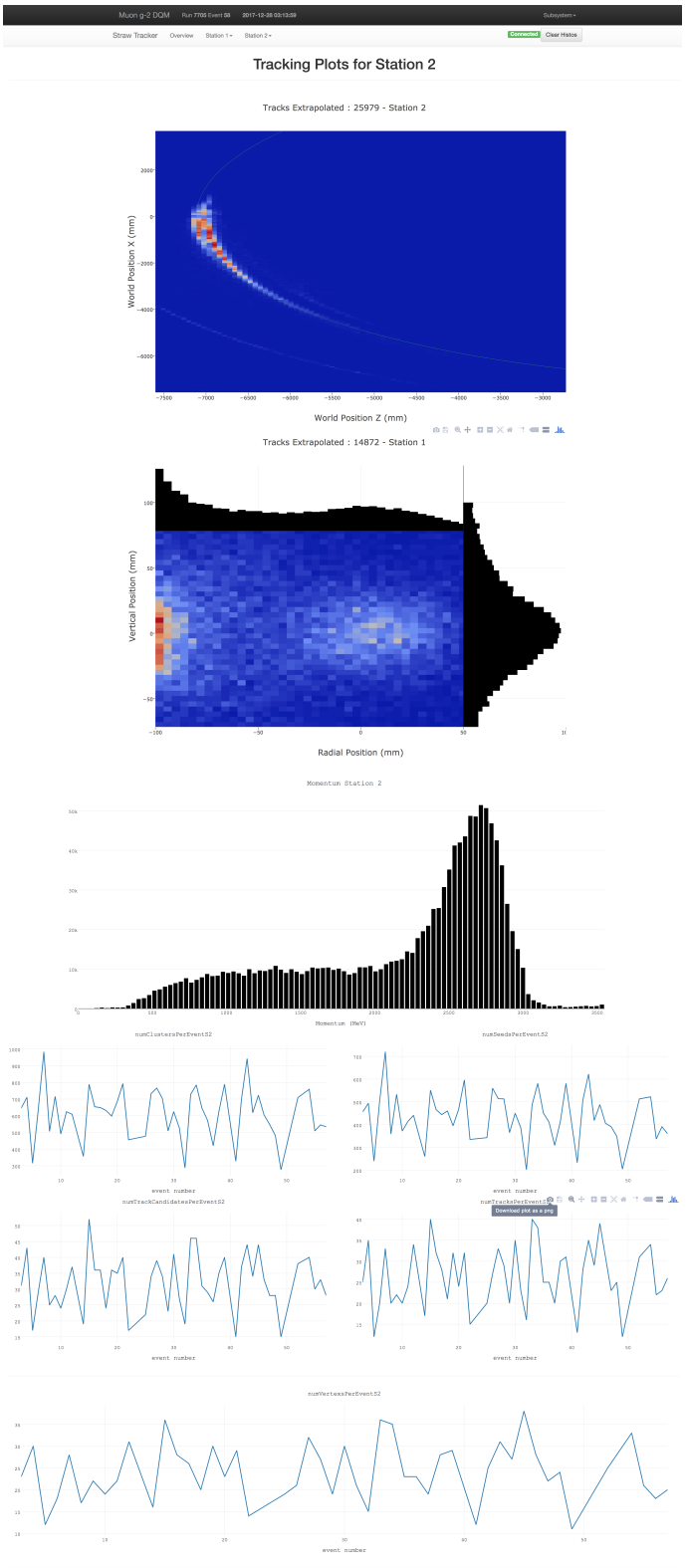

Figure 6.26: Data Quality Monitor (DQM) page showing beam related plots during running for tracking station 2. *Top:* figure showing a top down view of the extrapolated position around the ring of the decay positrons. *Second:* figure showing the extrapolated beam profile with the increase of hits at lower radius coming from tracks which hit a physical volume. *Third:* The fitted tracks momentum. *Last:* Five plots showing the number of seeds, clusters, track candidates, tracks and extrapolated tracks per fill.

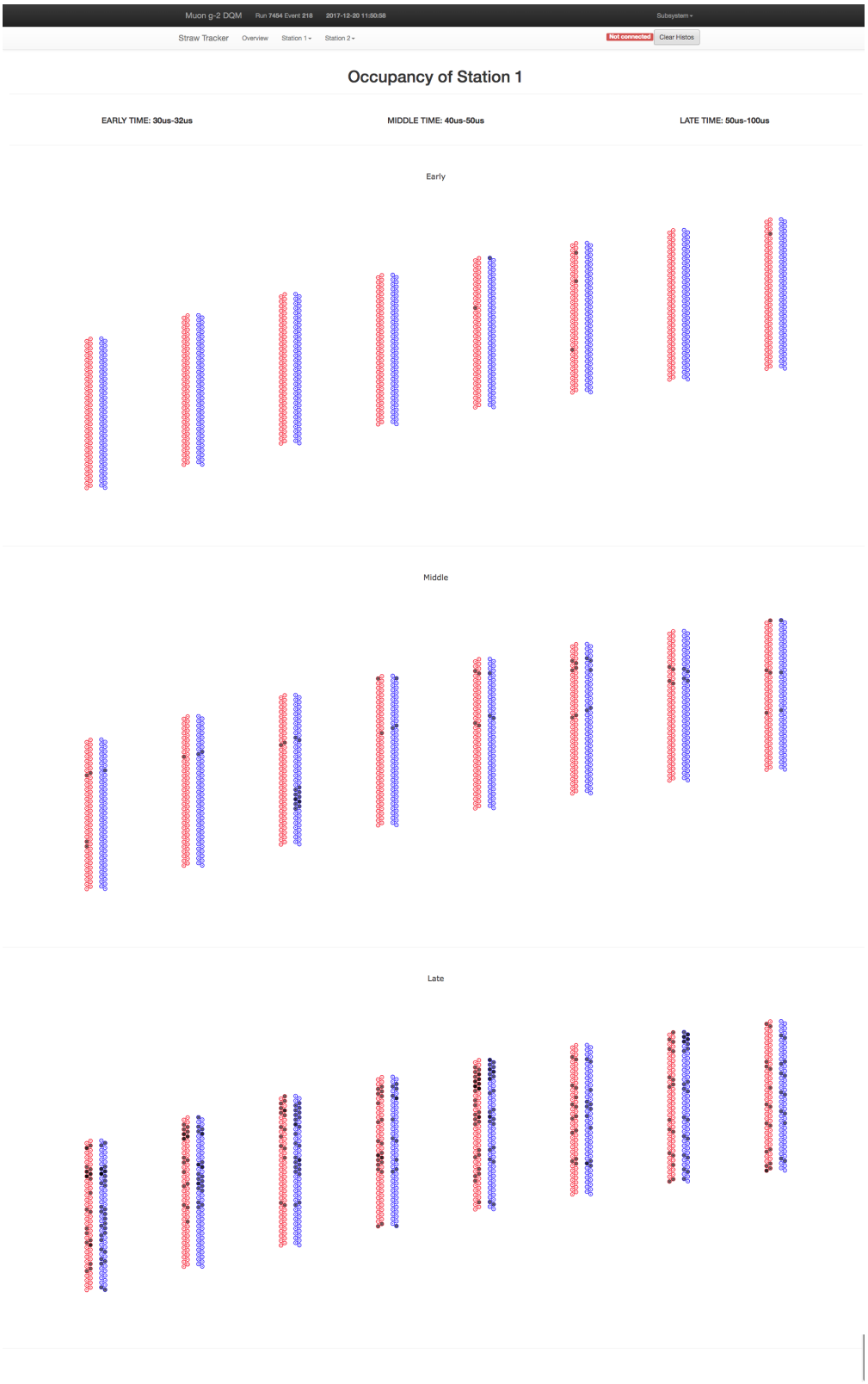

Figure 6.27: Data Quality Monitor (DQM) page showing detector system occupancy during early detector commissioning showing the proton launch when the electrostatic quadrupoles are turned off at late times.

6.6 Conclusion

This section covered the design, construction and initial testing of straw tracker modules carried out at the University of Liverpool as well as the testing, installation and commissioning at Fermi National Laboratory. Overall, 22 straw tracker modules were delivered with 16 currently installed in the storage ring, from the modules currently installed 99.7% of the channels are fully operational. The author was part of the team of three to install all of the tracker modules as well as ensuring the long term safety of the modules within the experiment. The ability to monitor and control the high voltage status of each channel was developed along with the ability to monitor the data coming from the detector system in near real-time as part of the data quality monitor. A number of tracker performance plots have been presented showing the successful operation, readout and tracking from these modules. The E989 straw tracker greatly surpasses the previous BNL straw tracker as they can start tracking at much earlier times in the fill giving higher statistics making the beam measurements and calo acceptance studies much stronger.

Chapter 7

Tracker and Calorimeter Matching

The primary physics objective of the straw tracker is to measure the stored muon beam profile but there are multiple secondary physics objectives which involve understanding and reducing the systematic uncertainties associated with the muon precession frequency measurement. This chapter will outline these secondary objectives with a focus on identifying pileup events in the calorimeter. To achieve this work the author developed the matching algorithm, the matched events association datatype, required coordinate system transformations as well as producing a number of standard plots. The standard plots are generated as part of data processing and as they are able to detect time shifts in either detector they are used as the first check to ensure that there are no problems with the data or processing.

7.1 Overview

Comparing data between the straw trackers and calorimeters requires knowledge of both the performance and limitations of both detectors. The performance of the straw trackers and calorimeters are presented in section 6.4 and 4.4.1 respectively, but key information required for making comparisons between the two detectors systems will be given here.

The 24 calorimeters positioned in the centre of the storage ring are constructed from 54 lead fluoride (PbF_2) crystals in a 6 high by 9 wide array. Each crystal is 25mm wide, 25mm tall, 140mm long ($15X_0$) and wrapped in a light tight white Millipore paper. When a positron enters a crystal it showers and produces Cerenkov radiation, this light is detected and read out by a single monolithic $12 \times 12\ mm^2$ Hamamatsu silicon photo-multiplier (SiPM) bonded onto it on the rear face [42]. The energy deposited by this positron is deposited across multiple neighbouring crystals as shown in figure 7.1. The position where a particle entered the calorimeter can be determined from the energy deposited in multiple crystals using a linear energy-weighted method, which performs well for positrons. The time given to the reconstructed cluster created is determined from the time of the highest-energy crystal within the cluster. The laser calibration system provides a calibration channel to each crystal allowing the gain of each crystal to be measured at regular intervals. Key specifications for the calorimeters in determining the energy and time-of-arrival of each decay positron include [45] :

- The time resolution, extracted from a fit of the SiPM pulse, must be better than 100 ps for positrons having energy greater than 100 MeV;
- The calorimeter must be able to reliably resolve two showers by temporal separation with time separations greater than 5 ns, and it must accurately assign correct energies to the two pulses;
- The energy resolution of the reconstructed positron energy summed over hit crystals must be better than 5% at 2 GeV;
- The maximally allowed, uncorrected, gain change is $\delta G/G < 0.04$ % over the 700 μs time period while the rate reduces by four orders of magnitude, starting with an initial rate that can exceed 1 MHz.

Straw tracking stations are installed in modified vacuum chambers directly in-front of calorimeters 13 and 19 as shown in figure 5.1 and 7.3. During the data taking period covered in this work the tracking software required a minimum of 6 planes of straws to

Figure 7.1: Figure showing the percentage energy shared between crystals when the centre crystal is hit by a normally incident positron. The calorimeter crystals not visible in this figure have no energy deposited from this positron [42].

be hit to enable a track to be passed to the fitting stage as well as having a p-value of greater than 0.005 to ensure a well fitted track.

Software was written within the *art* event-processing framework to loop over the forward extrapolated tracks and calorimeter clusters finding detector events which match in time after taking into account a global offset in time between the tracking and calorimeter systems, these will be referred to as coincident events. Figure 7.2 shows the coincident timing peaks for both systems with the time offset from zero being due to how each detector system handles their internal clocks as well as the time difference between the two distributions arising from differing cable lengths between the two tracker stations. Once a coincident event is found an association between the two data objects (track and cluster) is saved. An association within this framework is a reference between two data objects stored in an art *event* which allows many-to-many relations, i.e. one-to-one, one-to-many, many-to-one, to be saved to the art *event* and later retrieved which enables the track and calorimeter matching to be only carried out once.

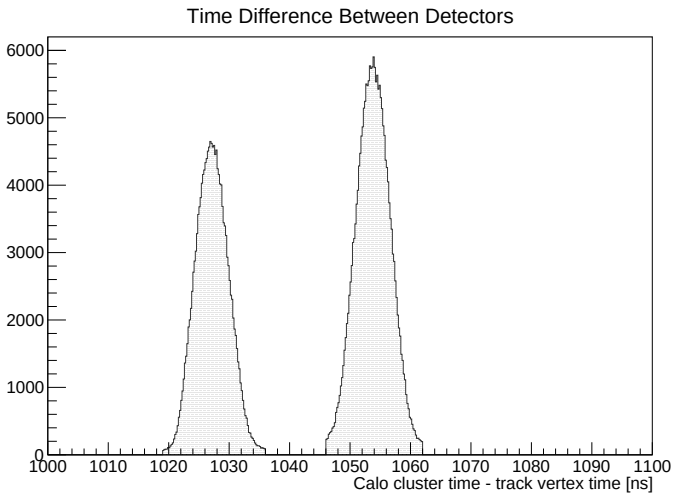

Figure 7.2: Time correlation peaks between a calorimeter cluster and straw tracker track, global offset from zero is due to how each detector system handles their internal clocks and the difference between the two peaks being due to cable length differences.

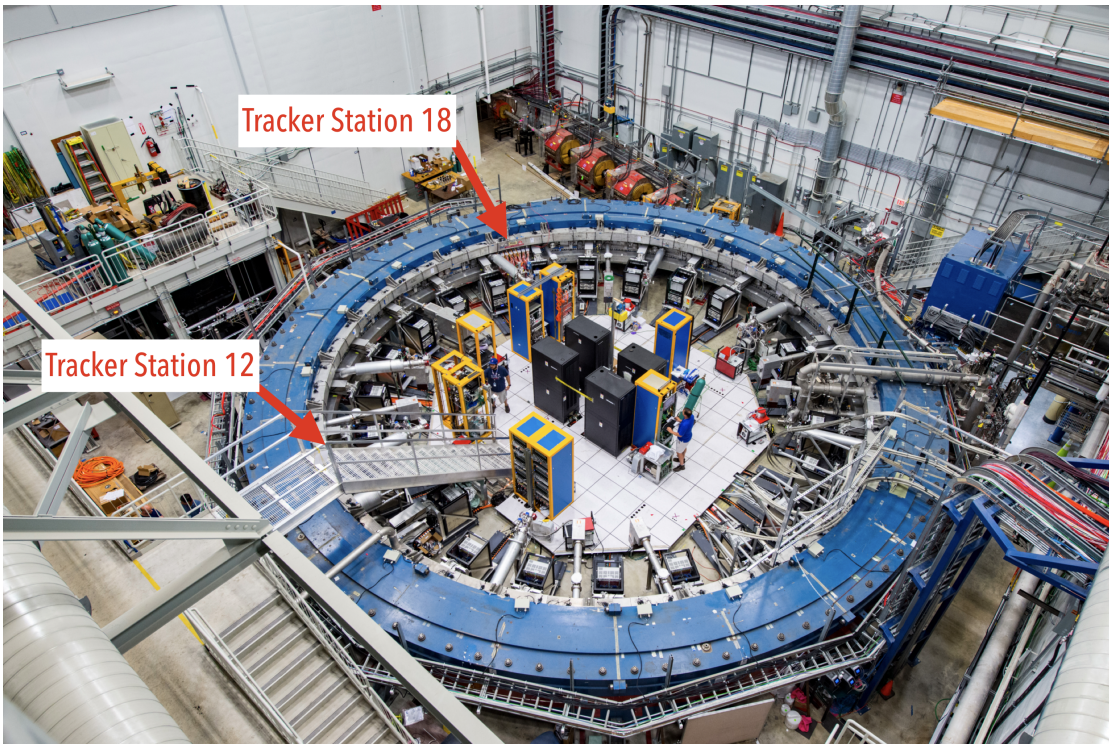

Figure 7.3: Annotated photograph of the g-2 storage ring showing the locations of the two currently installed tracker stations. *Base Image Credit: Fermilab*

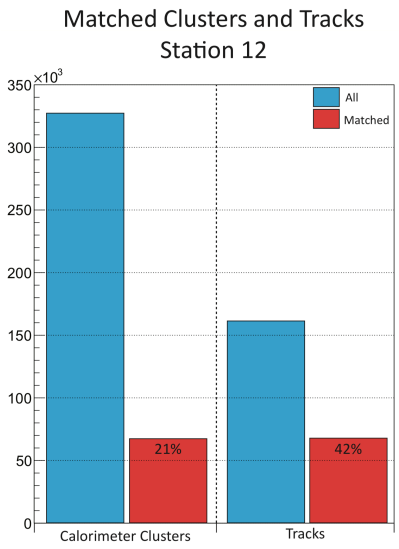

(a) Tracker Station 12

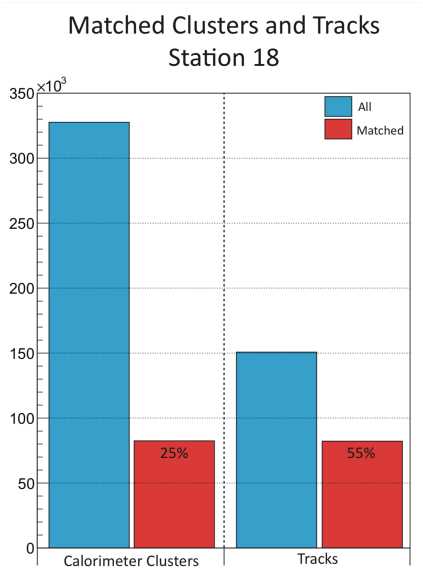

(b) Tracker Station 18

Figure 7.4: A high level overview showing the total number of calorimeter clusters and straw tracker tracks which have been recorded for each of the two tracker stations and corresponding calorimeter. In red is the fraction of clusters and tracks which are matched between the two systems with the difference between the two tracker stations coming from the azimuthal distribution of lost muons around the ring.

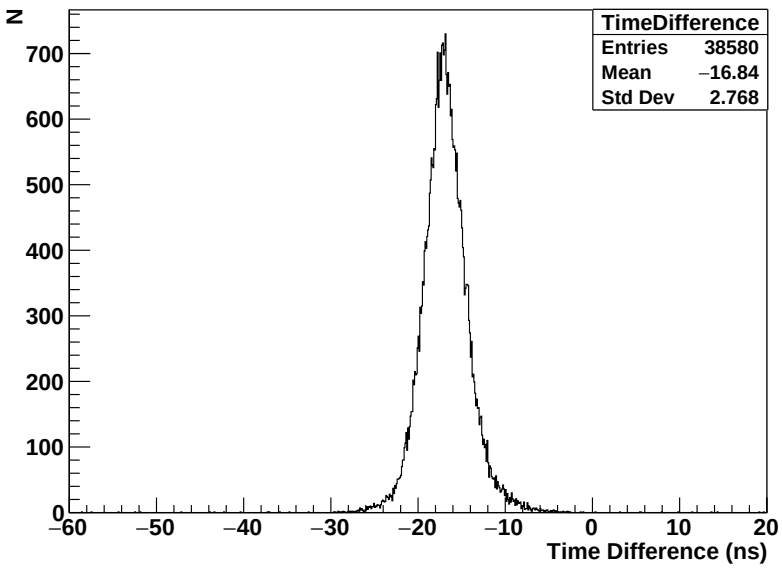

(a) Time difference between detector systems in the full g-2 simulation.

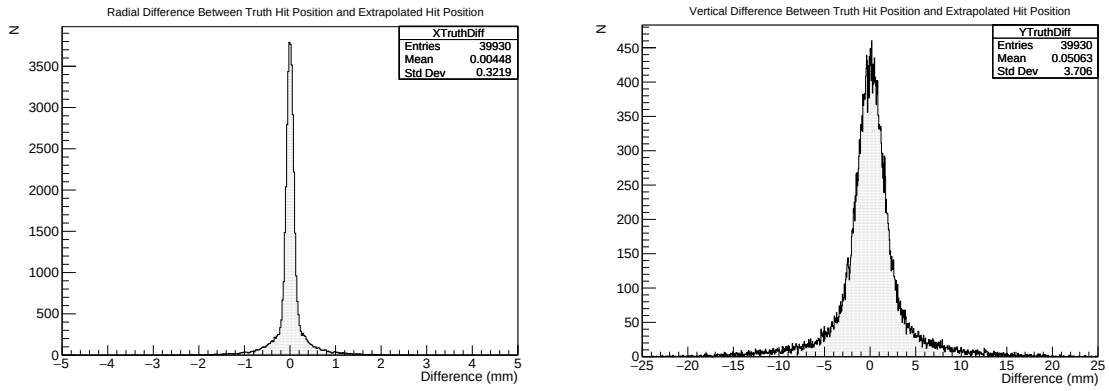

Figure 7.5: Matched extrapolated track and calorimeter cluster information for simulated data, where the time difference between the two detector systems is given *(top)*. Difference in radial *(left)* and vertical *(right)* position between simulated tracks reconstructed and extrapolated to the calorimeter face and the truth radial and vertical location of the calorimeter hit positions. This shows that the track extrapolation is working as expected with the distributions centred around 0.

7.2 Comparisons between detector systems

After matching the tracks with calorimeter clusters comparisons can be made between the two detector systems. For example the reconstructed position given from the forwards extrapolated tracks on the calorimeter face can be compared to the positions determined from the calorimeter clustering algorithm. The comparisons allow confirmation that the detectors are aligned correctly in space relative to each other; the extrapolation and clustering algorithms are working as intended and the fringe magnetic field experienced by the particle matches the field in the offline simulation and extrapolation code as well as verifying the matching code is performing as intended.

To ensure the conclusions drawn from a study comparing the position reconstruction of both systems are accurate, a simulation was carried out where positrons are produced around the ring with realistic parameters and stepped through the magnetic field. The data gained from this simulation was passed through the offline track reconstruction, forwards track extrapolation and then compared to the *truth* calorimeter hit position. This not only shows the correctness of the tracking and extrapolation code but also shows the accuracy of the forwards extrapolated position. Figure 7.5 gives the difference between these two positions in radial (x) and vertical (y) in the global coordinate system as well as the time offset between the coincident data shown in figure 7.5a. This shows the distributions centred around 0 with narrow widths verifying the tracking and forwards extrapolation code.

Comparing the forwards extrapolated track position to the reconstructed calorimeter cluster position allows us to infer information about how the shower propagates through the calorimeter crystals. If the positron is incident at an angle to the calorimeter face then the shower will deposit energy in multiple crystals pulling the reconstructed position away from the initial entry position. Figure 7.6 shows the radial (x) and vertical (y) differences between these reconstructed positions for simulated data and figure 7.7 shows these differences verses entry angle.

Figures 7.8 and figure 7.9 show the same results for data and overall show similar behaviour to the comparisons made from simulated data. However a vertical offset

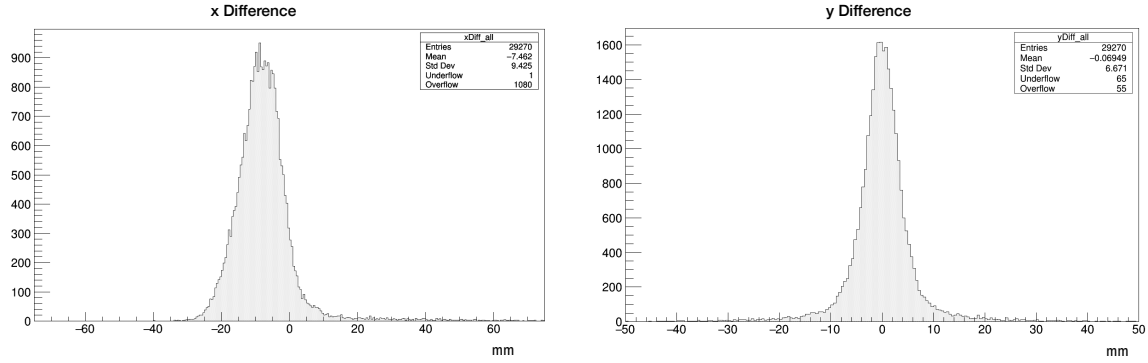

Figure 7.6: x and y difference between the matched extrapolated track position on the calorimeter face and the reconstructed calorimeter cluster location for data gained from simulation.

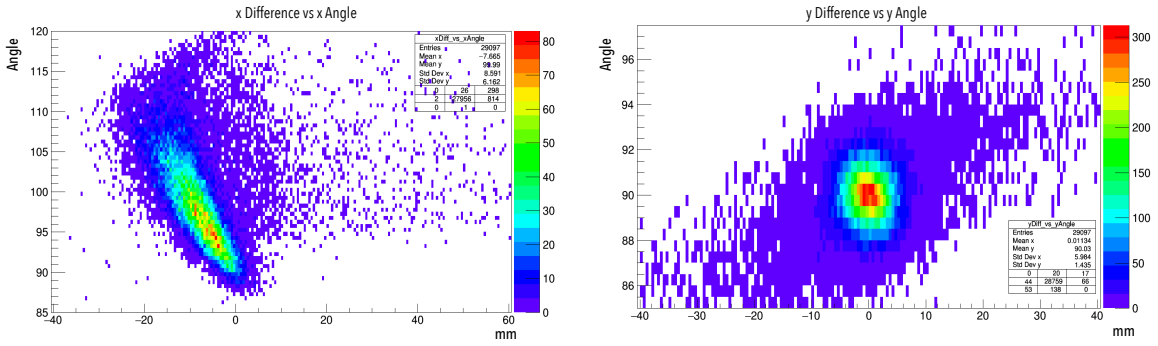

Figure 7.7: x and y difference between the matched extrapolated track position on the calorimeter face and the reconstructed calorimeter cluster location versus angle of entry for data gained from simulation.

between the calorimeter cluster location and the forward extrapolated track position on the calorimeter face of 2.06 mm for calorimeter number 13 and 2.80 mm for calorimeter number 19 is observed. These offsets were first detected from this study and are thought to be an issue in the vertical alignment of the calorimeters. This will be corrected for during offline data processing and will be fully addressed in future alignment processes.

When comparing the two detector systems it becomes possible to distinguish the decay positrons from minimally ionising particles, such as muons, as they would both be recorded with similar momenta but different deposited energies. Plotting the momentum of the track against the energy of the cluster shows these two distributions as shown in figure 7.10. This was the first example of particle identification at the

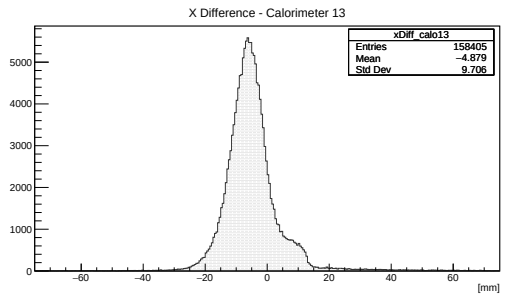

(a) Calorimeter 13 x difference

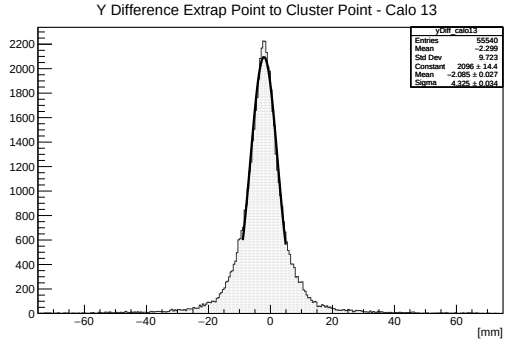

(b) Calorimeter 13 y difference

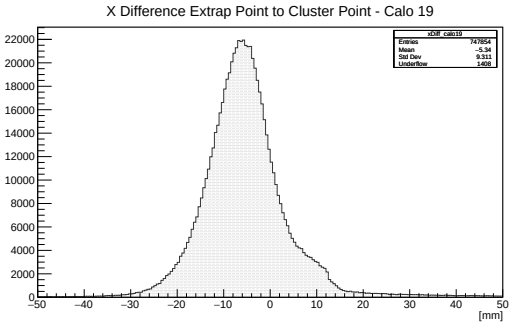

(c) Calorimeter 19 x difference

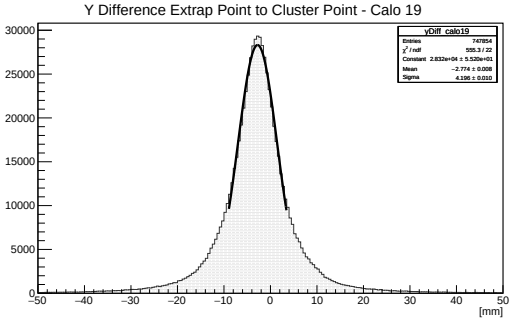

(d) Calorimeter 19 y difference

Figure 7.8: Radial (x) and vertical (y) differences between the positions of a matched tracks extrapolated to the calorimeter face and the reconstructed calorimeter cluster position from data for calorimeter number 13 (*7.8a, 7.8b*) and 19 (*7.8c, 7.8d*).

experiment, and demonstrates the power of matching data from multiple detectors. This method was unavailable at the BNL experiment as they did not have a working matching algorithm, and when higher statistics are available will be a crucial tool in reducing the systematic uncertainties.

7.2.1 Calorimeter efficiency

Using the straw tracker data it is possible to measure the efficiency of the calorimeters directly behind each tracker station. The method used to do this is to look over all of the tracks recorded and check to see if there is a time correlated calorimeter cluster in the calorimeter of interest. The forwards extrapolated position on the calorimeter face is recorded in two different histograms, one for each case, if there is a match and

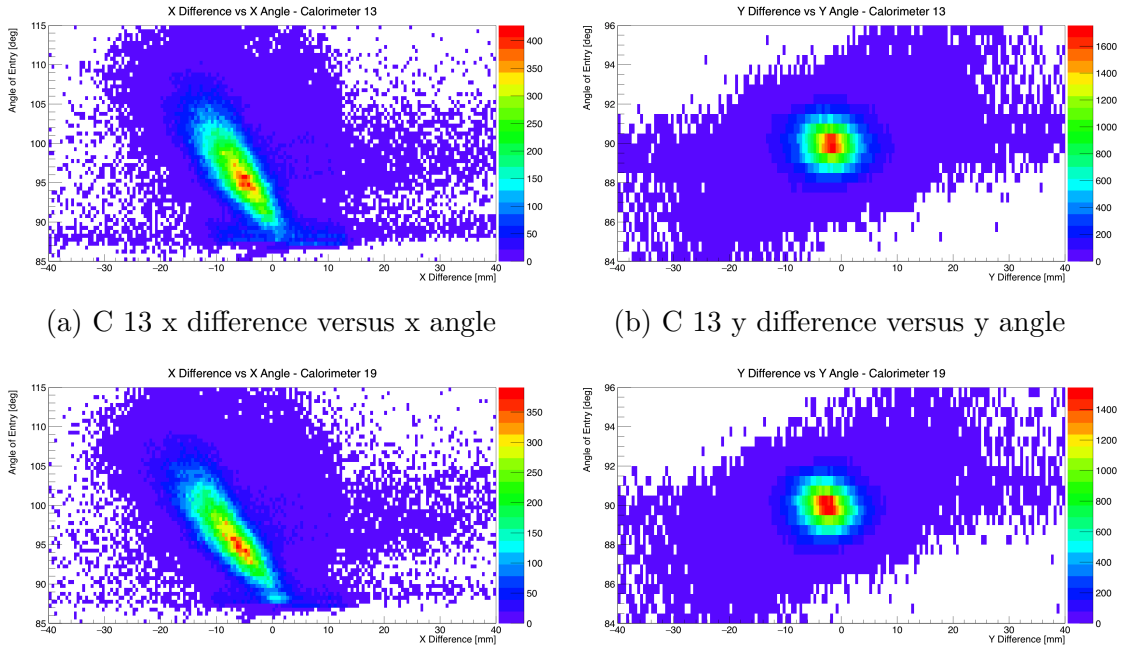

(a) C 13 x difference versus x angle

(b) C 13 y difference versus y angle

(c) C 19 x difference versus x angle

(d) C 19 Y difference versus Y angle

Figure 7.9: Radial (x) and vertical (y) differences between the positions of a matched tracks extrapolated to the calorimeter face and the reconstructed calorimeter cluster position from data versus particles angle of incidence for calorimeter number 13 (*Top*) and 19 (*Bottom*).

if there is not a match. Figure 7.12 shows all (matched and unmatched) forwards extrapolated positions for both tracker locations with the calorimeter crystals overlaid on the histograms, the muon storage region is on the right hand side of each of the plots. It is then possible using the two histograms produced to directly compare the unmatched extrapolated positions with the histogram of all of the extrapolated positions, shown in figures 7.13 and 7.14. These plots both show a number of interesting effects, primarily that there are calorimeter reconstruction inefficiencies at the crystal boundaries, which are to be expected, and that these inefficiencies change across the calorimeter face. This is thought to be due to particles hitting closer to the storage region having less curvature compared to those which hit the calorimeter further away and so have less chance to shower into a crystal if the boundary is hit. This study also detected a crystal in calorimeter number 19 which is less efficient than surrounding crystals. This was later verified by the laser calibration group, and crucial in giving

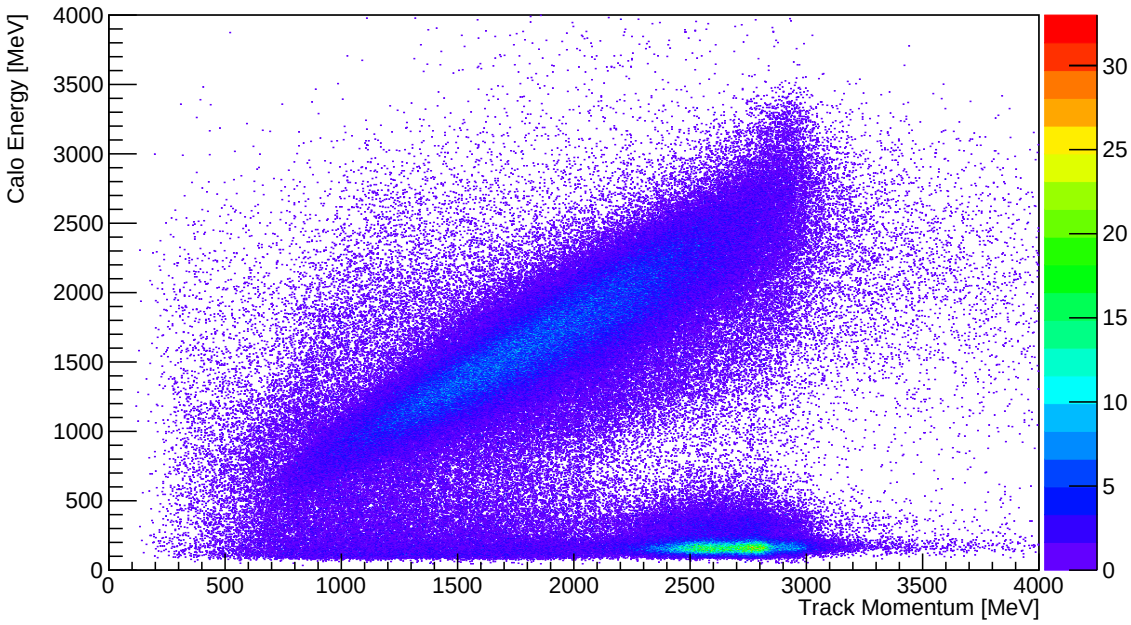

Figure 7.10: Tracker recorded momentum versus calorimeter cluster energy for experimental data showing the band of positrons where calorimeter energy is equal to track momentum and the distribution at high momentum and low energy coming from lost muons.

the collaboration confidence in the laser calibrations ability to identify the inefficient crystals, as well as demonstrating the need for the tracker and calorimeter matching algorithm.

Calorimeter Number	Total Number of Tracks	Total Number of Tracks Matched	Percentage Matched
13	3,892,381	3,581,990	92%
19	2,781,626	2,633,000	94%

Figure 7.11: Calculating the overall efficiencies of the two calorimeters behind the tracker stations using the total number of tracks extrapolated to the calorimeter face and the total number of tracks extrapolated to the calorimeter face which match to a calorimeter cluster.

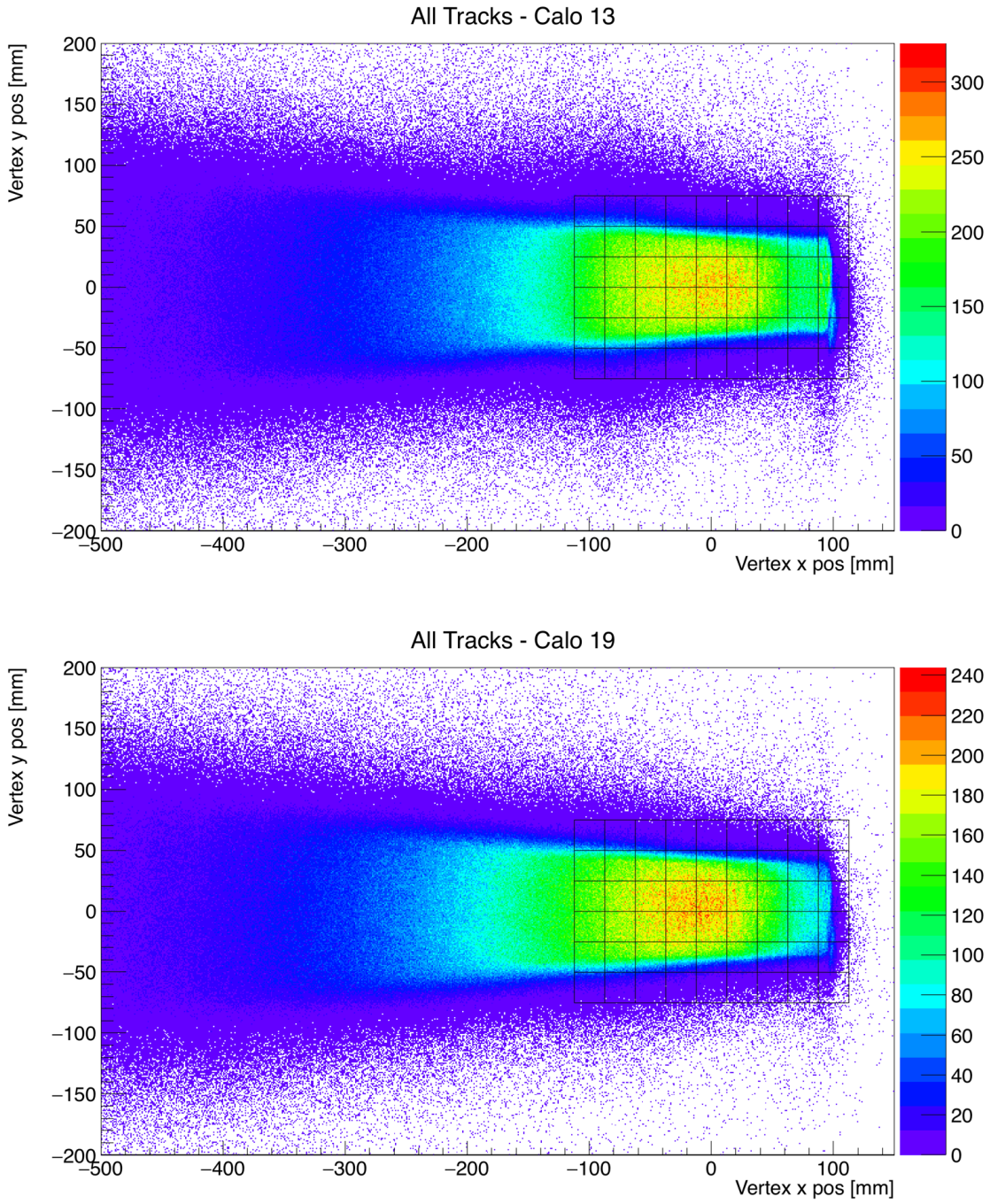

Figure 7.12: The radial (x) and vertical (y) position of all tracks extrapolated forwards to the calorimeter face (extrapolated track vertex). *Top:* Tracker Station 12. *Bottom:* Tracker Station 18. Where the z-axis colour denotes the number of entries in each bin.

Calorimeter MIP efficiency

Using the same method as outlined in the calorimeter efficiency study it is also possible to determine the efficiency of the calorimeter to reconstruct minimal ionising particles

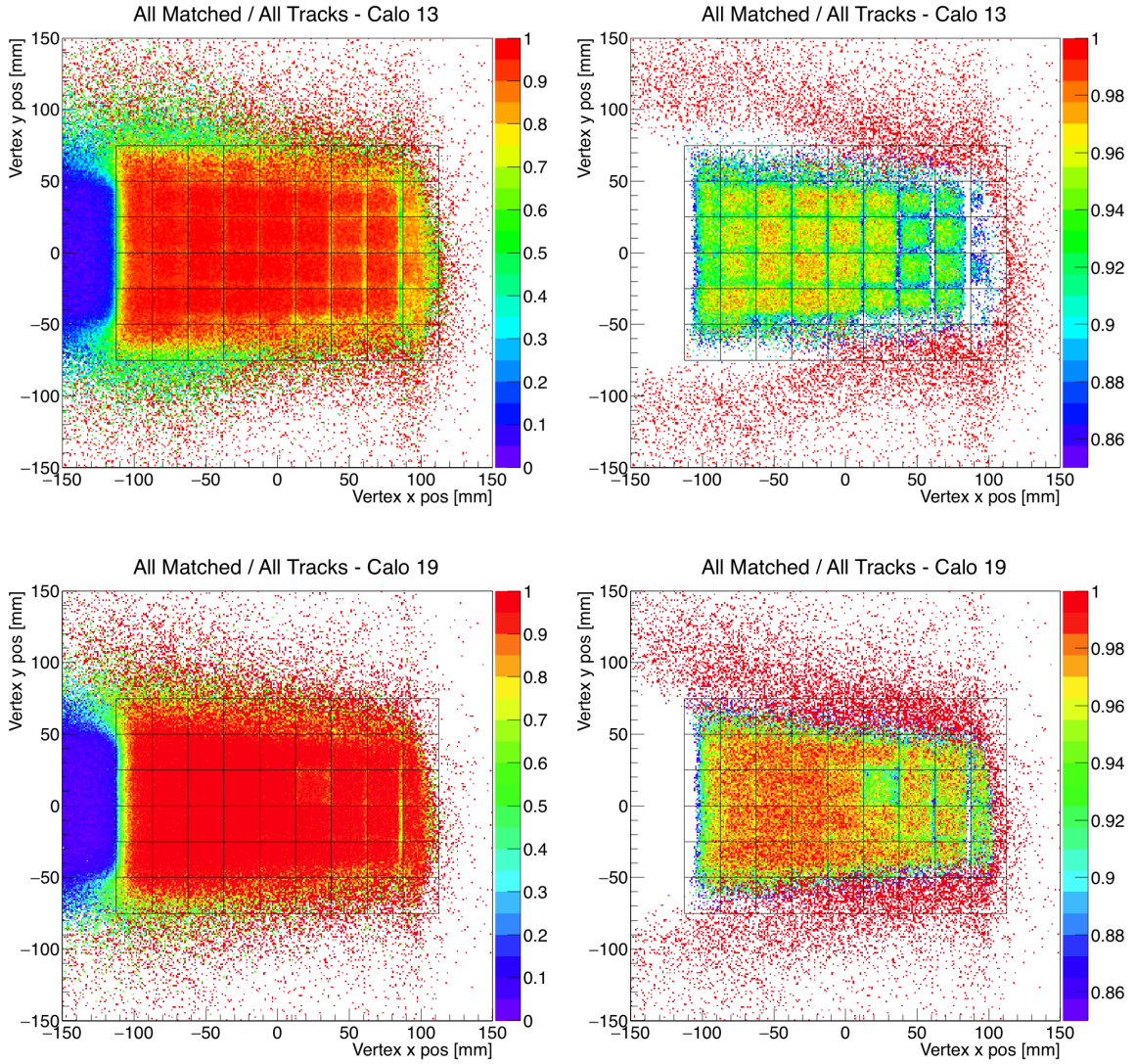

Figure 7.13: Matched track position (radially (x) and vertically (y)) over all tracks for *Top:* Calorimeter 13 and *Bottom:* Calorimeter 19. *Right Column:* Z-axis range changed to highlight the small efficiency changes. Here the inefficient crystal is clearly visible in Calorimeter 19 as the 7th row from the left, 3rd column down.

(MIP) using the straw trackers. This is an important independent cross check required for the muon loss algorithm and will ensure there is no bias or underestimation in their measurement. To be able to do this it is important to visualise the location of the straw tracker modules within the staircase vacuum chamber, as shown in figure 5.1 and 5.4, the first straw tracker module is positioned directly behind part of the vacuum chamber wall. It is highly unlikely that the straws in the 'shadow' of the vacuum

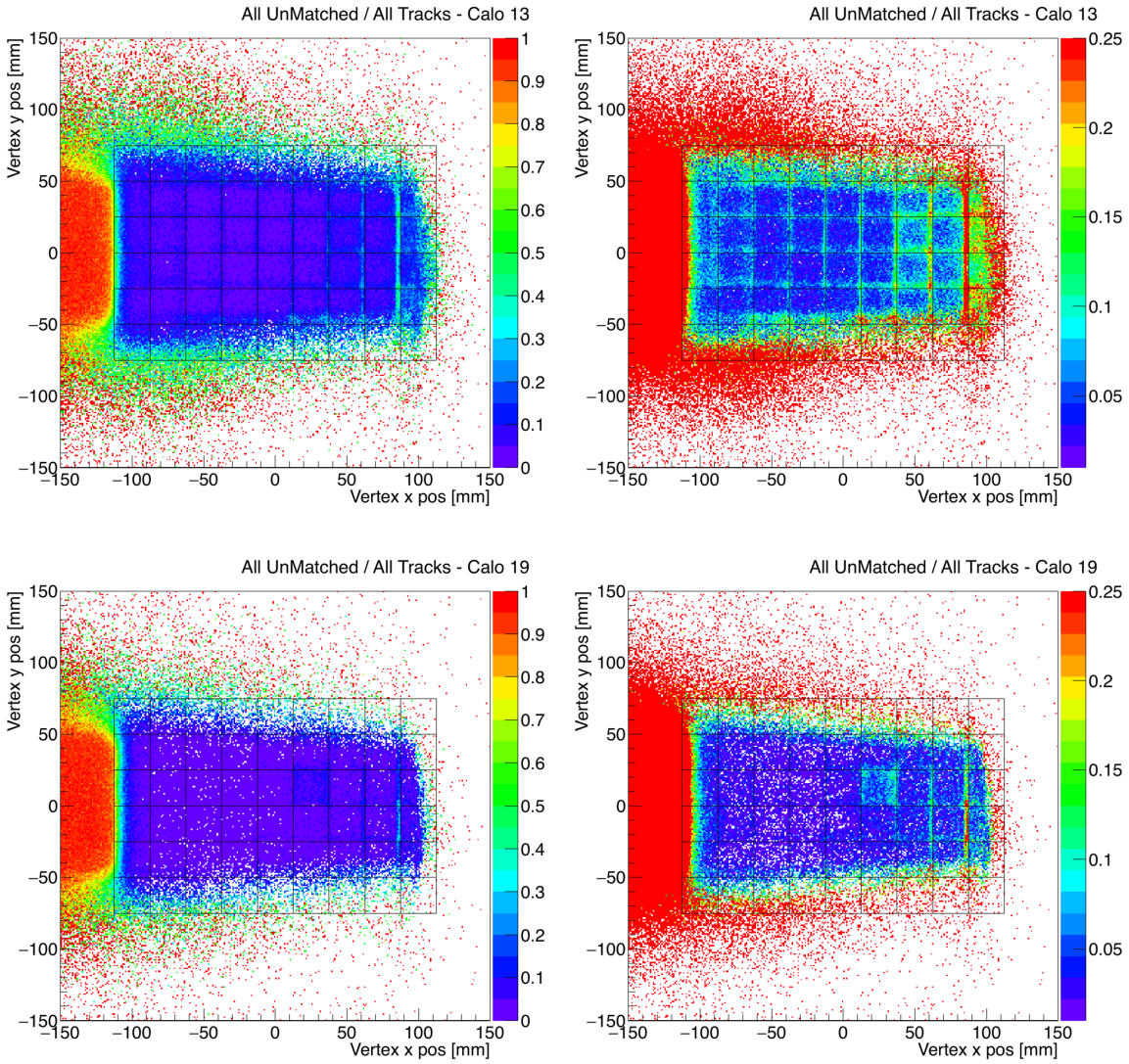

Figure 7.14: Unmatched track position (radially (x) and vertically (y)) over all tracks *Top:* Calorimeter 13 and *Bottom:* Calorimeter 19. *Right Column:* Z-axis range changed to highlight the small efficiency changes.

chamber wall will reconstruct any positrons that would travel on to hit the calorimeter as there is a large amount of aluminium in its path. It is clear that any particle originating from this location which creates a track through the tracking station and is successfully extrapolated forwards to the calorimeter face could not be a positron from the storage ring. Given this information, tracks which match this criteria - originating from these shadowed straws as well as extrapolating forwards to the calorimeter face

- are tagged as lost muons. The time at which the track would hit the calorimeter face is determined and a calorimeter cluster in a coincidence time window is searched for. This procedure can be carried out for each tracker station. Figure 7.15 shows the forwards extrapolated position of all tracks (matched and unmatched) tagged as lost muons on the calorimeter face while figure 7.16 gives the forward extrapolated position on the calorimeter face for lost muon tagged tracks which were not matched with a calorimeter cluster. The tracks which do not lie in the region of the calorimeter are due to random coincident background events in the time window of the matching algorithm. As the track-finding algorithm is improved and the t_0 of the track is updated this background is expected to become negligible, which will in turn improve the efficiency estimate.

Using this method and placing a cut to ensure the forwards extrapolated tracks hit the calorimeter face allows the total efficiency for reconstructing MIPs to be determined. For calorimeter number 13 it was found that 92 % of lost muons were matched to a reconstructed calorimeter cluster and 94 % were matched for calorimeter 19. The uncertainties on the percentage efficiencies quoted is estimated to be $\sim \pm 2\%$ coming from the fact that the tracking algorithms are still in their infancy so there could be a number of tracks which do not hit the calorimeter face that we are including in these numbers, biasing the results. A more detailed study will be carried out once both the tracking and calorimeter reconstruction algorithms are improved.

These efficiencies can be cross-checked with the Lost Muon analysis which will look at low energy calorimeter coincidences between a certain calorimeter, n, and the calorimeter two further around the ring, $n+2$, to determine the efficiency of the calorimeter between these two, $n+1$. This method only measures the global calorimeter efficiency and provides little information about crystal to crystal efficiencies.

Calorimeter Number	Total Number of Tracks Tagged as LMs	Total Number of LMs Tagged Tracks Matched	Percentage Matched
13	856,396	741,249	86 %
19	222,724	204,046	91 %

Table 7.1: Calculating the efficiencies of the two calorimeters behind the tracker stations for reconstructing MIPs using the total number of LM tagged tracks extrapolated to the calorimeter face and the total number of LM tagged tracks extrapolated to the calorimeter face which match to a calorimeter cluster.

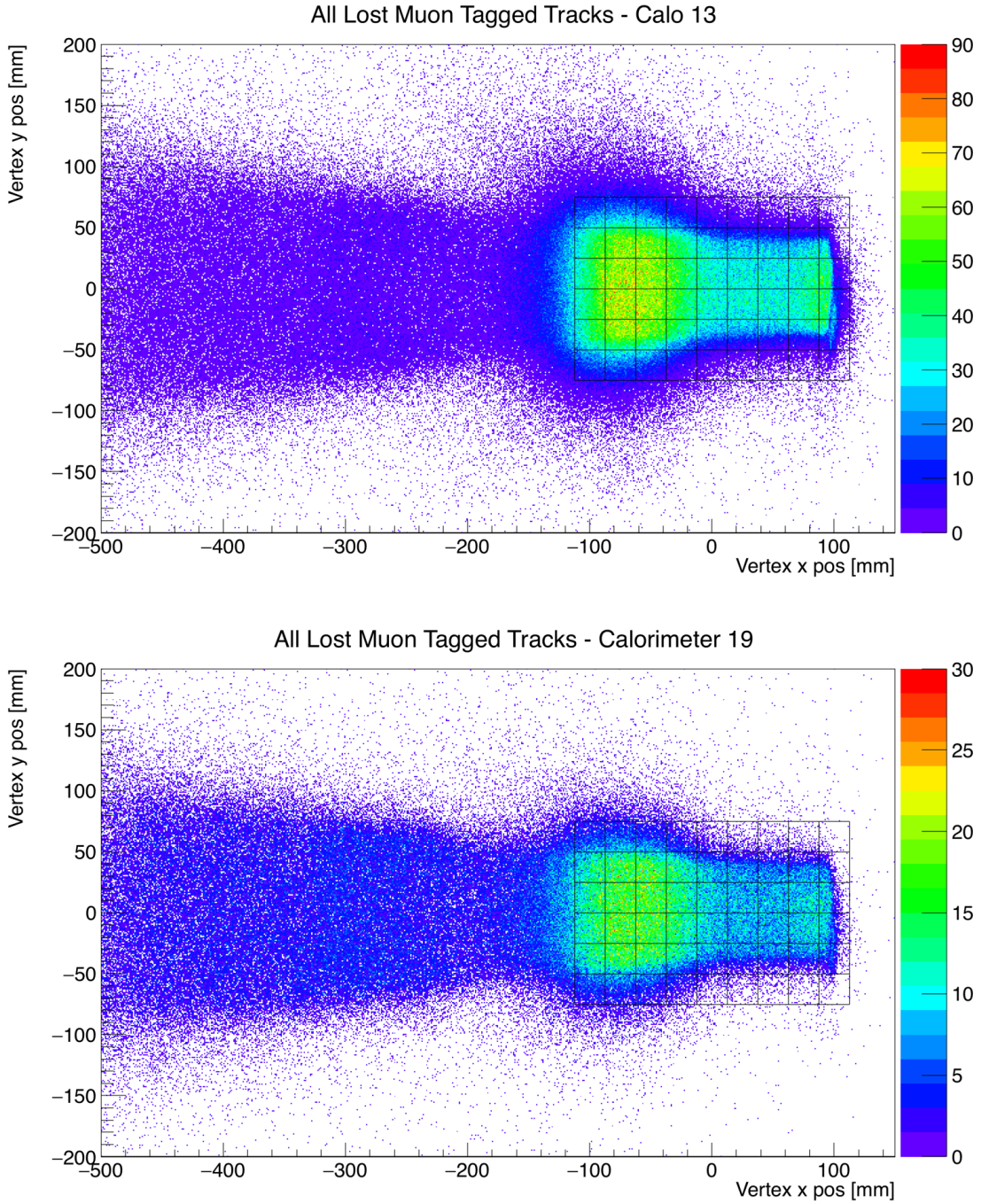

Figure 7.15: Radial (x) and vertical (y) position of Lost Muon tagged tracks extrapolated forwards to the calorimeter face (extrapolated track vertex). *Top:* Tracker Station 12. *Bottom:* Tracker Station 18. Where the z-axis colour denotes the number of entries in each bin.

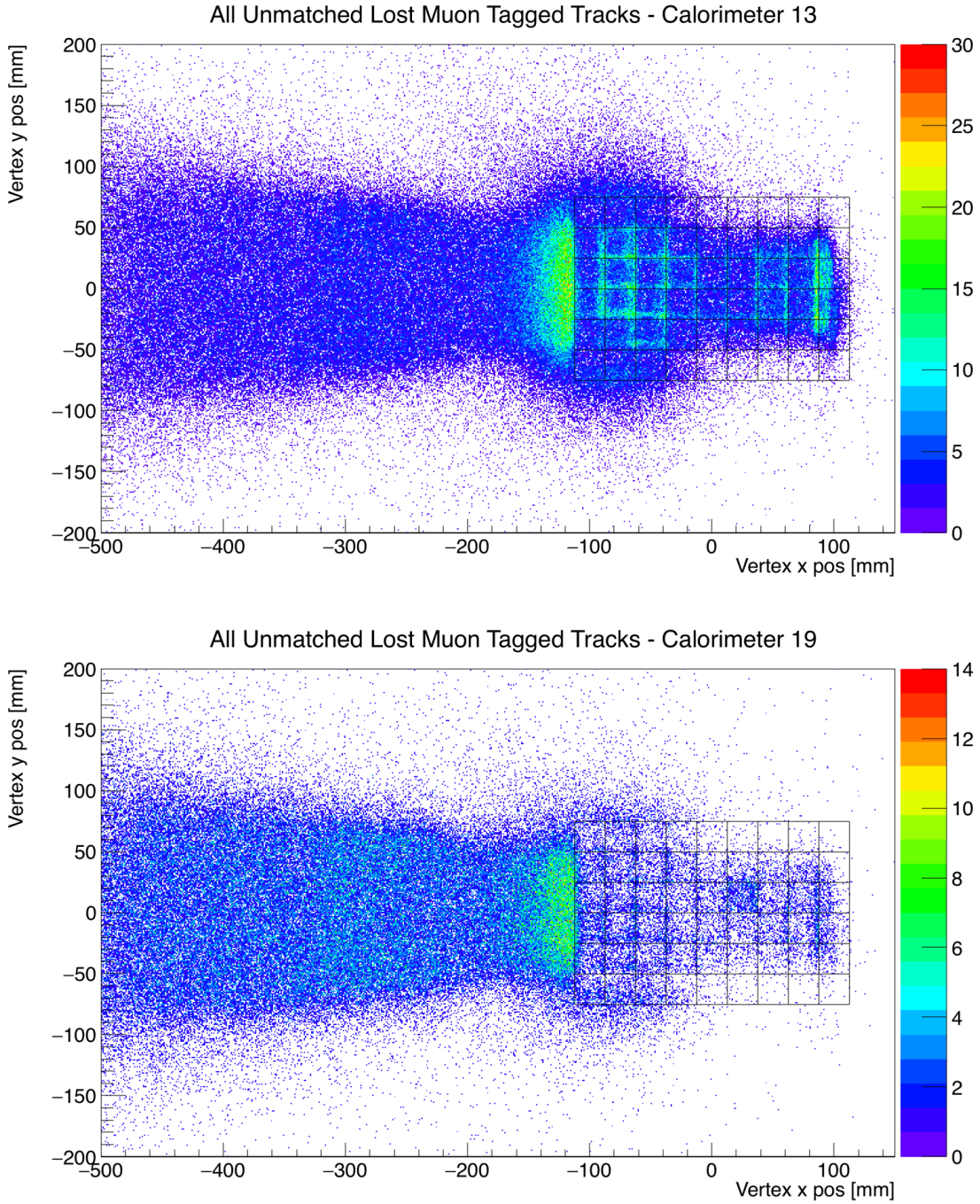

Figure 7.16: Radial (x) and vertical (y) position of Lost Muon tagged tracks extrapolated forwards to the calorimeter face (extrapolated track vertex) which do not match with a calorimeter cluster. *Top:* Tracker Station 12. *Bottom:* Tracker Station 18. Where the z-axis colour denotes the number of entries in each bin.

7.3 Pileup

Pileup occurs when two (or more) particles enter the calorimeter within the pulse reconstruction algorithms time resolution and is therefore counted as a single pulse with the combined deposited energy. This can add events to the time and energy spectra by having two pulses below the energy threshold adding up to a single pulse above the energy threshold. The effect of two decay positrons being reconstructed into one pulse is visible when analysing the overall calorimeter energy spectrum, events with energies up to 6 GeV are recorded while the injected beam energy is less than 3.2 GeV. Since pileup is rate dependent and since there are more decay positrons detected at the peak of the g-2 cycle than at bottom of the g-2 cycle, the number of pileup events oscillates at the g-2 frequency, making it a very important systematic uncertainty. In addition, when considering two low energy positrons entering the detector, the phase of the resulting pileup g-2 oscillation will differ from the pure g-2 oscillation coming from single events as the phase depends on the positron energy, therefore the two low energy positrons would have a different phase to the measured high energy positron. Consequently pileup events affect the decay positron time and energy spectra by introducing a background term with its own asymmetry and g-2 phase. This background term arising due to pileup causes a time-dependent, oscillating fit value of ω_a, referred to as 'phase-pulling'.

7.3.1 Pileup at E821

The E821 collaboration were able to identify individual pulses separated by more than 5ns with a 99.994% percent reliability. Events which came within a 5ns time window of each other were accounted for *on average* by subtracting an artificially constructed pileup time spectrum from the main time spectra. This approach is based on the assumption that the probability of two pulses overlapping is the same as the probability of two pulses being separated by a small time window, between $5ns$ and $10ns$. This pileup time spectrum is constructed by looking at pulses that follow an initial "trigger"

pulse, called "shadow pulses". If this shadow pulse occurs within a certain time window from the trigger pulse then the two pulses times and energies are used to construct a pileup pulse. The constructed energy and time spectra are then subtracted from the main spectra prior to carrying out the fit for ω_a. The systematic uncertainty on the ω_a measurement due to pileup was 0.08 ppm during E821. [12]

7.3.2 Pileup at E989

The improvements made for E989 aim to reduce this 0.08ppm systematic error due to pileup to 0.04ppm. These improvements include using segmented calorimeters with fast Cherenkov light, with the ability to record low-energy events as well as achieving higher statistics and as outlined previously there are straw tracker stations positioned in front of two calorimeters in the ring. The straw trackers are able to identify time windows in which there are two tracks entering the calorimeter for which there is only a single calorimeter cluster reconstructed. This information can be used to provide verification of the old BNL method or to build up a tracker-only pileup time spectra for subtraction from the main spectra with estimates being made for the calorimeters not behind a tracking station.

Straw tracker measured pileup

Using the information obtained from the straw tracker stations it is possible to isolate narrow time windows in which there are two fitted tracks that both extrapolate to the calorimeter face and which only match to a single reconstructed calorimeter cluster. Examples of these kind of coincidences are given in figure 7.17. Analysis of these pileup events shows that their composition are different to the previously mentioned $e^+ + e^+$ events where the energy of these calorimeter clusters extends beyond 3.2 GeV up to twice the beam energy and that the calorimeter cluster energy is roughly equal to the sum of the pileup event track momenta. This is not the case, as shown in figure 7.18 and 7.19, the calorimeter cluster energy for these events shows a large distribution below 500 MeV, consistent with two muons tracked to one cluster, as well as many of

the events being between 1.8 and 3.2 GeV, consistent with either one positron and one muon both tracked to one calorimeter cluster or two lower energy positrons tracked to one cluster. This is clearly seen when looking at total track momentum versus cluster energy figure in figure 7.19.

Plotting the cluster time for all events above 1.8 GeV as well as the cluster time for the detected pileup events above the same threshold, figure 7.20a and 7.20b, shows the pileup rate clearly varying with the g-2 frequency as well as varying with the fast rotation frequency when plotted with 25 ns binning, as shown in figure 7.21. Also plotted in these figures is the measured percentage pileup for each tracking station. The difference in pileup amounts between the two stations can be explained by the variation in the azimuthal muon losses arising from a mix of the underlying muon loss mechanisms and the placement of collimators in the ring. The azimuthal distribution of lost muons is shown in figure 7.22 [51]. This difference in pileup percentages being correlated with lost muon azimuthal distribution is further evidence of the detected pileup events being between a positron and a muon. It is worth noting that a muon travelling through a calorimeter deposits around 250 MeV which could raise a lower than threshold positron above the threshold and this give an erroneous entry in the energy time spectrum ('wiggle plot'). This effect can be thought of as a varying increased SiPM gain, section 7.4 covers a study into this effect.

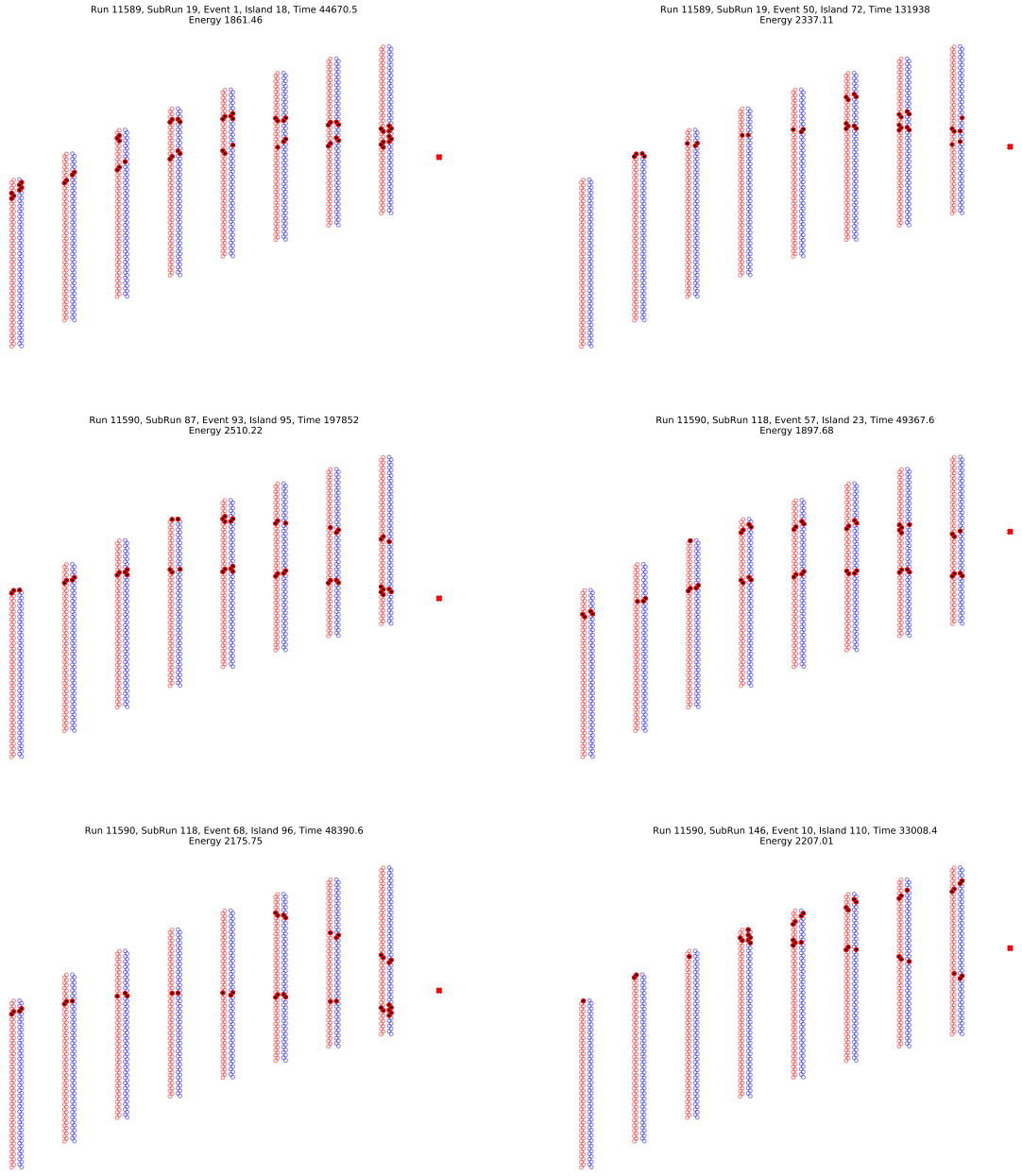

Figure 7.17: Event displays showing detected pileup events with the blue and red circles representing the straw tracker straws, with the solid red circles being the straws which were hit and reconstructed into a track and the red cross on the right hand side of each figure being the position of the calorimeter cluster on the calorimeter face without the calorimeter being displayed. Information about the time island time and calorimeter cluster energy is displayed as a title to each event.

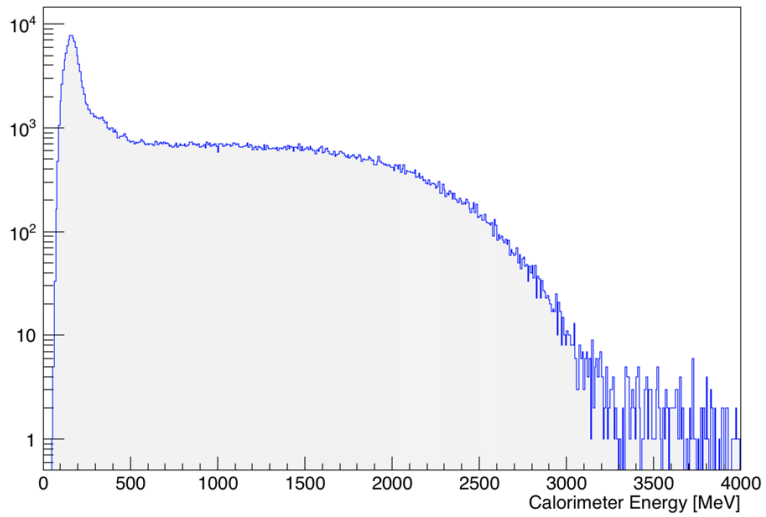

Figure 7.18: Calorimeter energy for all detected pileup events.

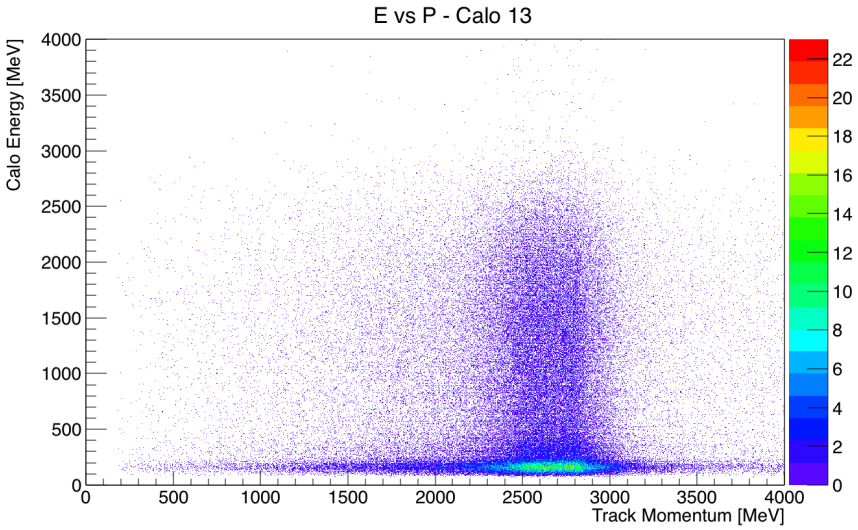

Figure 7.19: Calorimeter energy versus track momentum plotted individually for all detected pileup events. Showing a clear band of $\mu^+ + \mu^+$ events at low calorimeter cluster energy as well as a vertical band of either $e^+ + e^+$ events or $e^+ + \mu^+$ events.

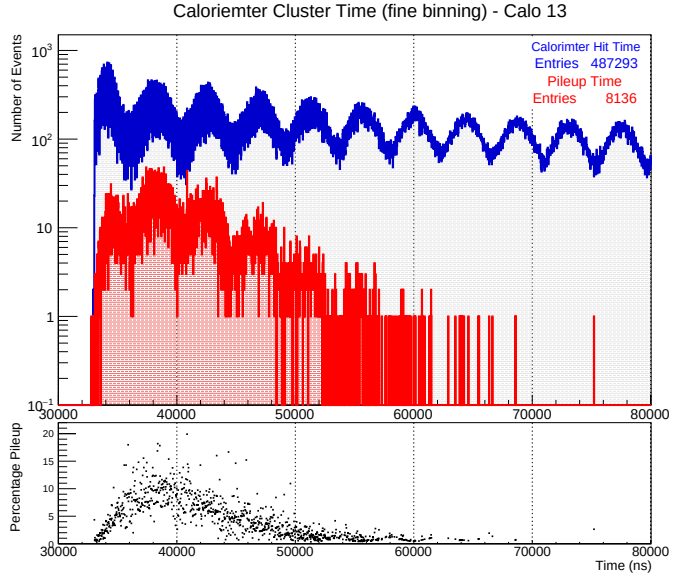

(a) Pileup time distribution for calorimeter 13

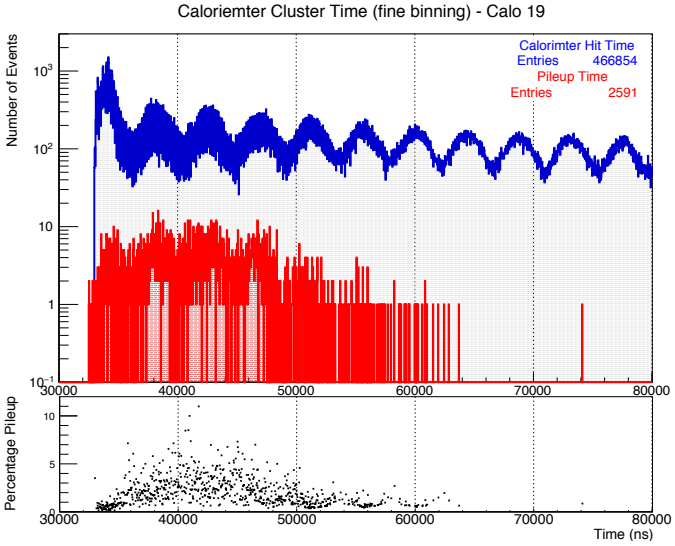

(b) Pileup time distribution for calorimeter 19

Figure 7.20: Measured pileup time distribution in red with the calorimeter clusters time distribution for this calorimeter in blue for both calorimeter 13 (*Top*) and calorimeter 19 (*Bottom*). The oscillations visible are at the ω_a frequency. In the bottom pane of each figure is the pileup percentage per time bin of 25 ns.

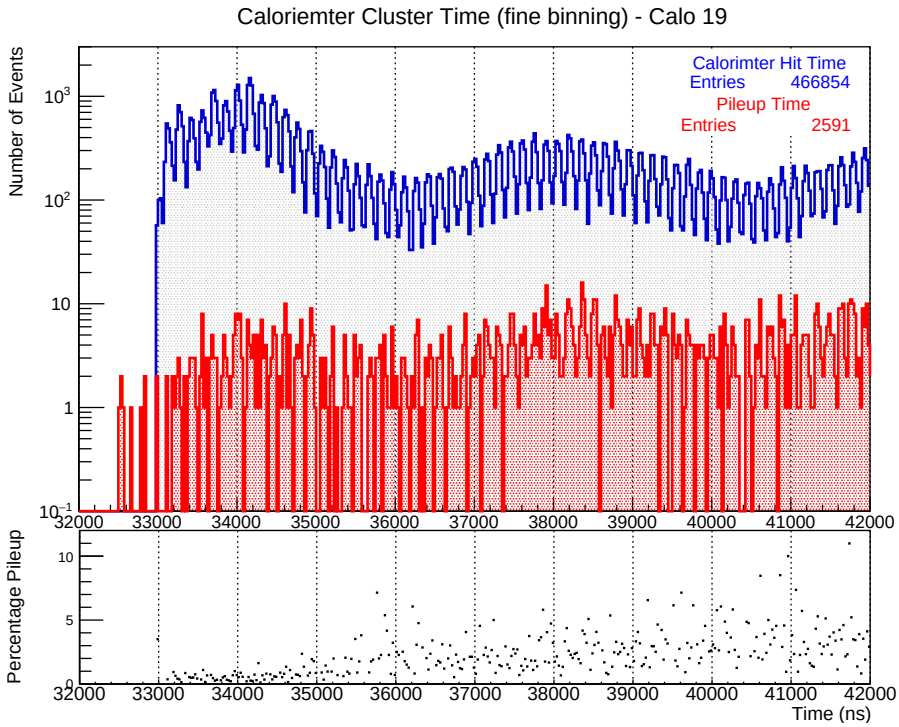

Figure 7.21: Tracker measured pileup time distribution (in blue) zoomed in between 32 μs and 42 μs showing that both the calorimeter clusters time distribution (in red) and tracker measured pileup time distribution oscillating with the fast rotation signal.

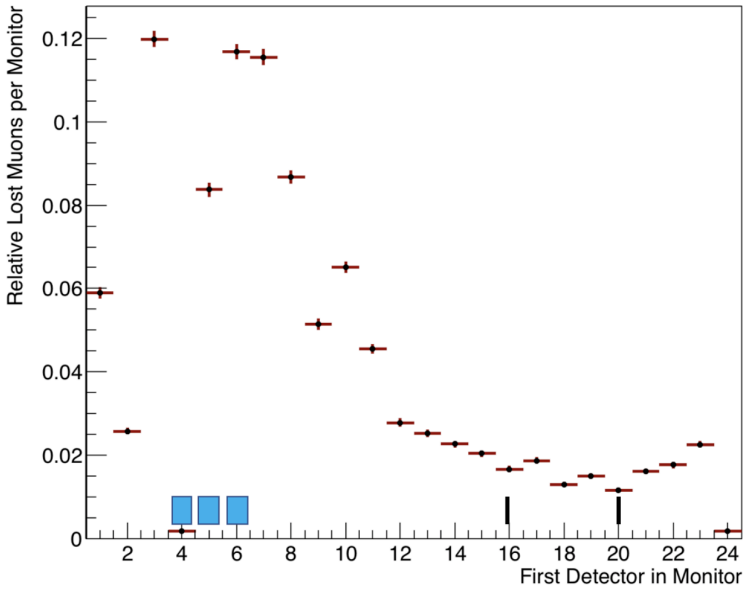

Figure 7.22: Preliminary results showing the azimuthal distribution of lost muons observed from two-fold calorimeter coincidence around the storage ring. Where a 'monitor' corresponds to the first calorimeter in the two calorimeter coincidence search. The black lines show the locations of the collimators, and the cyan bars show the location of the kicker plates. The straw tracker stations are located at monitor 13 and 19 in this figure [51].

7.4 Effect pileup has on ω_a

As mentioned previously, pileup events detected using the straw tracking stations have been identified to be predominantly arising from positron muon events or muon muon events which hit the calorimeter in a narrow time window and are therefore reconstructed as a single deposit. This effect can be modelled as a time varying gain increase which could alter the fit of the wiggle plot biasing the measured ω_a frequency by raising below threshold deposits above the energy threshold as well as introducing an early to late systematic. To establish the connection between a perturbation in gain of the calorimeters and the measured value of ω_a a simulation tool capable of producing a dataset with a comparable level of statistics to the full E989 experiment was used [62]. The generated data is either kept unchanged or perturbed according to a gain function. The final step is to analyse each of the time spectra and extract ω_a, this value for ω_a is then compared with the value from the unperturbed time spectrum to determine $\delta\omega_a$. In E821 the gain systematic uncertainty was a leading systematic effect at 70 ppb, for the E989 experiment we aim to reach a systematic uncertainty due to gain of 20 ppb. In this study two different gain perturbations will be investigated,

1. Rate dependent with twice the decay rate, $G(t) = \exp\left(-2t/\tau_\mu\gamma\right)$
2. Pileup time distribution as measured by the straw trackers.

The effect of changing the magnitude of these perturbations will also be investigated by multiplying the perturbation by a factor ϵ which is varied between 0 and 0.001. With higher statistics and more mature track finding and fitting software in the near future pileup consisting of $e^+ + e^+$ will be visible, this simulation tool and analysis can then be carried out again with the straw tracker measured $e^+ + e^+$ pileup rate.

7.4.1 Generating the simulated data set

The group behaviour of all decay positrons as seen by the calorimeter can be described by a five parameter function,

$$N(t,y) = N_0(y) \cdot \exp\left(\frac{-t}{\tau_\mu \gamma}\right) \cdot [1 + A(y)cos(\omega_a t + \phi(y))] \tag{7.1}$$

Where t represents the time in fill, y is the fractional energy where y_{max} would be the maximum beam energy of 3.09 GeV, τ_{mu} is the muon lifetime and γ is the Lorentz factor of the muon beam. The number of events, N_0, asymmetry, A, as well as phase, ϕ depend on the initial energy of the positron. These functions are known theoretically for a flat detector acceptance however the detector acceptance is not uniform across the decay energy range in the experimental setup. As it would be time and resource prohibitive to fully simulate these parameters for the full E989 level of statistics this study will use functional forms to seed the parameterisation. More information about the GEANT simulation carried out to obtain the parameters N_0, A and ϕ for this dataset can be found in [62].

Histograms corresponding to different energy layers can then be filled according to equation 7.1 and scaled to match the planned E989 dataset. Statistical fluctuations are introduced to each bin according to the Poisson distribution. Each energy 'layer' has a width of 1.5 MeV with the time spectra extending for 600 μs with a bin width of 149 ns (the cyclotron period of the g-2 ring). Figure 7.23 shows the time spectra for different energy layers over the range of above threshold layers.

A full unperturbed time spectra (or 'perfect wiggle' as shown in figure 7.25) can then be formed by integrating over each energy layer after a weight function is applied. This weight function, shown in figure 7.24, gives the probability of a certain positron being detected above the energy threshold of 1.8 GeV. The detector energy resolution is built into the weight function, set to be 5 % at 1 GeV in this study.

7.4.2 Perturbing the data

The perturbed time spectra (or 'perturbed wiggle') is generated in a similar fashion to the unperturbed but during the energy bins integration a gain function, $G(t)$, is applied prior to applying the weight function. This introduces a time dependence to

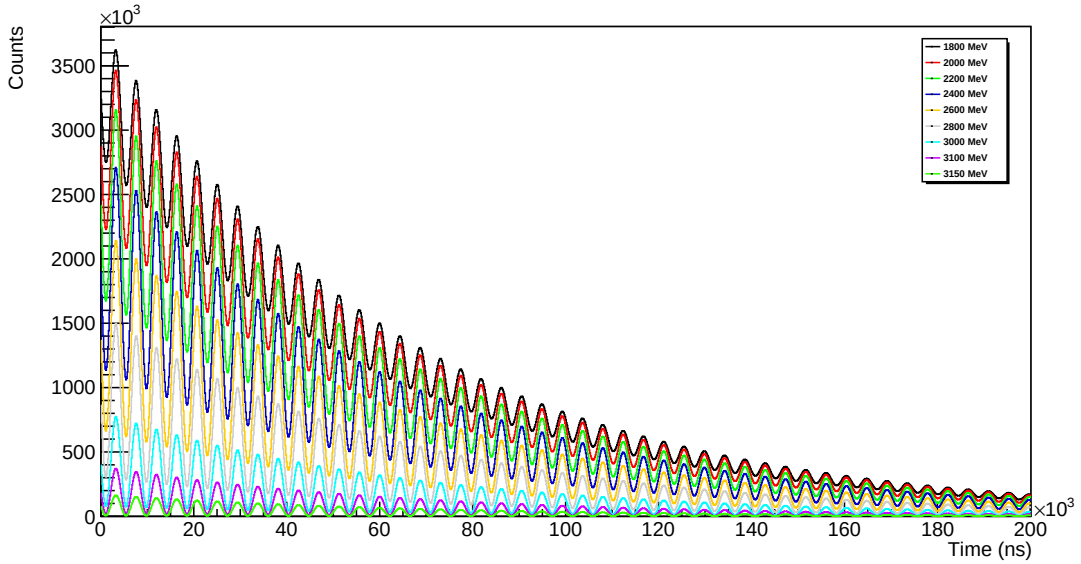

Figure 7.23: Time spectra for different energy layers above threshold value up to 200 μs.

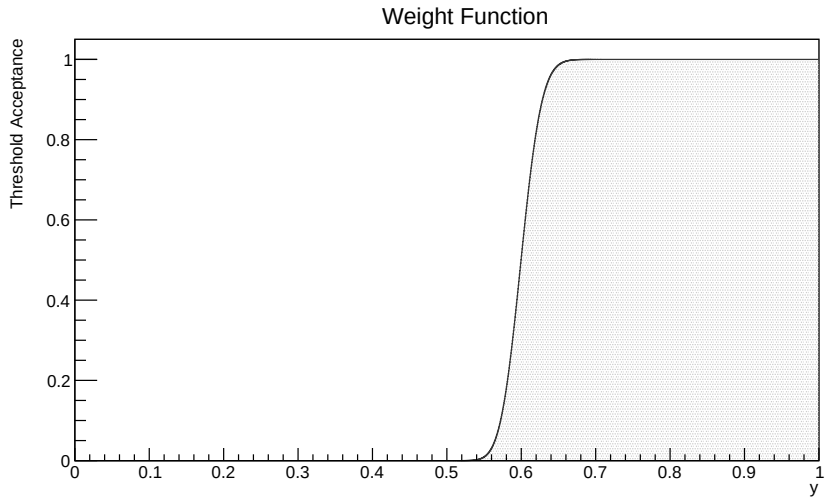

Figure 7.24: Weight function corresponding to the probability of a positron with a certain energy, y, being detected above threshold value of 1.8 GeV with a detector energy resolution of 5% at 1 GeV included.

the weight as the energy used in computing the weight is not the energy of the bin used

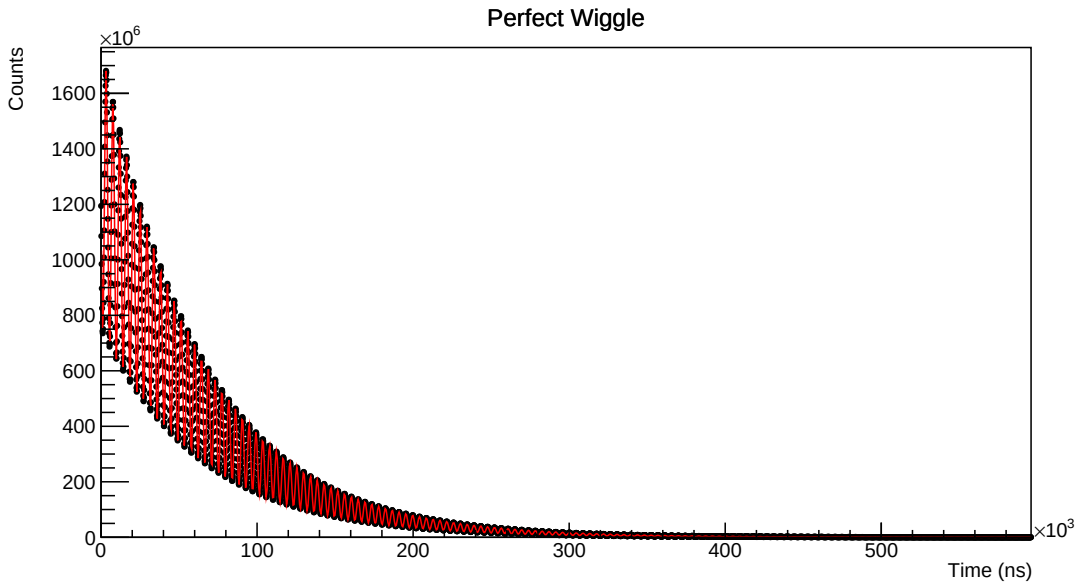

(a) Unperturbed time spectrum (black points) with overlaid fit (red line) over the whole fill of 600 μs.

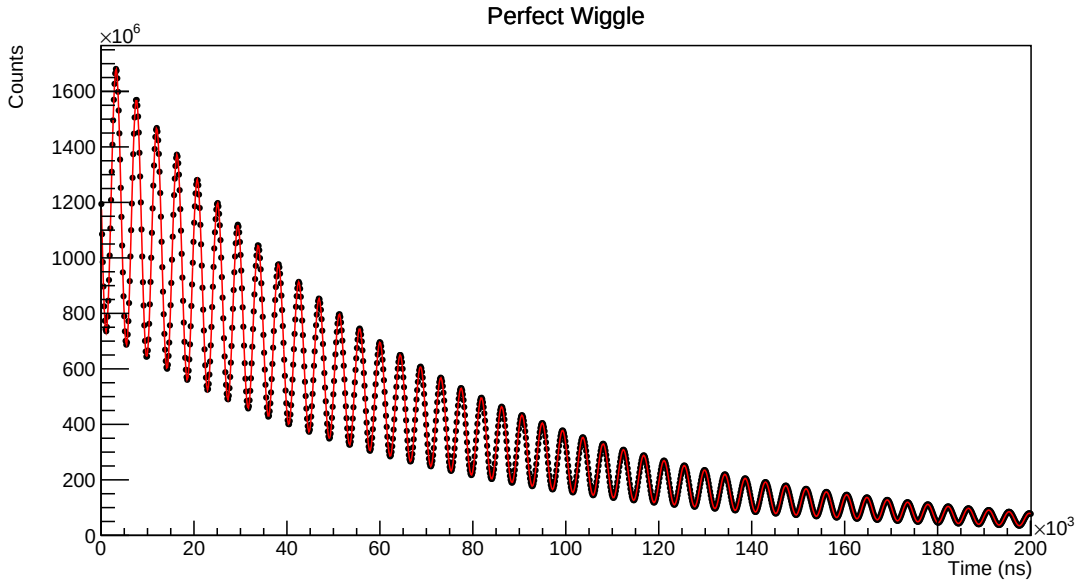

(b) Unperturbed time spectrum (black points) with overlaid fit (red line) between 0 and 200 μs.

Figure 7.25: Unperturbed time spectrum with fit.

but the energy of the bin after a time dependent gain perturbation has been applied.

$$y \to y\,(1 + \epsilon \cdot G(t))\,, \tag{7.2}$$

where ϵ allows the magnitude of the perturbation to be adjusted. As outlined at the start of section 7.4 there are two different perturbations which were investigated.

1. Rate dependent hypothesis. To emulate pileup which is rate dependent the gain is increased at the start of the fill and decays away exponentially with twice the decay rate throughout the fill,

$$G(t) = \exp\left(-2t/\tau_\mu\gamma\right). \tag{7.3}$$

2. Straw Tracker measured rate. The pileup rate in the calorimeter measured by the tracker is fitted and used as an increased gain, as explained in section 7.3.2.

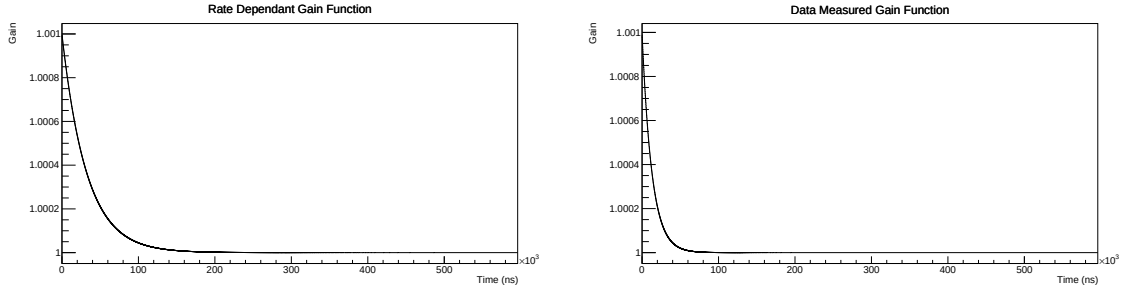

Figure 7.26: Gain functions used to perturb the ideal dataset. *Left:* Rate dependent gain function. *Right:* Pileup rate as measured by the straw trackers.

7.4.3 Analysis of unperturbed and gain perturbed data

After the three datasets are produced - perfect wiggle, rate dependant perturbed wiggle and straw tracker measured pileup perturbed wiggle - analyses can be carried out to extract ω_a from both of the perturbed wiggles as well as the perfect wiggle. The ω_a values extracted from the perturbed wiggle are compared with the value from the perfect wiggle to determine $\delta\omega_a$.

The function used to fit the data is,

$$N(t,y) = \exp\left(\frac{-t}{\tau_\mu\gamma}\right)\cdot[N_0 + A_c cos(\omega_a(1-R\cdot 10^{-6})t) + A_s sin(\omega_a(1-R\cdot 10^{-6})t)]. \tag{7.4}$$

There are certain key differences between the equation used to fit the data and the five parameter function used to generate the data, namely there are now two sinusoidal terms rather than a phase term and the asymmetry term is split into A_c and A_s. So the phase term, ϕ previously, is given by $\arctan(\frac{A_c}{A_s})$ and the asymmetry term is equal to $\sqrt{A_c^2 + A_s^2}/N_0$. The fit function also differs because the value for ω_a is fixed with the additional variable, R, which is used to parameterise the systematic shift in ω_a, with the factor of 10^{-6} included to give the R the units of parts per million of ω_a.

Figures 7.27, 7.28 and 7.29 present the three generated time spectrums, each with the overlaid fit as well as the residuals to each fit, and the Fourier transform of the residuals. It can be seen that the fit of the perturbed wiggles do not strictly satisfy a goodness of fit test from the χ^2/ndf - while the perfect wiggle does - this problem is not eliminated but rather shows a systematic effect before there is a noticeable change to the extracted ω_a frequency. Here this problem is not accounted for and the extracted values of ω_a are used to produce a $\delta\omega_a$ value for each corresponding perturbation.

Investigation can be made into changing the fit configuration, figures 7.30, 7.31 and 7.32 show how the fit parameters vary as a function of fit start time. In the case of the perfect wiggle the reduced χ^2 is at an acceptable level and remains acceptable when scanning the fit start time between 0 and 100 ns. While the extracted fit parameters fluctuate as the fit start time is scanned in the same time range with the fluctuations arising from fewer statistics at later start fit times. In the perturbed cases ($\epsilon = 0.001$), shown in 7.31 and 7.32, the reduced chi-squared varies a large amount at 0 ns and flattens out at around 40-50 μs while the rest of the fit parameters take longer to reach nominal levels.

With the level of statistics currently available the magnitude of the perturbation is unknown, but the magnitude of the perturbation can be varied by multiplying the perturbation gain functions by a factor, ϵ, and refitted. Figure 7.33 and 7.34 shows the value for $\delta\omega_a$ as ϵ is varied between 0 and 0.001. In both cases the increase in $\delta\omega_a$ is linear with ϵ. The start time used for this study was set to be the nominal 40 μs after

beam injection, which is the expected time that the ω_a fit will start from in the main experiment.

It has been shown to be possible to measure the calorimeter pileup rate using the straw trackers with several candidates found at early times in the current dataset. The composition of current measurable pileup was determined to be between $\mu^+ + e^+$ and is consistent with the time at which scraping of the beam occurs. The method of starting the fit at a later time, approximately 40 μs after injection, would remove the effect of this perturbation if the form of the $\mu^+ + e^+$ pileup remains constant. Furthermore, the ability of the straw trackers to detect and determine in fill $\mu^+ + e^+$ pileup has been demonstrated, and limits how early the starting time of the fits used to determine ω_a can be pushed back to. In future analyses this form of pileup should not be excluded as it can potentially affect the ω_a measurement by introducing an additional early to late effect. The $\mu^+ + e^+$ pileup events were used to develop the algorithm, which is generic enough to be used directly for both forms of the pileup.

7.4.4 Conclusion

As described in Chapter 5 the straw trackers have a wide variety of uses, one of which is the ability to cross check aspects of the calorimeters. The work in this chapter presented the development of the straw tracker and calorimeter matching algorithm written within the *g-2* software framework as well as the ability to probe aspects of the calorimeter with the matched tracks, this was the first example of particle identification at the experiment and demonstrates the power of matching multiple detectors. The ability to carry out a track and calorimeter related analysis was unavailable at the BNL experiment as they never had a working matching algorithm. This investigation discovered a small vertical offset between the two detectors systems at both tracker locations as well as a single crystal with a lower efficiency in one of the calorimeters. Both of these aspects will be addressed in future rounds of alignment and calibration. The ability to use the straw trackers to measure the calorimeter pileup rate was also developed with the effect to the measured ω_a value calculated for both the measured

pileup rate and a purely rate dependent pileup rate. With the data available it was found that the composition of the measured pileup events were mainly $\mu^+ + e^+$ at the start of the fill and delaying the start of the ω_a fit until after the beam scraping period, approximately $40\mu s$ after injection, removed the perturbation from pileup.

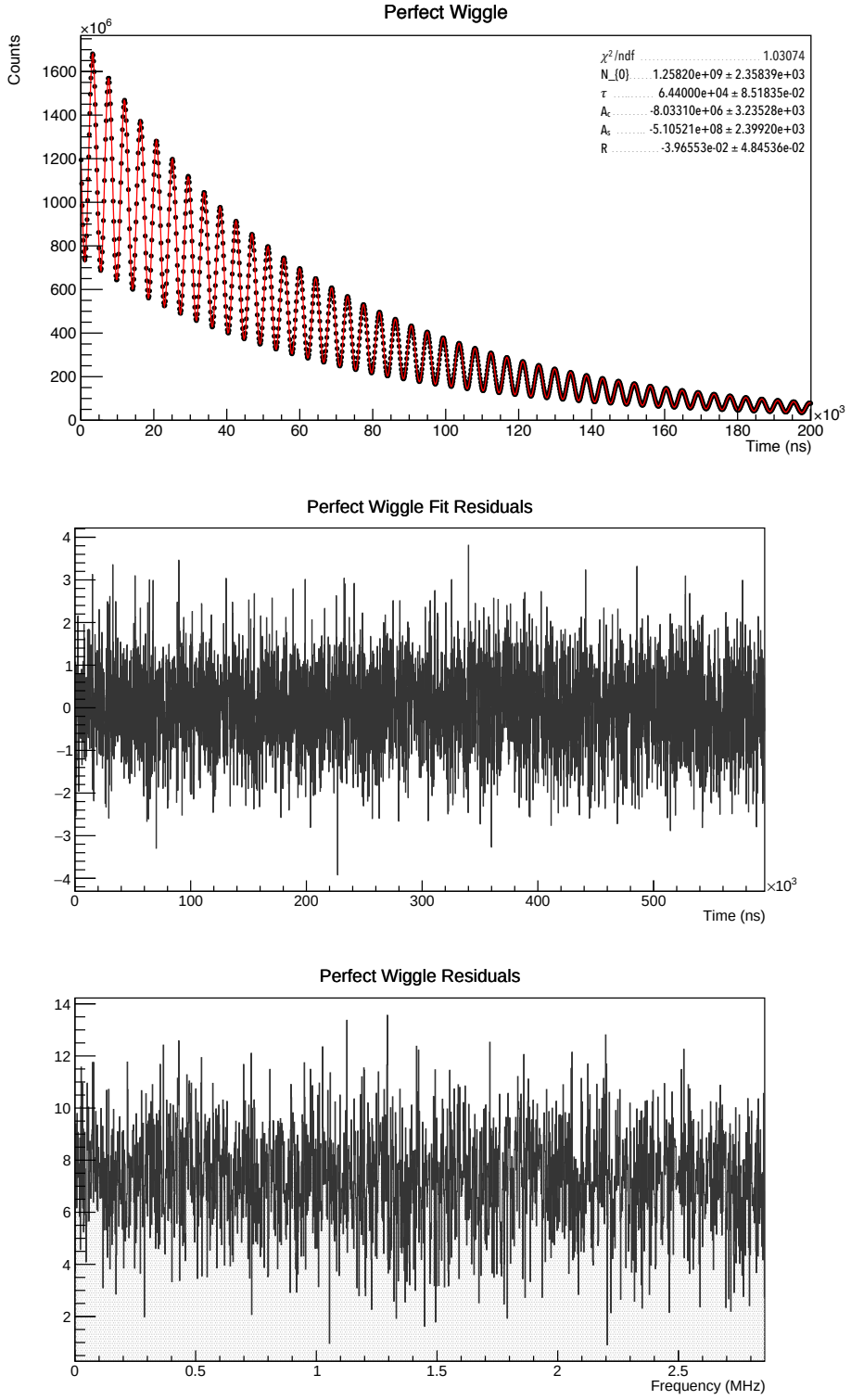

Figure 7.27: *Top:* Unperturbed wiggle plot between 0 and 200 μs with fit parameters given. *Bottom Left:* Fit residuals given for the full time scale of the time spectra. *Bottom Right:* Fourier transform of the fit residuals to show components not accounted for in the fit displayed in frequency space.

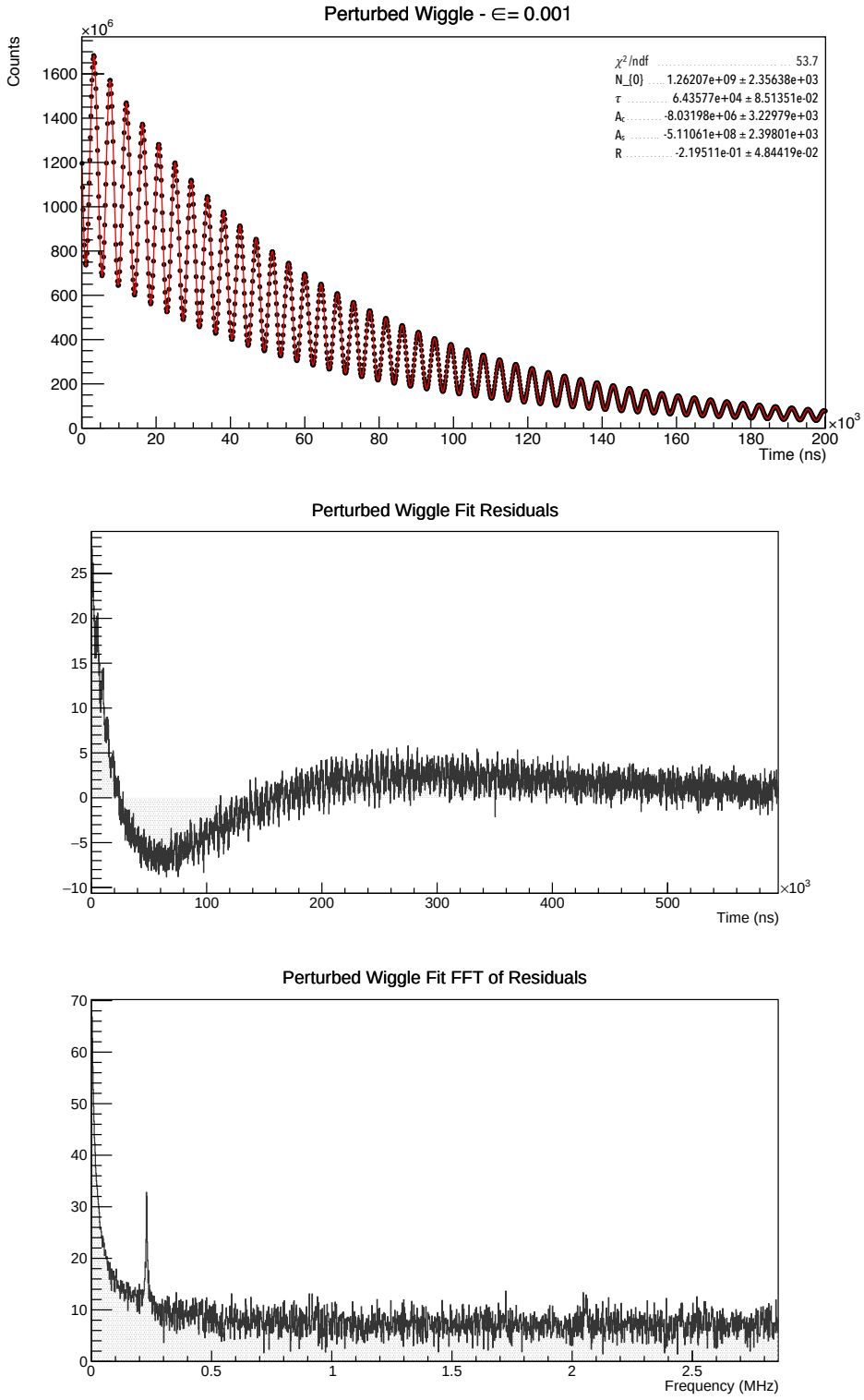

Figure 7.28: *Top:* Perturbed wiggle plot ($\epsilon = 0.001$) for the rate dependant case between 0 and 200 μs with fit parameters given. *Middle:* Fit residuals given for the full time scale of the time spectra. *Bottom:* Fourier transform of the fit residuals to show - in frequency space - any components not accounted for in the fit. Here it is clearly possible to see a peak at 0.231 MHz which corresponds to the g-2 frequency.

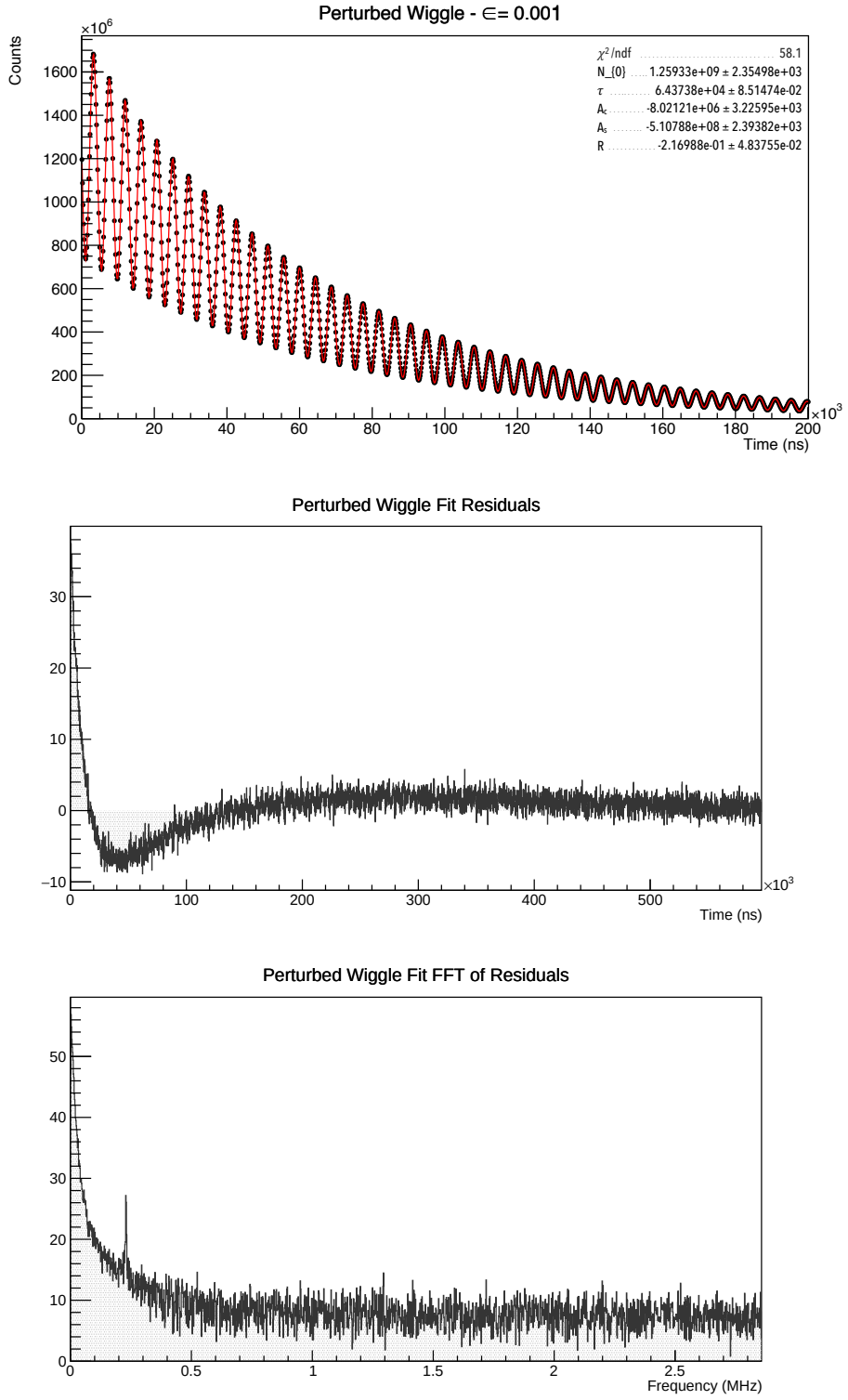

Figure 7.29: *Top:* Perturbed wiggle plot ($\epsilon = 0.001$) for the measured pileup case between 0 and 200 μs with fit parameters given. *Middle:* Fit residuals given for the full time scale of the time spectra. *Bottom:* Fourier transform of the fit residuals to show - in frequency space - any components not accounted for in the fit. Here it is clearly possible to see a peak at 0.231 MHz which corresponds to the g-2 frequency.

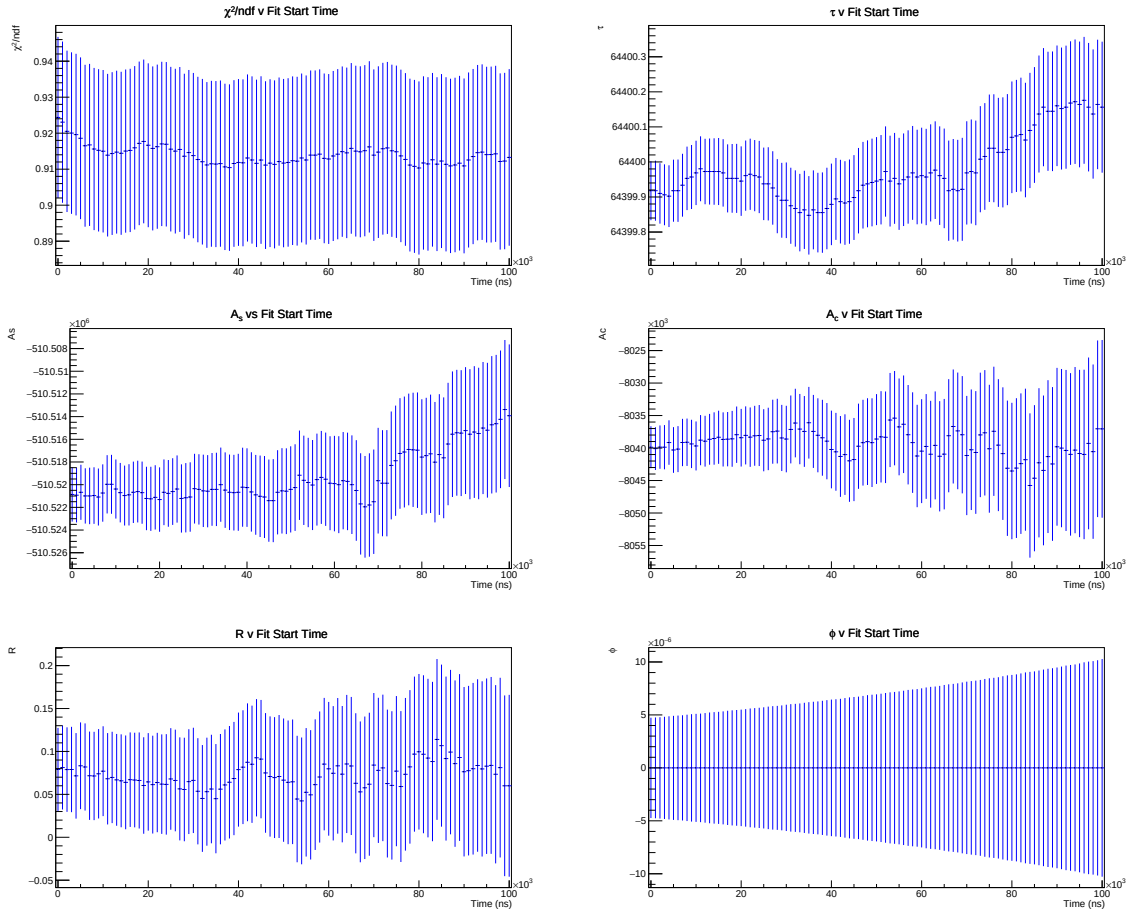

Figure 7.30: Values for the fit parameters for the unperturbed wiggle as the fit start time is varied. *Top Left:* The change in reduced chi-squared as the fit start time is varied between 0 and 100 μs.

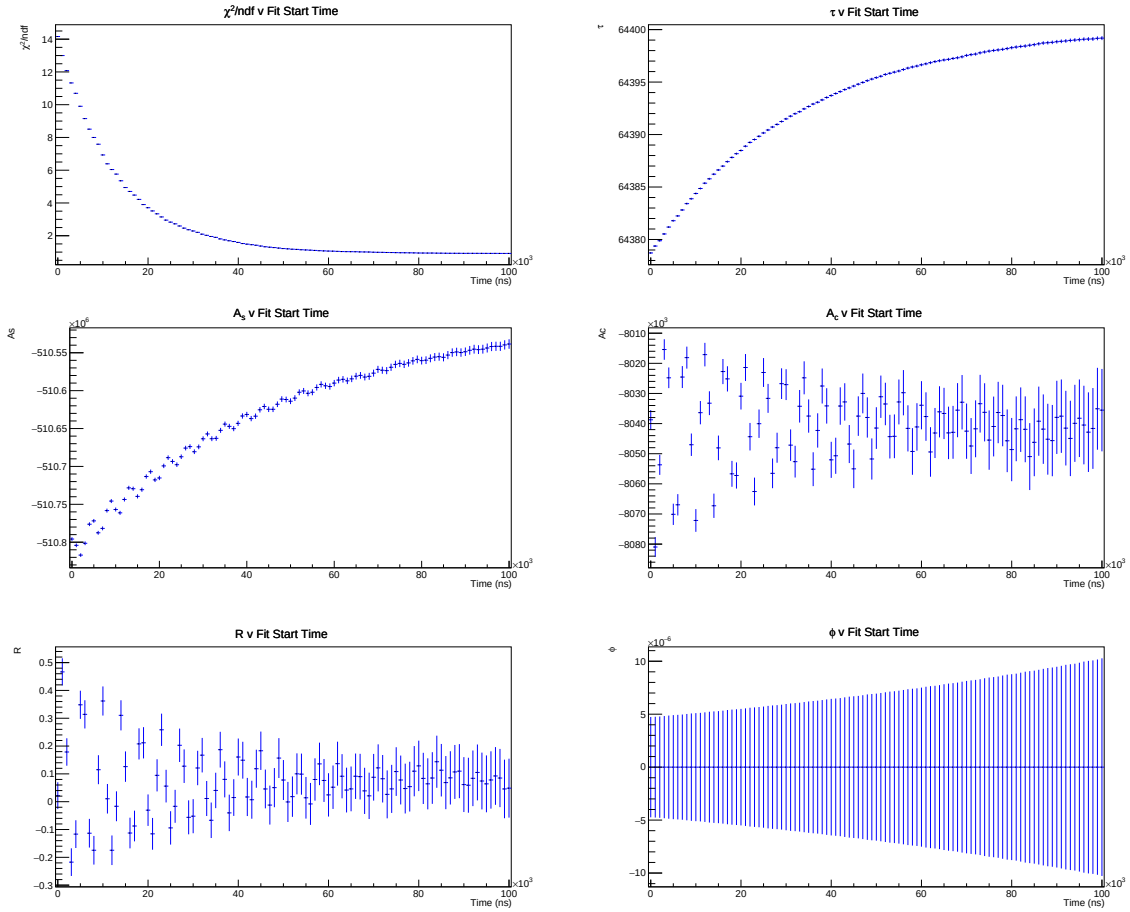

Figure 7.31: Values for the fit parameters for the theoretical rate dependant pileup perturbation as the fit start time is varied.

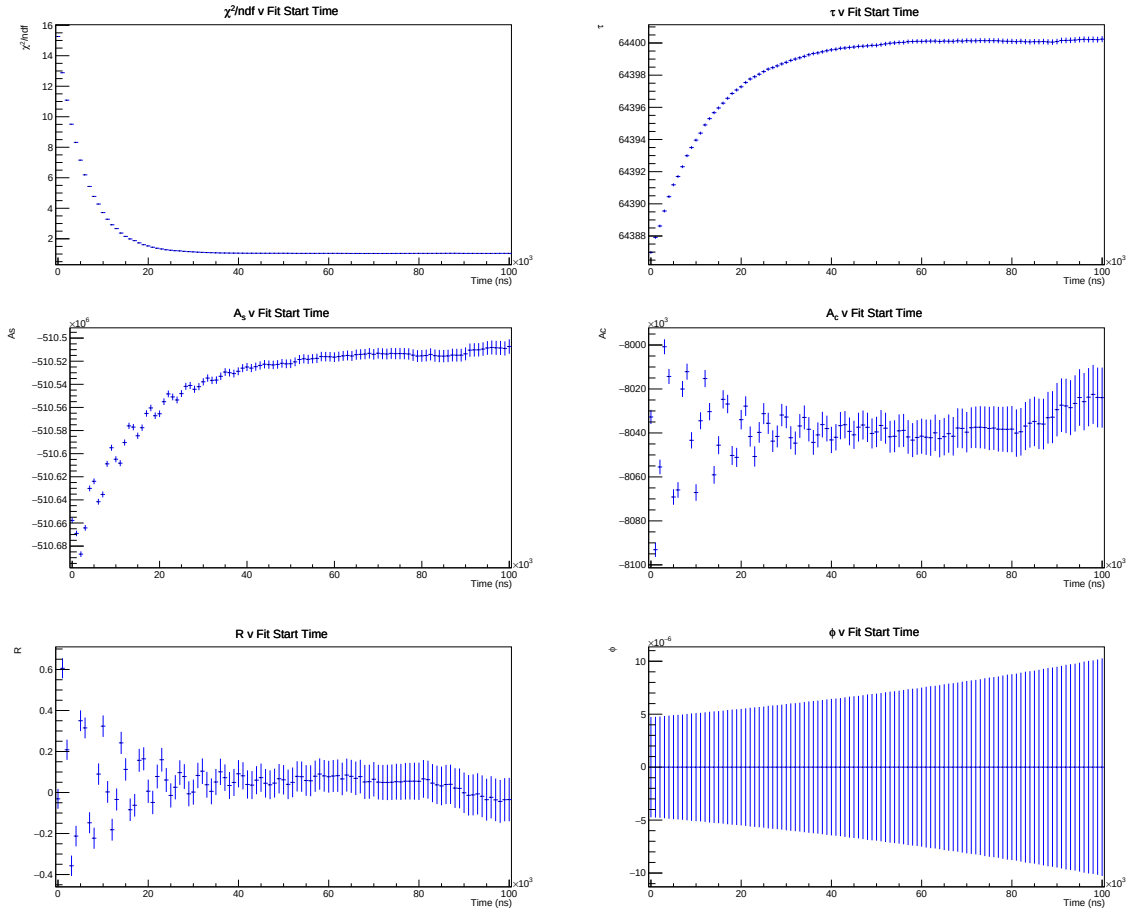

Figure 7.32: Values for the fit parameters for the measured pileup rate perturbation as the fit start time is varied.

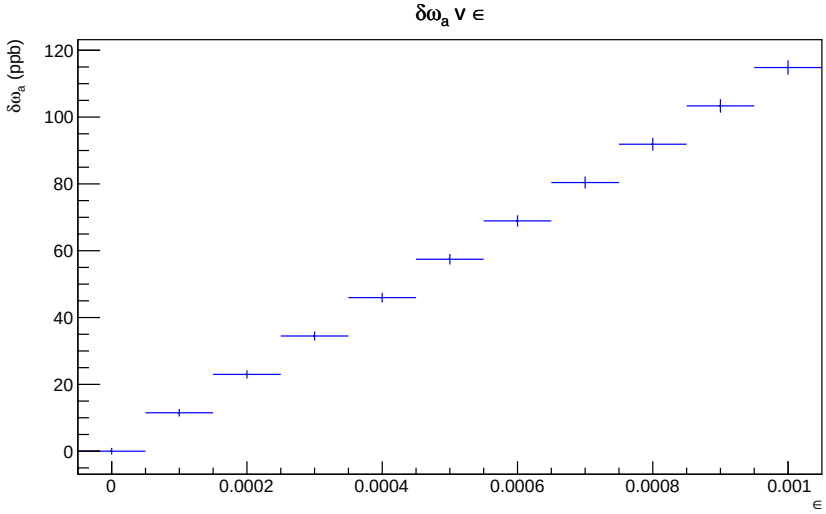

Figure 7.33: Size of $\delta\omega_a$ for different perturbation magnitudes, ϵ, for the rate dependant case.

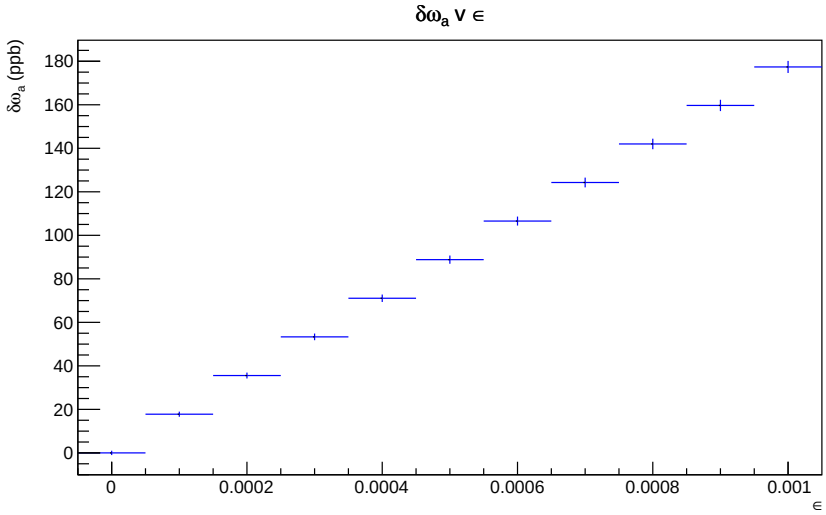

Figure 7.34: Size of $\delta\omega_a$ for different perturbation magnitudes, ϵ, for the straw tracker measured pileup case.

Chapter 8

Current status and outlook

The Fermilab muon g-2 experiment is currently going through the first physics data taking phase and reached an integrated number of e^+ of 116% of the BNL dataset (before data quality cuts) in May 2018, as shown in figure 8.1. The straw trackers have been crucial in this effort by providing real-time beam position reconstruction, this not only gives prompt feedback to the beam tuning efforts but also detects any change in beam conditions during operation.

This piece of work has covered the design, construction and initial testing of straw tracker modules carried out at the University of Liverpool as well as the testing, installation and commissioning at Fermi National Laboratory. Overall, 22 straw tracker modules were delivered with 16 currently installed in the storage ring, from the modules currently installed 99.7% of the channels are fully operational, with a large proportion of the author's contributions entering the detector construction, presented in chapter 6. The installed modules have been operating exceptionally stably for almost a year which bears testament to the level of thought that entered every detail from everyone involved in the module design and construction. The ability to monitor and control the high voltage status of each channel was developed along with the ability to monitor the data coming from the detector system in near real-time as part of the data quality monitor. A number of tracker performance plots have been presented showing the successful

operation, readout and tracking from these modules as well as giving an overview of the different analyses which the straw trackers can provide useful information towards.

The ability to match the straw tracker tracks with calorimeter clusters has also been developed, as presented in chapter 7, which opens the door to a huge amount of future analyses which were unavailable at the BNL experiment as they did not have a working matching algorithm. The matched events have been used to further characterise both detector systems and lead to the identification of a vertical offset between the tracker and calorimeter at both tracker locations of approximately 2.8 mm as well as determining that one of the crystals in calorimeter 18 has a lower efficiency, these two effects will be addressed in future rounds of alignment and calibration. Lastly, the matched events provided the ability to make an initial measurement the calorimeter pileup rate, this measured rate as well as a purely rate dependant hypothesised pileup rate was used to determine the effect to the measured ω_a value. With the data available it was found that the composition of the measured pileup events were mainly $\mu^+ + e^+$ at the start of the fill and delaying the start of the ω_a fit until after the beam scraping period, approximately $40\mu s$ after injection, removed the perturbation to ω_a from pileup. With improved beam storage, increased statistics as well as more mature tracking algorithms the trackers will be able to measure the in fill e^+ and e^+ pileup which will be invaluable to the final pileup analysis. Furthermore, the unique ability of the straw trackers to detect and determine in fill μ^+ and e^+ pileup has been demonstrated, and limits how early the starting time of the fits used to determine ω_a can be pushed back to.

At the time of writing E989 is nearing the end of the first data taking period and over the next 18-24 months ten-times the statistics of the BNL measurement will be collected. This dataset will produce the world's best measurement of a_μ. If the central value remains the same and the aims to reduce the uncertainties involved in the measurement by a factor of four are realised then a $\sim 7\ \sigma$ discrepancy between the experimental measurement and standard model theoretical calculation will be reached, providing evidence of an undiscovered physical process.

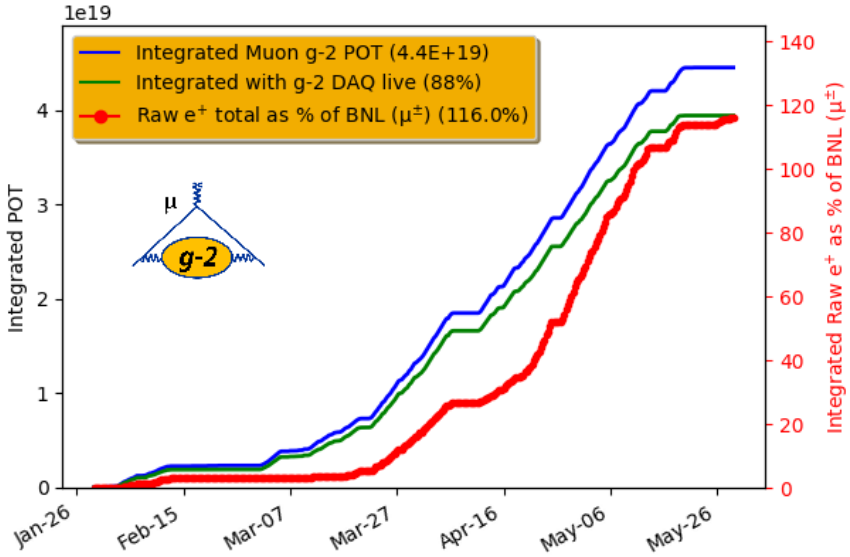

Figure 8.1: The number of recorded positrons taken by E989 between January 26th and May 26th 2018 as well as showing the integrated number of e^+ as a percentage of the BNL dataset ($\mu^\pm$).

References

[1] The quantum theory of the electron. *Proceedings of the Royal Society of London A: Mathematical, Physical and Engineering Sciences*, 117(778):610–624, 1928.

[2] L. E. Kinsler and W. V. Houston. The value of $\frac{e}{m}$ from the zeeman effect. *Phys. Rev.*, 45:104–108, Jan 1934.

[3] P. Kusch. Magnetic moment of the electron. *Science*, 123(3189):207–211, 1956.

[4] R. P. Feynman. Space-time approach to quantum electrodynamics. *Phys. Rev.*, 76:769–789, Sep 1949.

[5] F. J. Dyson. The radiation theories of tomonaga, schwinger, and feynman. *Phys. Rev.*, 75:486–502, Feb 1949.

[6] S. Tomonaga. On a relativistically invariant formulation of the quantum theory of wave fields*. *Progress of Theoretical Physics*, 1(2):27–42, 1946.

[7] Julian Schwinger. Quantum electrodynamics. i. a covariant formulation. *Phys. Rev.*, 74:1439–1461, Nov 1948.

[8] Julian Schwinger. On quantum-electrodynamics and the magnetic moment of the electron. *Phys. Rev.*, 73:416–417, Feb 1948.

[9] A. A. Schupp, R. W. Pidd, and H. R. Crane. Measurement of the g factor of free, high-energy electrons. *Phys. Rev.*, 121:1–17, Jan 1961.

[10] Boris L Ioffe. Weak interactions at short distances. *Soviet Physics Uspekhi*, 16(4):459, 1974.

[11] Fred Jegerlehner and Andreas Nyffeler. The muon g2. *Physics Reports*, 477(1):1 – 110, 2009.

[12] G. W. Bennett, B. Bousquet, H. N. Brown, G. Bunce, R. M. Carey, P. Cushman, G. T. Danby, P. T. Debevec, M. Deile, H. Deng, W. Deninger, S. K. Dhawan, V. P. Druzhinin, L. Duong, E. Efstathiadis, F. J. M. Farley, G. V. Fedotovich, S. Giron, F. E. Gray, D. Grigoriev, M. Grosse-Perdekamp, A. Grossmann, M. F. Hare, D. W. Hertzog, X. Huang, V. W. Hughes, M. Iwasaki, K. Jungmann, D. Kawall, M. Kawamura, B. I. Khazin, J. Kindem, F. Krienen, I. Kronkvist, A. Lam, R. Larsen, Y. Y. Lee, I. Logashenko, R. McNabb, W. Meng, J. Mi, J. P. Miller, Y. Mizumachi, W. M. Morse, D. Nikas, C. J. G. Onderwater, Y. Orlov, C. S. Özben, J. M. Paley, Q. Peng, C. C. Polly, J. Pretz, R. Prigl, G. zu Putlitz, T. Qian, S. I. Redin,

O. Rind, B. L. Roberts, N. Ryskulov, S. Sedykh, Y. K. Semertzidis, P. Shagin, Yu. M. Shatunov, E. P. Sichtermann, E. Solodov, M. Sossong, A. Steinmetz, L. R. Sulak, C. Timmermans, A. Trofimov, D. Urner, P. von Walter, D. Warburton, D. Winn, A. Yamamoto, and D. Zimmerman. Final report of the e821 muon anomalous magnetic moment measurement at bnl. *Phys. Rev. D*, 73:072003, Apr 2006.

[13] A. Keshavarzi, D. Nomura, and T. Teubner. The muon $g-2$ and $\alpha(M\_Z^2)$: a new data-based analysis. *ArXiv e-prints*, February 2018.

[14] D. W. Hertzog. Next Generation Muon g - 2 Experiments. In *European Physical Journal Web of Conferences*, volume 118 of *European Physical Journal Web of Conferences*, page 01015, April 2016.

[15] A. Czarnecki and W.J. Marciano. Muon anomalous magnetic moment: A harbinger for new physics. *prd*, 64(1):013014, July 2001.

[16] Tatsumi Aoyama, Masashi Hayakawa, Toichiro Kinoshita, and Makiko Nio. Complete tenth-order qed contribution to the muon $g-2$. *Phys. Rev. Lett.*, 109:111808, Sep 2012.

[17] Tatsumi Aoyama, Masashi Hayakawa, Toichiro Kinoshita, and Makiko Nio. Complete Tenth-Order QED Contribution to the Muon g-2. *Phys. Rev. Lett.*, 109:111808, 2012.

[18] C. Gnendiger, D. Stöckinger, and H. Stöckinger-Kim. The electroweak contributions to $(g-2)_\mu$ after the higgs-boson mass measurement. *Phys. Rev. D*, 88:053005, Sep 2013.

[19] James P. Miller, Eduardo de Rafael, B. Lee Roberts, and Dominik Stöckinger. Muon (g 2): Experiment and theory. *Annual Review of Nuclear and Particle Science*, 62(1):237–264, 2012.

[20] Michel Davier, Andreas Hoecker, Bogdan Malaescu, and Zhiqing Zhang. Reevaluation of the hadronic vacuum polarisation contributions to the Standard Model predictions of the muon $g-2$ and $\alpha(m_Z^2)$ using newest hadronic cross-section data. *Eur. Phys. J.*, C77(12):827, 2017.

[21] Fred Jegerlehner. Muon g - 2 theory: The hadronic part. In *KLOE-2 Workshop on e+ e- Collision Physics at 1 GeV, Frascati, Italy, Edited by Di Domenico, A.; EPJ Web of Conferences, Volume 166, id.00022*, volume 166, January 2018.

[22] Joaquim Prades, Eduardo de Rafael, and Arkady Vainshtein. The Hadronic Light-by-Light Scattering Contribution to the Muon and Electron Anomalous Magnetic Moments. *Adv. Ser. Direct. High Energy Phys.*, 20:303–317, 2009.

[23] Andreas Nyffeler. Precision of a data-driven estimate of hadronic light-by-light scattering in the muon $g-2$: Pseudoscalar-pole contribution. *Phys. Rev.*, D94(5):053006, 2016.

[24] Dominik Stöckinger. (g2) and physics beyond the standard model. *Nuclear Physics B - Proceedings Supplements*, 181-182:32 – 36, 2008. Proceedings of the International Workshop on e+e- Collisions from to .

[25] Andrzej Czarnecki and William J. Marciano. Muon anomalous magnetic moment: A harbinger for "new physics". *Phys. Rev. D*, 64:013014, Jun 2001.

[26] Dominik Stockinger. The Muon Magnetic Moment and Supersymmetry. *J. Phys.*, G34:R45–R92, 2007.

[27] B Lee Roberts. Searching for physics beyond the standard model through the dipole interaction. *Journal of Physics: Conference Series*, 295(1):012027, 2011.

[28] C. Green, J. Kowalkowski, M. Paterno, M. Fischler, L. Garren, and Q. Lu. The Art Framework. *J. Phys. Conf. Ser.*, 396:022020, 2012.

[29] E. J. Williams and E. Pickup. Heavy Electrons in Cosmic Rays. *Nature*, 141:836, May 1938.

[30] Carl D. Anderson and Seth H. Neddermeyer. Cloud chamber observations of cosmic rays at 4300 meters elevation and near sea-level. *Phys. Rev.*, 50:263–271, Aug 1936.

[31] R. F. Christy and S. Kusaka. Burst production by mesotrons. *Phys. Rev.*, 59:414–421, Mar 1941.

[32] Val L. Fitch and James Rainwater. Studies of x-rays from mu-mesonic atoms. *Phys. Rev.*, 92:789–800, Nov 1953.

[33] EUROPEAN ORGANIZATION FOR NUCLEAR RESEARCH. Annual report 1959, dec 1959.

[34] Archives of muon g-2 experiment, 1959.

[35] D. Berley, R. L. Garwin, G. Gidal, and L. M. Lederman. Electric dipole moment of the muon. *Phys. Rev. Lett.*, 1:144–146, Aug 1958.

[36] F Combley, F.J.M Farley, and E Picasso. The cern muon (g-2) experiments. *Physics Reports*, 68(2):93 – 119, 1981.

[37] G. Charpak, F. J. M. Farley, R. L. Garwin, T. Muller, J. C. Sens, V. L. Telegdi, and A. Zichichi. Measurement of the anomalous magnetic moment of the muon. *Phys. Rev. Lett.*, 6:128–132, Feb 1961.

[38] F Combley and Emilio Picasso. The muon (g-2) precession experiments; past, present and future. *Phys. Rep.*, 14:1–58, 1974.

[39] J. Bailey, K. Borer, F. Combley, H. Drumm, C. Eck, F.J.M. Farley, J.H. Field, W. Flegel, P.M. Hattersley, F. Krienen, F. Lange, G. Lebée, E. McMillan, G. Petrucci, E. Picasso, O. Rúnolfsson, W. von Rüden, R.W. Williams, and S. Wojcicki. Final report on the cern muon storage ring including the anomalous magnetic moment and the electric dipole moment of the muon, and a direct test of relativistic time dilation. *Nuclear Physics B*, 150(Supplement C):1 – 75, 1979.

[40] V. Bargmann, Louis Michel, and V. L. Telegdi. Precession of the polarization of particles moving in a homogeneous electromagnetic field. *Phys. Rev. Lett.*, 2:435–436, May 1959.

[41] D. Stratakis, M. E. Convery, C. Johnstone, J. Johnstone, J. P. Morgan, M. J. Syphers, J. D. Crmkovic, W. M. Morse, V. Tishchenko, N. S. Froemming, and M. Korostelev. Performance analysis for the new G-2 experiment. *ArXiv e-prints*, July 2016.

[42] J. Grange et al. Muon (g-2) Technical Design Report. 2015.

[43] David Flay. Precision Magnetic Field Calibration for the Muon $g-2$ Experiment at Fermilab. *PoS*, ICHEP2016:1075, 2017.

[44] M. Farooq, T. Chupp, and Muon g-2 Collaboration Collaboration. Absolute Calibration of the Magnetic Field Measurement for Muon g-2. In *APS April Meeting Abstracts*, page F1.036, January 2017.

[45] J. Kaspar et al. Design and performance of SiPM-based readout of PbF_2 crystals for high-rate, precision timing applications. *JINST*, 12(01):P01009, 2017.

[46] L. P. Alonzi et al. The calorimeter system of the new muon g -2 experiment at Fermilab. *Nucl. Instrum. Meth.*, A824:718–720, 2016.

[47] L.P. Alonzi, A. Anastasi, R. Bjorkquist, D. Cauz, G. Cantatore, S. Dabagov, G. Di Sciascio, R. Di Stefano, R. Fatemi, C. Ferrari, A.T. Fienberg, A. Fioretti, A. Frankenthal, C. Gabbanini, L.K. Gibbons, K. Giovanetti, S.D. Goadhouse, W.P. Gohn, T.P. Gorringe, D. Hampai, D.W. Hertzog, M. Iacovacci, P. Kammel, M. Karuza, J. Kaspar, B. Kiburg, L. Li, F. Marignetti, S. Mastroianni, D. Moricciani, G. Pauletta, D.A. Peterson, D. Poani, L. Santi, M.W. Smith, D.A. Sweigart, V. Tishchenko, T.D. Van Wechel, G. Venanzoni, K.B. Wall, P. Winter, and K. Yai. The calorimeter system of the new muon g-2 experiment at fermilab. *Nuclear Instruments and Methods in Physics Research Section A: Accelerators, Spectrometers, Detectors and Associated Equipment*, 824(Supplement C):718 – 720, 2016. Frontier Detectors for Frontier Physics: Proceedings of the 13th Pisa Meeting on Advanced Detectors.

[48] A. Anastasi, D. Babusci, F. Baffigi, G. Cantatore, D. Cauz, G. Corradi, S. Dabagov, G. Di Sciascio, R. Di Stefano, C. Ferrari, A. T. Fienberg, A. Fioretti, L. Fulgentini, C. Gabbanini, L. A. Gizzi, D. Hampai, D. W. Hertzog, M. Iacovacci, M. Karuza, J. Kaspar, P. Koester, L. Labate, S. Mastroianni, D. Moricciani, G. Pauletta, L. Santi, and G. Venanzoni. Test of candidate light distributors for the muon (g - 2) laser calibration system. *Nuclear Instruments and Methods in Physics Research A*, 788:43–48, July 2015.

[49] B. Martinez, E. Diamond, A. Sblendorio, and F. Gray. Development and Testing of Scintillating Detectors for the Muon g-2 Experiment. In *APS Division of Nuclear Physics Meeting Abstracts*, page EA.098, September 2016.

[50] Kim Siang Khaw. Muon g-2 reconstruction and analysis framework. *18th International Workshop on Advanced Computing and Analysis Techniques in Physics Research*, aug 2017.

[51] J. D. Crnkovic C. C. Polly S. Ganguly, K. T. Pitts. Lost muon studies for the muon g-2 experiment at fermilab. *E989 Collaboration*, dec 2018.

[52] ANDREW BEHNKE. *STRUCTURAL ANALYSIS AND QUALITY CONTROL OF A MUON BEAM TRACKER*. PhD thesis, 2016.

[53] G.I. Merzon V.A. Chechin V.K. Ermilova, L.P. Kotenko. Primary specific ionization of relativistic particles in gases. 1969.

[54] Walter Blum, Werner Riegler, and Luigi Rolandi. *Particle Detection with Drift Chambers (Particle Acceleration and Detection)*. Springer, 2008.

[55] Fabio Sauli. Principles of operation of multiwire proportional and drift chambers. page 92 p, Geneva, 1977. CERN, CERN. CERN, Geneva, 1975 - 1976.

[56] Rob Veenhof. Garfield - simulation of gaseous detectors, jun 2018.

[57] Z. Ahmed et al. A prototype low-background multiwire proportional chamber. *JINST*, 9(01):P01009, 2014.

[58] Wasiq Bokhari, Joachim Heinrich, N Lockyer, Mitch Newcomer, Richard Van Berg, hh hh, M Binkley, A Mukherjee, Kevin Pitts, and R Wagner Fermilab. The asdq asic for the front end electronics of the cot. 01 2018.

[59] Nicholas Kinnaird. Geane track fitting. *g-2 Note*, aug 2017. G Minus 2 Experiment Document 8102-v3.

[60] W. Erni et al. Technical Design Report for PANDA Electromagnetic Calorimeter (EMC). 2008.

[61] S. Agostinelli, J. Allison, K. Amako, J. Apostolakis, H. Araujo, P. Arce, M. Asai, D. Axen, S. Banerjee, G. Barrand, F. Behner, L. Bellagamba, J. Boudreau, L. Broglia, A. Brunengo, H. Burkhardt, S. Chauvie, J. Chuma, R. Chytracek, G. Cooperman, G. Cosmo, P. Degtyarenko, A. Dell'Acqua, G. Depaola, D. Dietrich, R. Enami, A. Feliciello, C. Ferguson, H. Fesefeldt, G. Folger, F. Foppiano, A. Forti, S. Garelli, S. Giani, R. Giannitrapani, D. Gibin, J.J. Gómez Cadenas, I. González, G. Gracia Abril, G. Greeniaus, W. Greiner, V. Grichine, A. Grossheim, S. Guatelli, P. Gumplinger, R. Hamatsu, K. Hashimoto, H. Hasui, A. Heikkinen, A. Howard, V. Ivanchenko, A. Johnson, F.W. Jones, J. Kallenbach, N. Kanaya, M. Kawabata, Y. Kawabata, M. Kawaguti, S. Kelner, P. Kent, A. Kimura, T. Kodama, R. Kokoulin, M. Kossov, H. Kurashige, E. Lamanna, T. Lampén, V. Lara, V. Lefebure, F. Lei, M. Liendl, W. Lockman, F. Longo, S. Magni, M. Maire, E. Medernach, K. Minamimoto, P. Mora de Freitas, Y. Morita, K. Murakami, M. Nagamatu, R. Nartallo, P. Nieminen, T. Nishimura, K. Ohtsubo, M. Okamura, S. O'Neale, Y. Oohata, K. Paech, J. Perl, A. Pfeiffer, M.G. Pia, F. Ranjard, A. Rybin, S. Sadilov, E. Di Salvo, G. Santin, T. Sasaki, N. Savvas, Y. Sawada, S. Scherer, S. Sei, V. Sirotenko, D. Smith, N. Starkov, H. Stoecker, J. Sulkimo, M. Takahata, S. Tanaka, E. Tcherniaev, E. Safai Tehrani, M. Tropeano, P. Truscott, H. Uno, L. Urban, P. Urban, M. Verderi, A. Walkden, W. Wander, H. Weber, J.P. Wellisch, T. Wenaus, D.C. Williams, D. Wright, T. Yamada, H. Yoshida, and D. Zschiesche. Geant4a simulation toolkit. *Nuclear Instruments and Methods in*

Physics Research Section A: Accelerators, Spectrometers, Detectors and Associated Equipment, 506(3):250 – 303, 2003.

[62] D.W. Hertzog L.P. Alonzi, F.E. Gray. Study of gain perturbation on t and q method analysis. *E989 Collaboration Note 58*, dec 2015.